Genetic Approaches to Study Tissue Morphogenesis in *Drosophila*

BY

2009

Liang Zhang

B.S., University of Science and Technology of China (USTC), 2003

Submitted to the graduate degree program in Molecular Biosciences
and the Graduate Faculty of the University of Kansas
in partial fulfillment of the requirements for the degree of
Doctor of Philosophy

Committee members:

_____
Chairperson – Robert E. Ward

_____
Yoshiaki Azuma

_____
Robert S. Cohen

_____
Victoria L. Corbin

_____
Lena C. Hileman

_____
Erik A. Lundquist

_____
Mark L. Richter

Date defended: 11/04/2009

The Dissertation Committee for Liang Zhang certifies
that this is the approved version of the following dissertation:

Genetic Approaches to Study Tissue Morphogenesis in *Drosophila*

Committee members:

_____
Chairperson – Robert E. Ward

_____
Yoshiaki Azuma

_____
Robert S. Cohen

_____
Victoria L. Corbin

_____
Lena C. Hileman

_____
Erik A. Lundquist

_____
Mark L. Richter

Date approved: 11/30/2009

Abstract

Morphogenesis is defined as the change of body shape over time, the understanding of which is one of the central questions of developmental biology. To achieve proper overall organ and body shape, morphogenetic movements have to be precisely controlled during development. I have used both genetic and cell biological approaches to study control mechanisms of morphogenesis in the model organism *Drosophila melanogaster*. Nonmuscle myosin II (myosin hereafter) has well-established roles in generating contractile force on actin filaments during morphogenetic processes. Myosin activation is regulated by phosphorylation of the myosin regulatory light chain (MRCL, encoded by *spaghetti squash* or *sqh* in *Drosophila*) first on Ser-21 and subsequently on Thr-20. These phosphorylation events are positively controlled by a variety of kinases including myosin light chain kinase, Rho kinase, citron kinase, and AMP kinase and are negatively regulated by myosin phosphatase. The activation of myosin is thus highly regulated and is likely developmentally controlled. Therefore in order to monitor the activity of myosin during development, we have generated antibodies against the monophosphorylated (Sqh1P) and diphosphorylated (Sqh2P) forms of Sqh. We first show that the antibodies are highly specific for each phosphorylated form of the protein. We next used these antibodies on wild type *Drosophila* tissues. Interestingly, Sqh1P predominantly localizes in the adherens junction in imaginal disc cells, whereas Sqh2P locates

to the apical domain. Sqh1P and Sqh2P also show distinct patterns of expression in embryos. Sqh1P is expressed nearly ubiquitously and outlines cells consistent with a junctional localization, whereas Sqh2P is strongly expressed in the ventral furrow, the invaginating fore- and hindgut, the invaginating tracheal system, head segments during head involution, and the dorsal most row of epidermal (DME) cells during dorsal closure. These represent tissues that are undergoing extensive cell shape change or cell rearrangements. Sqh2P is localized very apically in these cells, and is noticeably enriched in filopodia emanating from the DME cells during dorsal closure. These antibodies will thus be very useful in monitoring myosin activation for functional studies of morphogenesis.

The tracheal system of *Drosophila melanogaster* has proven to be an excellent model system for studying the development of branched tubular organs. Mechanisms regulating the patterning and initial maturation of the tracheal system have been largely worked out, yet important questions remain regarding how the mature tubes inflate with air at the end of embryogenesis, and how the tracheal system grows in response to the oxygen needs of a developing larva that increases nearly 1000-fold in volume over a four day period. In chapter 2, I describe the cloning and characterization of *uninflatable* (*uif*), a gene that encodes a large transmembrane protein containing carbohydrate binding and cell signaling motifs in its extracellular domain. Uif is highly conserved in insect species, but does not appear to have a true ortholog in vertebrate species. *uif* is expressed zygotically beginning in stage 5 embryos, and

Uif protein localizes to the apical plasma membrane in all ectodermally derived epithelia, most notably in the tracheal system. *uif* mutant animals show defects in tracheal inflation at the end of embryogenesis, and die primarily as larvae. Tracheal tubes in mutant larvae are often crushed or twisted, although tracheal patterning and maturation appear normal during embryogenesis. *uif* mutant larvae also show defects in tracheal growth and molting of their tracheal cuticle. RNAi-induced knockdown of *uif* in the leg and wing imaginal discs attenuates Notch signaling and produces *Notch* loss-of-function phenotypes in corresponding adult tissues, indicating that Uif might be a positive regulator of Notch signaling during leg and wing imaginal disc development.

Acknowledgements

First, I would like to thank my mentor, Dr. Robert Ward, who is not only a wonderful advisor but also a dearest friend. I always feel that it is beyond my ability to express my gratitude to him. He has always been my role model of great scientist and professor. He gives me guidance on so many things, from how to do good experiments to how to do good science; from how to make beautiful PowerPoint slides to how to give a good presentation; from how to be a better graduate student to how to be a better person. Furthermore, he has given me the maximum amount of advice, encouragement and support to help me develop my career and manage my family and life. I consider him not only my mentor in graduate school for these 6 years but also my mentor in life for a lifetime.

I would like to thank my graduate committee members, Dr. Yoshi Azuma, Dr. Bob Cohen, Dr. Vicki Corbin, Dr. Lena Hileman, Dr. Erik Lundquist and Dr. Mark Richter. They have always been very supportive and have given me great advice and suggestions on my graduate work. Specially, I want to thank Dr. Corbin, Dr. Lundquist and Dr. Richter for serving as the readers of my research proposal and dissertation.

I want to give many thanks to my dearest friends, Ruth Entwistle and Kistie Brunsell for reading the very first draft of my dessertation and for all the support they gave me in these years.

Thanks to former and current undergraduate students who had worked with me or helped with my projects: Ty Beaver, Locke Uppendahl, Aaron Welch, Stefani Fontana, Aaron Olsen, Genea Edwards and Bethany Lucas.

Also, I want to thank John Connolly, the Graduate Program Assistant of the Department of Molecular Biosciences, for helping me schedule the committee meetings, oral exam and dissertation defense; for helping me find useful information about academic deadlines and rules; and for writing all sorts of supporting letters for me.

Last, I would like to thank my family, the most important people in my life. Thanks to my dear husband, Yu Wang, who is always there for me, faces everything and shares every feeling with me. Thanks to my daughter, Sophie, the sweetest girl in my mind; to my son, Nathan, a great fighter for life since he was born. Thanks to my parents and grandparents for their love since I was born. I want to give special thanks to my parents-in-law. Without their help with taking care of Nathan, who needs tremendous amount of special care, I would not have had the time to finish my dissertation and degree.

Table of Contents

List of Figures

List of Tables

Chapter 1

Introduction

The primary focus of my graduate research is to investigate mechanisms of morphogenesis, which is the change of organismal shape over time. Successful development requires the proper collaboration of morphogenetic processes, including cell shape change, cell rearrangement, oriented cell proliferation and patterned cell death. To study morphogenesis, the fruit fly *Drosophila melanogaster* offers a great model system. *Drosophila* is easy and inexpensive to culture. *Drosophila* has a short life cycle (~9-10 days in room temperature). The genome of the fly has been fully sequenced. ~70% of total genes and over 90% of disease genes are conserved between *Drosophila* and human. And there are many genetic tools available in this model organism. Genetics, therefore, provides a great tool to study morphogenesis in a simple model organism. Using forward genetics, we can isolate an unbiased set of mutations that affect specific morphogenetic events, and then can clone and characterize the genes affected by these mutations. We can also conduct reverse genetics by starting with specific genes and then create mutations in these genes to determine if they play a role in a particular morphogenetic event. In this chapter, I will introduce two morphogenetic events that I have studied during my graduate career, hormone dependent imaginal disc morphogenesis and larval tracheal morphogenesis,

using genetic approaches. Both of the morphogenetic events involve extensive cell shape change and cell rearrangement.

Part I. Ecdysone triggered imaginal disc morphogenesis in *Drosophila*

Hormonal signaling provides important cues and helps the proper coordination of morphogenetic events. Hormones can be divided into three major chemical classes including steroid hormones, peptide/protein hormones and amine hormones. We are particularly interested in steroid hormones, which are lipid-based molecules derived from cholesterol. In vertebrates, steroid hormones direct a wide range of development processes including growth, differentiation, metabolism, and homeostasis. For example, androgens control the development of primary sex characteristics in males while estrogens control those in females; Adrenal glucocorticoids play a key role in mediation of long-term stress [1]. Also, there is extensive evidence linking steroid hormones and their receptors to cancer. For instance, estrogen can promote growth of breast cancer cells containing estrogen receptors and/or progesterone receptors [2]. Consequently, estrogen agonists and antagonists have been used to treat breast cancer [3].

To study molecular mechanisms of steroid hormone action, *Drosophila melanogaster* provides an ideal model organism. 20-hydroxyecdysone (referred to as ecdysone hereafter) is the key steroid hormone that directs virtually every

major developmental transition during *Drosophila* life cycle. Pulses of ecdysone can be detected during embryogenesis, at each larval molt and during metamorphosis [4].

The action of ecdysone begins with its binding to a nuclear hormone receptor, which is a heterodimer of Ecdysone receptor (EcR) and Ultraspiracle (USP). The ligand-receptor complex then activates or represses the expression of the primary-response early genes. These early genes, many of which encode transcription factors, in turn, change the expression of the secondary-response late genes that direct the proper biological responses to ecdysone [4, 5].

Development of the *Drosophila* leg imaginal disc offers an excellent model system with which to characterize the molecular mechanisms of hormone dependent morphogenesis. The processes involved in imaginal disc morphogenesis are becoming clearer. During embryogenesis, precursor cells of the imaginal discs are specified. These cells then go through extensive proliferation and patterning during the larval instars. At the end of the third larval stage, each of the mature leg discs is a sac-like organ that consists of a single layer of epithelial cells [6]. The discs are connected to the larval epidermis through open stalks (Figure 1.1 A, B). In the sagittal view, it is apparent that a leg disc is composed of folded columnar epithelia on one side that grades into the squamous peripodial epithelia on the other (Figure 1.1 B). In response to the late larval ecdysone pulse that triggers puparium formation and initiates metamorphosis, these flat epithelial discs start elongating in the

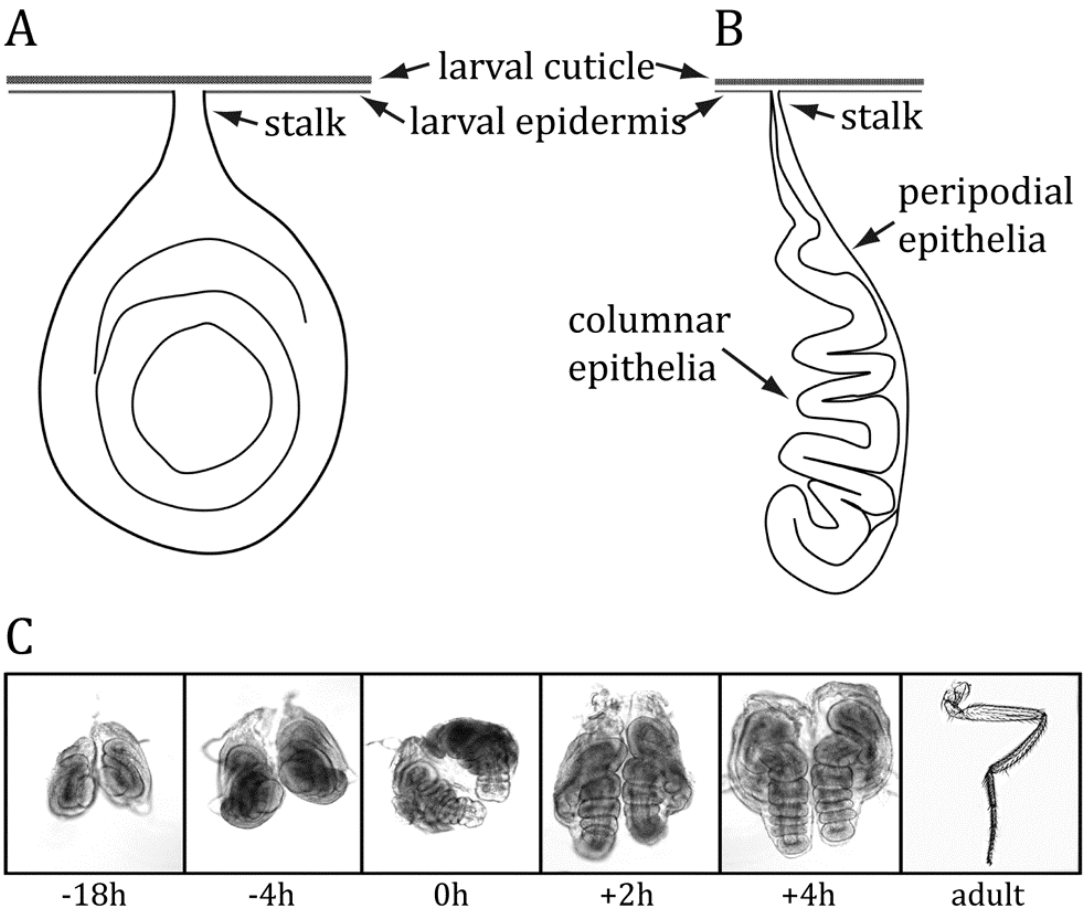

Figure 1.1
***Drosophila* leg morphogenesis**
(A, B) Schematic models of top view (A) and sagittal view (B) of a mature leg imaginal disc at 3rd instar larval stage.
(C) Live images of leg imaginal discs and an adult leg. Time points are given relative to puparium formation. (Images are from R Ward)

proximal-distal direction (Figure 1.1 C). Around 5 hours after puparium formation, the leg imaginal discs rapidly evert through the stalk opening and come to the outside of the puparium [7, 8]. The process of elongation and eversion together is called “evagination” [9, 10]. During pupal stage, the leg discs go through extensive differentiation and develop into adult legs (Figure 1.1 C).

During leg disc evagination, the relatively flat “Danish pastry”-like discs change to long and thin tubular rudimentary adult legs. Changes of cell shape contribute greatly to these changes in disc morphology. In 0-hour prepupal leg discs, the shape of cells in the basitarsal segments is highly asymmetric and oriented circumferentially. Six hours later, cells in the same segments elongate in the proximal-distal direction and become isometric. Active cell rearrangement also plays an important role in disc evagination. Fristrom [9] described that the number of cells encircling comparable regions is reduced in elongated discs as a result of cell movement. Recently, Taylor and Adler were able to visualize cell rearrangements using live imaging [10]. Taken together, the dramatic morphology changes of the discs are due to a combination of cell shape changes and cell rearrangements. However, despite extensive descriptions about the morphogenetic events during ecdysone triggered leg development, little is known about how the global hormonal signal is integrated into the cellular machinery. To address this question, large genetic screens have been performed to identify genes required for leg disc elongation and eversion [11, 12].

The *Broad-complex* (*BR-C*) encodes one set of ecdysone-inducible early genes, which belong to a family of at least four zinc-finger transcription factors that share a common core amino-terminal domain [4, 13]. Loss-of-function mutations suggest that one of these transcription factors, *broad* (*br*), is essential for disc elongation and eversion [14]. An amorphic *br* mutant allele (br^5) produces arrested discs with limited elongation (Figure 1.2 B). Previous work indicated that the cells in br^5 mutant leg discs fail to change shape [15]. A hypomorphic *br* mutant allele (br^1) only displays a weakly penetrant malformed leg phenotype (Figure 1.2 D). Using br^1 as a sensitized mutant background, two genetic modifier screens have been performed [11, 16]. In the recent screen, 26 individual mutations that enhance the br^1 leg phenotype (*E(br)* mutations) were recovered out of ~112,000 F1 progeny of EMS-treated br^1 animals [11]. Two of the *E(br)* mutations are allelic to the small GTPase, *Rho1*. Nonmuscle myosin II heavy chain (MHC, encoded by *zipper* (*zip*) in *Drosophila*) was also identified through these screens. Consistently, mutations in nonmuscle myosin regulatory light chain (MRLC, encoded by *spaghetti squash* (*sqh*) in *Drosophila*) result in disrupted leg morphogenesis [17].

The Rho family of small GTPases function as molecular switches that cycle between the inactivated form (Rho-GDP) and the activated form (Rho-GTP). The equilibrium between Rho-GDP and Rho-GTP is influenced by

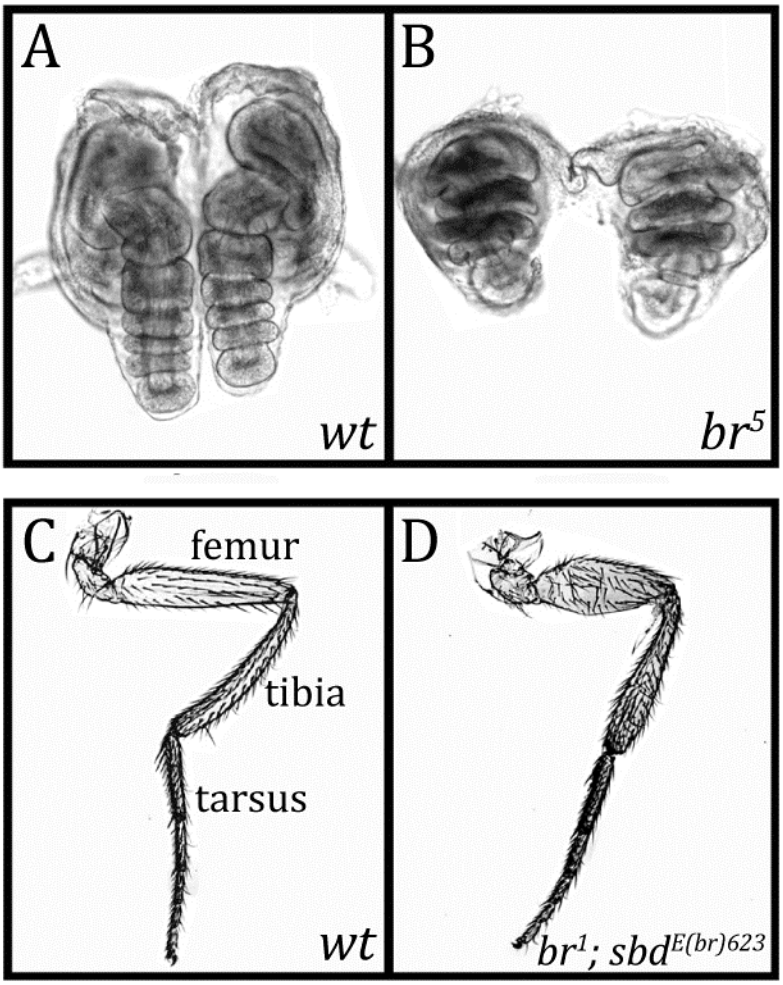

Figure 1.2
***broad* function is essential for leg morphogenesis**
(A) A pair of wild type leg imaginal discs 4 hours after pupariation.
(B) A pair of *br*^{5} mutant leg imaginal discs 4 hours after pupariation. Note the limited elongation.
(C) A wild type adult leg with three segments, femur, tibia and tarsus.
(D) A malformed leg. Note the fatter and shorter femur and tibial segments.
(Images are from R Ward)

RhoGEFs, which are guanine nucleotide exchange factors that promote the exchange of GDP to GTP, and by RhoGAPs, which are GTPase activating proteins that promote the hydrolysis of GTP to GDP. In addition, RhoGDIs (GDP dissociation inhibitors) can reinforce the action of RhoGAPs by binding to RhoGDP and preventing nucleotide exchange (Figure 1.3). In the active state, Rho works through a variety of downstream effectors and controls many aspects of cell behavior including reorganization of the actin cytoskeleton, axonal guidance, cell polarity, microtubule dynamics, gene transcription, apoptosis and oncogenic transformation etc (reviewed in [18, 19]).

One key effecter of activated Rho is Rho-kinase, a serine-threonine kinase that can phosphorylate the myosin regulatory light chain (MRLC) primarily at Serine-19 and further at Theronine-18 in vertebrates (Serine-21 and threonine-20 in *Drosophila*)(ref) [20, 21]. Phosphorylation at these two sites increases actin-activated myosin ATPase activity [22] and is important for regulation of actin reorganization and contractility [21, 23, 24]. The diphosphorylated form of MRLC has higher activity than the monophosphorylated form [25]. A second function of Rho-kinase is to phosphorylate and inactivate myosin light chain phosphatase, which dephosphorylates and inactivates MRLC [26]. Thus, the net effect of activating Rho is an increase in the phosphorylation of MRLC. In turn, phosphorylated MRLC can activate myosin heavy chain, allowing the myosin complex to move along actin filaments and generate contractile force essential for cell migration and cell morphology changes (Figure 1.3).

In summary, previous studies have shown that nonmuscle myosin II plays an important role during ecdysone directed leg imaginal disc elongation and eversion, which are processes largely driven by cell shape changes and cell rearrangements. The activation of myosin is likely under the control of Rho signaling during imaginal disc morphogenesis. In chapter 2, I present my work on the investigation of the expression pattern of the phosphorylated forms of MRLC in imaginal discs and embryos, and the effect of perturbing Rho signaling on phospho MRLC expression.

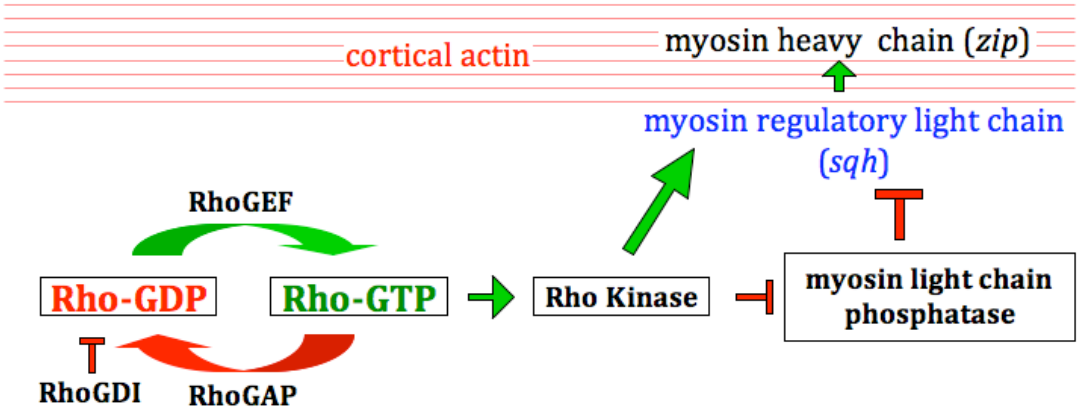

Figure 1.3
Central part of the Rho signaling pathway.
Drosophila gene names are given in parentheses. (Adapted from Ward et al 2003 [11].)

Part II. Tracheal morphogenesis in *Drosophila*

Organs composed of networks of branched tubes play essential roles in the transport of liquids and gasses in all animals. Examples include the kidney, lung and vascular system of mammals and the tracheal system of insects. In general, these organs are well-ordered structures with stereotypic developmental patterns. Maturation of these organs during development yields tubes of appropriate shapes and sizes to support the fluid or gas movement throughout the organ. Continued growth of these organs after birth is also critical to support the needs of a rapidly growing animal, as postnatal hypotrophy of organs including the lung and kidney can be pathological [27, 28]. The larval tracheal system of *Drosophila melanogaster* is an excellent model, not only for the stereotypic patterning of a branched tubular organ, but also for its maturation into a functional organ and its ability to expand in size and complexity as the animal grows.

Branching processes of the *Drosophila* tracheal system during embryogenesis have been studied extensively [29-35]. At stage 5 (the blastodermal stage), ~20 clusters of tracheal precursor cells (placodes) are specified in the future ectoderm, one on each side of the body segments T2-T3 and A1-A8. There are ~20 cells in each tracheal placode. At late stage 10/early stage 11, the placodes start invaginating and form sac-like structures (often referred to as tracheal pits) (Figure 1.4 A). During this process, the tracheal

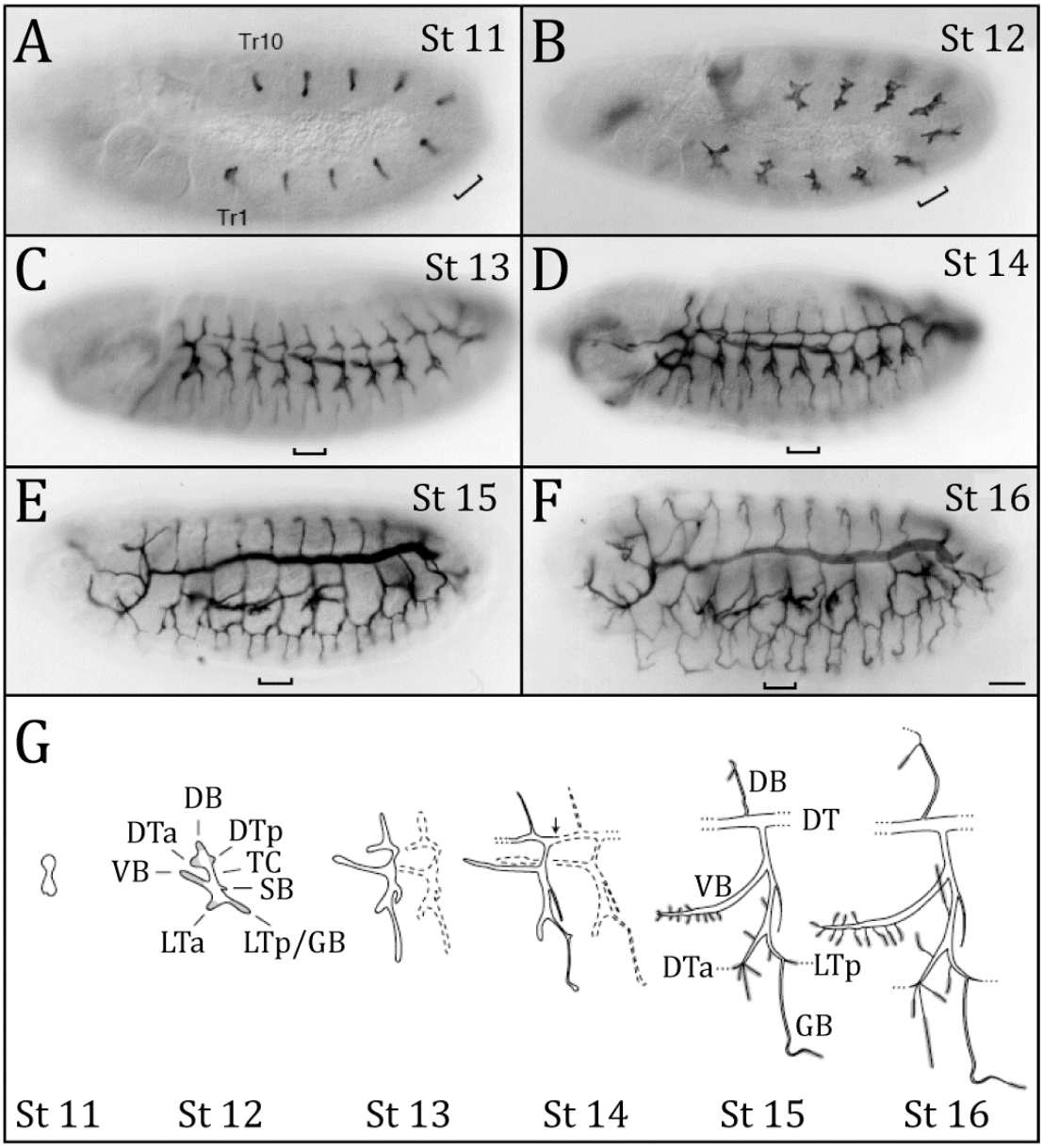

Figure 1.4
Tracheal branching morphogenesis during *Drosophila* embryogenesis (adapted from Samakovlis et al. 1996 [35])
(A-F) Lateral view of embryonic tracheal development from stage 11 to stage 16. The embryos are immunostained with antisera against the tracheal lumen. The brackets indicate the position of the 5th tracheal metamere (Tr5, in body segment A3). Anterior is left and dorsal is up in all figures.
(G) Schematic drawing of Tr5 development. Transverse connective (TC), spiracular branch (SB) and the six primary branches are indicated in stage 12 and stage 15.

precursor cells divide twice, resulting in ~80 cells in each unit (referred to as tracheal metamere) and ~1600 cells in the entire tracheal system. No additional cell divisions occur during later embryonic and larval stages of tracheal morphogenesis. Then, each tracheal pit goes through similar branching processes (Figure 1.4). At stage 12, the primary branches sprouting out from a pit are dorsal branch (DB), dorsal trunk anterior/posterior (DTa/p), visceral branch (VB), lateral trunk anterior (LTa), lateral trunk posterior and ganglionic branch (LTp/GB). The region between DT and LT is the transverse connective (TC), which contains cells that do not bud out from the tracheal pit. The spiracular branch (SB) is formed by cells remaining at the tracheal placode invaginating path, thus connecting the trachea to epidermis. At stage 14, the DTa/ps become interconnected with their partners, forming the two longest and thickest tubes running from anterior to posterior of the animal. The very posterior ends of the fused DTs connect with posterior spiracles, which are the only openings to air. At stage 15, the primary branches produce secondary branches from stereotyped positions. Also, the LTa/p fuse with the LTa/p in the neighboring segments. At stage 16, the DBs on both sides of each segment fuse together, connecting the left side and right side of the network [34]. By this time, the highly stereotyped tracheal network consisting the primary and secondary branches is completely formed. During later stages of embryogenesis and in the following larval stages, each secondary branch can send out hundreds of variable

terminal branches (tracheoles) reaching target tissues and organs in response to the oxygen needs.

Another critical process during tracheal morphogenesis is tracheal tube maturation (see more detailed description in chapter 2). At stage 13, the nascent tracheal tubes are very thin and filled with fluid. The tracheal epithelial cells then secrete chitinous solid materials along with some proteins and enzymes into the lumen, which together help with proper expansion of the tube diameter and length. Starting from stage 16, the luminal solids are cleared through endocytosis, leaving behind liquid-filled tubes again. Right before hatching (late stage 17), the liquids in the tracheal tubes are rapidly cleared, followed by immediate gas filling. At this point, the tracheal system is ready to carry out the function of distributing air efficiently.

During larval stages, the tracheal system has to expand in both length and diameter coordinately with overall growth of the whole body to meet the oxygen demands of the fast growing animal. Tracheal length increases in a continuous mode. In contrast, tracheal diameters only increase after each larval molt [30]. The apical surfaces of the tracheal tubes are covered with well-organized cuticular lining (intima) that provides mechanical support and prevents dehydration and microbial invasion. Possibly, this cuticular lining also prevents increases of tracheal diameter between molts. Before each larval molt, the old lining is detached from the tracheal cells, allowing the tracheal tubes to widen. Then, the tracheal cells secrete a new layer of intima on the apical surface of the

tube. The space between the old and new intima is filled with molting fluids [36]. During molting, the new intima becomes air inflated; the old intima collapses and is expelled through the temporarily opened spiracular branch (SB) in each segment (the intima in the 10th segment is expelled through the posterior spiracle) (Figure 1.5).

In chapter 3, I describe the cloning and initial characterization of *uninflatable* (*uif*), a novel gene that encodes a type I transmembrane protein expressed in the ectodermally derived epithelial cells. The large extracellular domain contains carbohydrate binding and cell signaling motifs, whereas the small intracellular domain is devoid of any conserved domains. *uif* mutant animals have defects in embryonic tracheal inflation and larval tracheal growth and molting. Interestingly, *uif* also plays a role in imaginal disc development and is possibly a regulator of Notch activation.

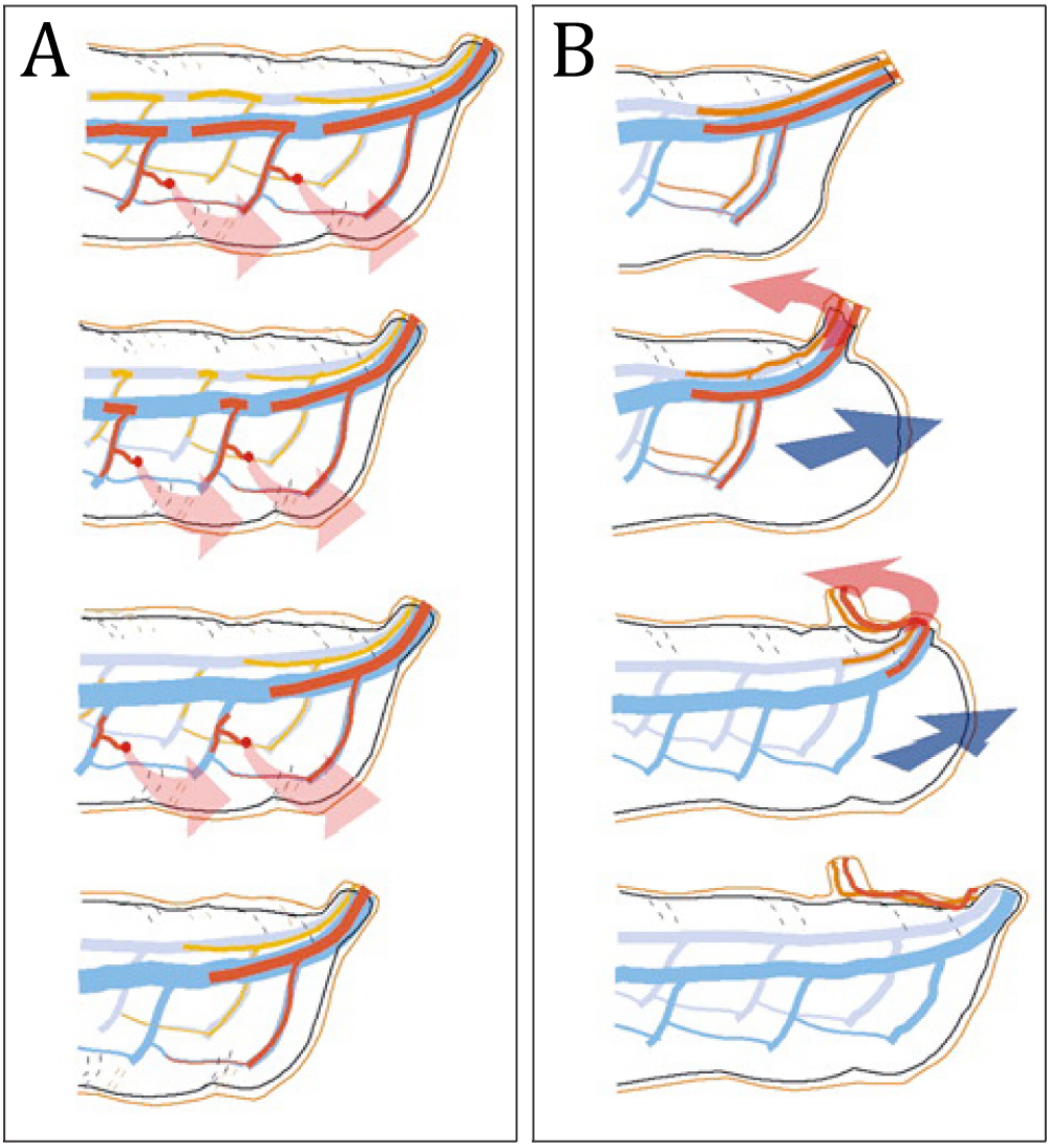

Figure 1.5
Larval tracheal molting (adapted from Park et al. 2002 [36])
(A) Shedding of the old intima in Tr1-Tr9 is through segmental SBs.
(B) The old intima of Tr10 is expelled from the posterior spiracles.

References

1. Silverthorn, D.U. (2007). Human physiology : an integrated approach, 4th Edition, (San Francisco: Pearson/Benjamin Cummings).
2. Mester, J., and Redeuilh, G. (2008). Proliferation of breast cancer cells: regulation, mediators, targets for therapy. Anti-cancer agents in medicinal chemistry *8*, 872-885.
3. Bai, Z., and Gust, R. (2009). Breast cancer, estrogen receptor and ligands. Archiv der Pharmazie *342*, 133-149.
4. Thummel, C.S. (1996). Files on steroids--Drosophila metamorphosis and the mechanisms of steroid hormone action. Trends Genet *12*, 306-310.
5. Thummel, C.S., and Chory, J. (2002). Steroid signaling in plants and insects--common themes, different pathways. Genes & development *16*, 3113-3129.
6. Fristrom, D.K., and Fristrom, J.W. (1993). The metamorphic development of the adult epidermis in *The development of Drosophila melanogaster* , M. Bate and A. Martinez Arias, (Cold Spring Harbor, NY).
7. Pastor-Pareja, J.C., Grawe, F., Martin-Blanco, E., and Garcia-Bellido, A. (2004). Invasive cell behavior during Drosophila imaginal disc eversion is mediated by the JNK signaling cascade. Developmental cell *7*, 387-399.
8. Fristrom, D., and Chihara, C. (1978). The mechanism of evagination of imaginal discs of Drosophila melanogaster. V. Evagination of disc fragments. Developmental biology *66*, 564-570.
9. Fristrom, D. (1976). The mechanism of evagination of imaginal discs of Drosophila melanogaster. III. Evidence for cell rearrangement. Developmental biology *54*, 163-171.
10. Taylor, J., and Adler, P.N. (2008). Cell rearrangement and cell division during the tissue level morphogenesis of evaginating Drosophila imaginal discs. Developmental biology *313*, 739-751.
11. Ward, R.E., Evans, J., and Thummel, C.S. (2003). Genetic modifier screens in Drosophila demonstrate a role for Rho1 signaling in ecdysone-triggered imaginal disc morphogenesis. Genetics *165*, 1397-1415.
12. Bayer, C.A., Halsell, S.R., Fristrom, J.W., Kiehart, D.P., and von Kalm, L. (2003). Genetic interactions between the RhoA and Stubble-stubbloid loci suggest a role for a type II transmembrane serine protease in intracellular signaling during Drosophila imaginal disc morphogenesis. Genetics *165*, 1417-1432.
13. DiBello, P.R., Withers, D.A., Bayer, C.A., Fristrom, J.W., and Guild, G.M. (1991). The Drosophila Broad-Complex encodes a family of related proteins containing zinc fingers. Genetics *129*, 385-397.

14. Kiss, I., Beaton, A.H., Tardiff, J., Fristrom, D., and Fristrom, J.W. (1988). Interactions and developmental effects of mutations in the Broad-Complex of Drosophila melanogaster. Genetics *118*, 247-259.
15. Condic, M.L., Fristrom, D., and Fristrom, J.W. (1991). Apical cell shape changes during Drosophila imaginal leg disc elongation: a novel morphogenetic mechanism. Development (Cambridge, England) *111*, 23-33.
16. Gotwals, P.J., and Fristrom, J.W. (1991). Three neighboring genes interact with the Broad-Complex and the Stubble-stubbloid locus to affect imaginal disc morphogenesis in Drosophila. Genetics *127*, 747-759.
17. Edwards, K.A., and Kiehart, D.P. (1996). Drosophila nonmuscle myosin II has multiple essential roles in imaginal disc and egg chamber morphogenesis. Development (Cambridge, England) *122*, 1499-1511.
18. Etienne-Manneville, S., and Hall, A. (2002). Rho GTPases in cell biology. Nature *420*, 629-635.
19. Johndrow, J.E., Magie, C.R., and Parkhurst, S.M. (2004). Rho GTPase function in flies: insights from a developmental and organismal perspective. Biochemistry and cell biology = Biochimie et biologie cellulaire *82*, 643-657.
20. Kosako, H., Yoshida, T., Matsumura, F., Ishizaki, T., Narumiya, S., and Inagaki, M. (2000). Rho-kinase/ROCK is involved in cytokinesis through the phosphorylation of myosin light chain and not ezrin/radixin/moesin proteins at the cleavage furrow. Oncogene *19*, 6059-6064.
21. Ueda, K., Murata-Hori, M., Tatsuka, M., and Hosoya, H. (2002). Rho-kinase contributes to diphosphorylation of myosin II regulatory light chain in nonmuscle cells. Oncogene *21*, 5852-5860.
22. Ikebe, M., Koretz, J., and Hartshorne, D.J. (1988). Effects of phosphorylation of light chain residues threonine 18 and serine 19 on the properties and conformation of smooth muscle myosin. The Journal of biological chemistry *263*, 6432-6437.
23. Padash Barmchi, M., Rogers, S., and Hacker, U. (2005). DRhoGEF2 regulates actin organization and contractility in the Drosophila blastoderm embryo. The Journal of cell biology *168*, 575-585.
24. Sakurada, K., Seto, M., and Sasaki, Y. (1998). Dynamics of myosin light chain phosphorylation at Ser19 and Thr18/Ser19 in smooth muscle cells in culture. The American journal of physiology *274*, C1563-1572.
25. Ikebe, M. (1989). Phosphorylation of a second site for myosin light chain kinase on platelet myosin. Biochemistry *28*, 8750-8755.
26. Kimura, K., Ito, M., Amano, M., Chihara, K., Fukata, Y., Nakafuku, M., Yamamori, B., Feng, J., Nakano, T., Okawa, K., et al. (1996). Regulation of myosin phosphatase by Rho and Rho-associated kinase (Rho-kinase). Science (New York, N.Y *273*, 245-248.

27. Kerecuk, L., Schreuder, M.F., and Woolf, A.S. (2008). Renal tract malformations: perspectives for nephrologists. Nat. Clin. Pract. Nephrol. *4*, 312-325.
28. Shi, W., Bellusci, S., and Warburton, D. (2007). Lung development and adult lung diseases. Chest *132*, 651-656.
29. Cabernard, C., Neumann, M., and Affolter, M. (2004). Cellular and molecular mechanisms involved in branching morphogenesis of the Drosophila tracheal system. J Appl Physiol *97*, 2347-2353.
30. Beitel, G.J., and Krasnow, M.A. (2000). Genetic control of epithelial tube size in the Drosophila tracheal system. Development (Cambridge, England) *127*, 3271-3282.
31. Ghabrial, A., Luschnig, S., Metzstein, M.M., and Krasnow, M.A. (2003). Branching morphogenesis of the Drosophila tracheal system. Annual review of cell and developmental biology *19*, 623-647.
32. Uv, A., Cantera, R., and Samakovlis, C. (2003). Drosophila tracheal morphogenesis: intricate cellular solutions to basic plumbing problems. Trends in cell biology *13*, 301-309.
33. Swanson, L.E., and Beitel, G.J. (2006). Tubulogenesis: an inside job. Curr Biol *16*, R51-R53.
34. Hartenstein, V. (1993). Atlas of *Drosophila* development, (Cold Spring Harbor, NY).
35. Samakovlis, C., Hacohen, N., Manning, G., Sutherland, D.C., Guillemin, K., and Krasnow, M.A. (1996). Development of the Drosophila tracheal system occurs by a series of morphologically distinct but genetically coupled branching events. Development (Cambridge, England) *122*, 1395-1407.
36. Park, Y., Filippov, V., Gill, S.S., and Adams, M.E. (2002). Deletion of the ecdysis-triggering hormone gene leads to lethal ecdysis deficiency. Development (Cambridge, England) *129*, 493-503.

Chapter 2

Distinct subcellular localizations of differently phosphorylated forms of the myosin regulatory light chain

Introduction

Nonmuscle myosin II (referred to as myosin hereafter) is a motor protein that can bind reversibly to actin filaments and generate essential contractile forces in various cellular processes such as intracellular vesicle transport, cytokinesis, maintenance of cell morphology and polarity, cell shape change and cell movements (reviewed in [1]). Loss-of-function mutations of myosin in various organisms result in severe developmental defects and are inevitably lethal. For example, in *Dictyostelium*, mutant cells that lack myosin heavy chain or regulatory light chain undergo cytokinesis with greatly decreased efficiency, have dramatic reduction of cell polarity and greatly reduced motility, cease development after aggregation and fail to form fruiting bodies (reviewed in [2]). In *Drosophila*, strong loss-of-function alleles of myosin heavy chain (encoded by *zipper* (*zip*) gene) are embryonic lethal with defects in axon patterning, dorsal closure, and head involution [3, 4]. Hypomorphic *zip* alleles produce malformed adult legs due to defects in cell shape changes during imaginal disc morphogenesis [5, 6]. Mutations in myosin regulatory light chain (encoded by

spaghetti squash (*sqh*) gene) result in disrupted cytokinesis, leg disc eversion, eye morphogenesis, and oogenesis [7, 8].

Myosin molecules are hexamers composed of a pair of heavy chains (MHC), a pair of essential light chains, and a pair of regulatory light chains (MRLC) [9]. Activity of myosin is mainly controlled by phosphorylation and dephosphorylation of MRLC (reviewed in [10]). Phosphorylation of Ser-19 on MRLC (Ser-21 on Sqh) can greatly increase the actin-dependent myosin ATPase activity and motor activity of myosin [11]. Subsequent phosphorylation of Thr-18 (Thr-20 on Sqh) can further increase myosin activity [11-13]. Protein kinases including myosin light chain kinase (MLCK), Rho-associated protein kinase (ROK), Rho-dependent Citron kinase, AMP-activated kinase, leucine zipper interacting kinase (ZIPK) and myotonic dystrophy kinase-related CDC42-binding kinase can phosphorylate and activate MRLC [10, 14-18]. Antagonistically, myosin phosphatase dephosphorylates MRLC, leading to inactivation of myosin [19, 20].

To monitor the activation of myosin during develop and identify upstream regulators of myosin activity, we developed two phosphorylation site-specific antibodies against the phosphorylated forms of Sqh. We performed immunostaining with these antibodies and observed that Sqh1P mainly localizes to the adherens junction in imaginal disc cells, whereas Sqh2P mainly localizes to the apical domain of the cells. In the embryos, Sqh1P is ubiquitously expressed while Sqh2P is only expressed in places undergoing extensive cell

shape change or cell movement. Interestingly, in the leading edge cells of the migrating lateral epidermis during dorsal closure, Sqh1P localizes in a "bars-on-a-string" pattern on the actomyosin cable, whereas Sqh2P localizes in the filopodial protrusions. We also examined the effect of perturbing Rho signaling activation on the expression of Sqh1P and Sqh2P in imaginal discs by generating homozygous *Rho kinase* (*Rok*) mutant clones. In late 3rd instar and white prepual imaginal discs, distributions and levels of Sqh1P and Sqh2P are not obviously affected in *Rok* clones.

Materials and methods

Drosophila strains

yw cv sqh^{AX3}; P{sqh-GFP} and *yw, sqh^{AX3}, FRT101/FM7C* fly lines were generous gifts from Anne Royou and Roger Karess [21]. *Rho$^{E(br)264}$* line was described in Ward et al., 2003 and Patch et al., 2009 [22, 23]. Other stocks were obtained from Bloomington *Drosophila* Stock Center (Bloomington, IN). *w^{1118}* was used as the wild type strain for the experiments conducted in this study. All *Drosophila* stocks were maintained on media consisting of corn meal, sugar, yeast, and agar in incubators maintained at a constant temperature of 21°C or in a room that typically fluctuated between 21°C and 22.5°C. Genetic experiments were conducted in incubators controlled at a constant temperature of 25ºC.

Generation of antibodies

To generate phosphorylation site-specific antibodies, two peptides were commercially synthesized corresponding to regions of the Sqh protein with phosphorylated derivatives at Serine-21 or Threonine-20/Serine-21. The sequences of the peptides used were Sqh1P: A-Q-R-A-T-S*-N-V-F-A-M and Sqh2P: A-Q-R-A-T*-S*-N-V-F-A-M (* indicates phosphorylated amino acid). These peptides were then conjugated to Keyhole limpet hemocyanin (KLH) and

used to immunize animals. The Sqh1P peptide was synthesized at Pocono Rabbit Farm and Laboratory Inc. (PRF&L, Canadensis, PA) and used to immunize guinea pigs. The guinea pig anti-Sqh1P serum was subsequently affinity purified at PRF&L. The Sqh2P peptide was synthesized at the Immunological Resource Center at the University of Illinois and used to immunize rats. To generate antiserum against Sqh, full length Sqh was cloned into a PGEX2TK vector. The protein was over expressed in *E.Coli* BL21 cells, then purified and used immunize mice at PRF&L.

Gel electrophoreses and immunoblotting

SDS PAGE was performed according to standard procedures [24]. ~25 imaginal discs from wandering 3rd instar larvae were hand dissected in cold fresh PBS. The discs were collected in 1.5ml centrifuge tubes and homogenized in 1x SDS-PAGE sample buffer (~1 wing disc per μl buffer) and boiled for 5 minutes. 20μl samples were loaded in each lane of 12% polyacrylamide gels and eletrophoresed at 120 V. The proteins on the gel were transferred to PVDF membranes (Bio-Rad Laboratories, Hercules, CA) overnight at 30V or for 1 hour at 100V at 4°C in transfer buffer (25mM Tris, 192mM Glycine and 20% methanol) and followed with immunoblotting procedure described below.

Phosphatase treatment of protein samples was done by homogenizing imaginal discs in 1xPBS with protease inhibitors (0.1mM PMSF, 10μM leupeptin)

(~1.5wing discs/μl PBS), followed by treatment of the disc lysates with 0.025unit/μl protein phosphatase 1(PP1) (New England Biolabs, Ipswich, MA) for the indicated times.

Urea-glycerol-PAGE and immuno blotting was adapted from Seto et al., 1990 [25]. Imaginal discs from wondering 3rd instar larvae were hand dissected in fresh PBS. ~20 wing discs plus associated leg and halter discs were homogenized in 20μl urea sample buffer (20mM Tris pH 8.6, 22 mM glycine, 10mM DTT, 8M urea, 0.1% bromophenol blue). The glycerol-polyacrylamide gels contained 20mM Tris pH 8.6, 23mM glycine, 40% glycerol, 15% acrylamide and 0.75% Bis. Reservoir buffer contained 20mM Tris pH 8.6, 23mM glycine, 1mM sodium thioglycolate, 1mM DTT. The gels were pre-electrophoresed for 1 hour at 400V in 4°C. Then the disc samples were loaded and eletrophoresed for 5 hours at 400V in 4°C. The proteins on the gel were transferred to PVDF membranes (Bio-Rad Laboratories, Hercules, CA) overnight at 30V (4°C) in transfer buffer containing 20mM Tris (pH 7.5) and 20% methanol and followed with immunoblotting procedure described below.

Immunoblotting of all blots were started with blocking in 1xTBS (0.1M NaCl, 0.02M Tris, pH7.5~7.6) plus 0.1% Tween20 and 5% nonfat dry milk (blocking buffer) for 1 hour in room temperature, then incubated with primary antibodies in blocking buffer overnight at 4°C. After three quick rinses and three 15-minute washes with 1XTBS plus 0.1% Tween20, the blots were incubated with HRP-conjugated secondary antibodies in blocking buffer for 2~3 hours at

room temperature. After three quick rinses and three 15-minute washes with 1XTBS plus 0.1% Tween20, the blots were then developed with SuperSignal West Pico Chemiluminescent Substrate (Thermo Fisher Scientific Inc., Rockford, IL) for 1 minute. Chemiluminescence signal was detected on KODAC imaging station or exposed to X-ray film, developed and scanned.

The following antibodies were used at indicated dilutions: mouse anti-Sqh (1:5000), affinity purified guinea pig anti-Sqh1P (1:1000), rat anti-Sqh1P (1:3000), mouse anti-Coracle (1:1000) [26]. HRP-conjugated secondary antibodies (Jackson ImmunoResearch Laboratories Inc., West Grove, PA) were used at 1:5000.

Immunohistochemistry

Imaginal discs were hand dissected from wandering 3rd instar larvae or prepupae in fresh PBS, then fixed immediately in 4% paraformaldehyde for 20 minutes. Embryos were collected and processed for antibody staining as described [26]. The following antibodies were used at the given dilutions: mouse anti-Sqh 1:3000, affinity purified guinea pig anti-Sqh1P 1:500, rat anti-Sqh2P 1:3000, mouse anti-Crumbs 1:100 (clone Cq4 from Developmental Studies Hybridoma Bank at the University of Iowa), mouse anti-Armadillo 1:100 (clone N27A1, DSHB), mouse anti-Coracle 1:400 (gift from Richard Fehon, University of Chicago [14]). Secondary antibodies were obtained from Jackson

ImmunoResearch Laboratories (West Grove, PA) and used at 1:400. Confocal images were aquired on a Zeiss LSM510 Meta Laser Scanning Confocal Microscope (Carl Zeiss Inc, Thornwood NY). Photomicrographs were adjusted for brightness and contrast with the Adobe Photoshop (version CS3, San Jose, CA), and figures were complied in Adobe Illustrator (version CS3, San Jose, CA).

Mosaic mutant clones

The FLP/FRT system[27] was used to generate sqh^{AX3} homozygous mutant clones in the ovary. To generate *sqh* clones, *yw, Ubi-GFP, FRT101/Y; hsFLP/+* males were crossed to *yw,* sqh^{AX3}*, FRT101/FM7C* virgin females. Then, *yw, ubiGFP, FRT101/yw,* sqh^{AX3}*, FRT101; hsPLF/+* 2-3 day old females were selected and heat shocked at 37°C for 1 hour. Ovaries were dissected 24 hours after heat shock. Homozygous *sqh* mutant cells are marked by the absence of ubiquitous GFP.

Rho-kinase MARCM clones were generated as described[11]. *FRT19A, tubP-GAL80, hsFLP, w; UAS-mCD8::GFP* virgin females were crossed to *yw; tubP-GAL4/TM3, Sb* males. Next, *FRT19A, tubP-GAL80, hsFLP, w /Y; UAS-mCD8::GFP /+; tubP-GAL4/+* males were crossed to *yw,* rok^{2}*, FRT19A/FM7i* virgin females to generate *yw,* rok^{2}*, FRT19A / FRT19A, tubP-GAL80, hsFLP, w; UAS-mCD8::GFP /+; tubP-GAL4/+* animals. To induce clones, first instar larvae were then heat

shocked for 1 hour at 37°C. Imaginal discs from white prepupae where dissected, fixed and stained as described above.

Results

Antibodies specific for phosphorylated forms of Sqh

We generated two site-specific antibodies against the phosphorylated forms of Sqh (MRLC in *Drosophila*) protein. One antibody is against the monophosphorylated form, Sqh1P; the other is against the diphosporylated form, Sqh2P. We also generated an antibody against full length Sqh to use as a control. To test the specificity of the antibodies, we conducted western blots on lysates from wild type imaginal discs. All three antibodies recognized a single band of ~21KD on the blots, suggesting that these antibodies are recognizing the endogenous Sqh protein (Figure 2.1 A). To confirm this notion, we tested the antibodies on protein samples extracted from *yw cv* sqh^{Ax3}*; P{sqh-GFP}* animals. sqh^{Ax3} is an amorphic allele that produces no Sqh protein [21], whereas *sqh-GFP* encodes a GFP tagged Sqh protein with a predicted molecular weight of ~48 KD. Consistently, the 21KD band was absent and a band of approximately 48KD was detected on blots of these samples (Figure 2.1 A).

We performed Urea-glycerol-PAGE followed by immunoblotting to further demonstrate the specificity of the antibodies. Urea-glycerol-PAGE separates acidic proteins based on their native charges instead of molecular weight [28]. Thus, differently phosphorylated forms of Sqh proteins can be efficiently separated on this type of gels and then transferred to PVDF

membrane for immunoblotting. On the blot probed with an antibody against total Sqh protein, three bands were clearly visible. From top to bottom, these bands represent nonphosphorylated, monophosphorylated and diphosphorylated forms of the Sqh protein respectively (Figure 2.1 B). On blots probed with anti-Sqh1P or anti-Sqh2P antibodies, only a single band showed up (Figure 2.1 B, C). To confirm that the single band represents either Sqh1P or Sqh2P specifically, we re-probed these blots with the anti-Sqh antibody and visualized the presence of the other two bands at expected positions (data not shown). These blots also revealed that only a small proportion of total Sqh proteins are phosphorylated in late larval imaginal discs and the monophosphorylated form, Sqh1P is the dominant form of phosphorylated Sqh.

To further demonstrate the specificity of the antibodies against the phosphorylated forms of Sqh, we performed time course experiments in which we treated protein samples from wild type imaginal discs with protein phosphatase 1 (PP1). PP1 is a general phosphatase that dephosphorylates phospho-serine and phospho-threonine residues, and thus is predicted to be able to dephosphorylate Thr20 and Ser21 on endogenous Sqh. On western blots, we observed that the signal of both Sqh1P and Sqh2P decreased significantly after PP1 treatment, whereas the expression of Coracle, a cytoplasmic protein used as control for protein stability was unaffected during the time course (Figure 2.1 C, D).

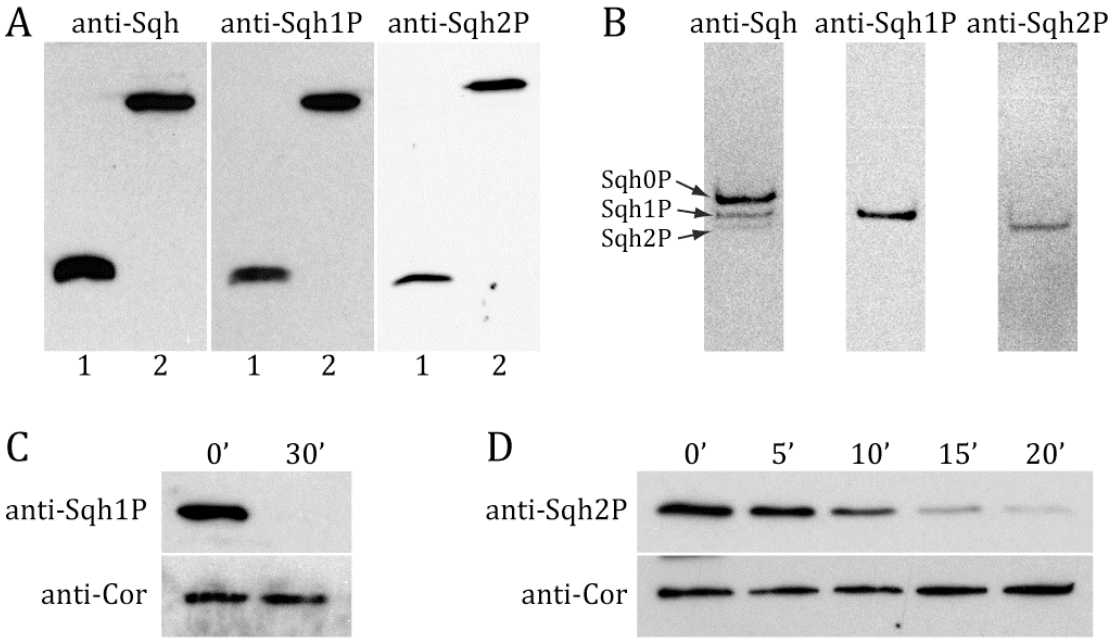

Figure 2.1
Demonstration of the specificity of antibodies against Sqh1P and Sqh2P.
(A) Western immunoblots incubated with anti-Sqh, anti-Sqh1P or anti-Sqh2P antibodies. Lane 1 of each blot contains protein lysate extracted from imaginal discs of w^{1118} (wild type) 3rd instar larvae. Lane 2 of each blot contains lysate extracted from imaginal discs of *yw cv* sqh^{Ax3}*; P{sqh-GFP}* 3rd instar larvae. The bottom band is ~ 21 KD on each blot, whereas the top band is ~ 48 KD.
(B) Western immunoblots of w^{1118} 3rd instar larval lysates separated by urea-glycerol-PAGE. Anti-Sqh antiserum detects three protein forms (arrows) corresponding to nonphosphorylated, monophosphorylated and diphosphorylated Sqh (from top to bottom). Antibodies against Sqh1P or anti-Sqh2P detect only a single protein species.
(C, D) Phosphatase treatment of w^{1118} 3rd instar larval lysates reveals that the antibodies against Sqh1P and Sqh2P specifically recognize phosphorylated proteins. Protein samples were treated with PP1 for the indicated time. Coracle was used as a control for loading and transfer. Note the strong reductions of Sqh1P (C, top panel) and Sqh2P (D, top panel) after PP1 treatment.

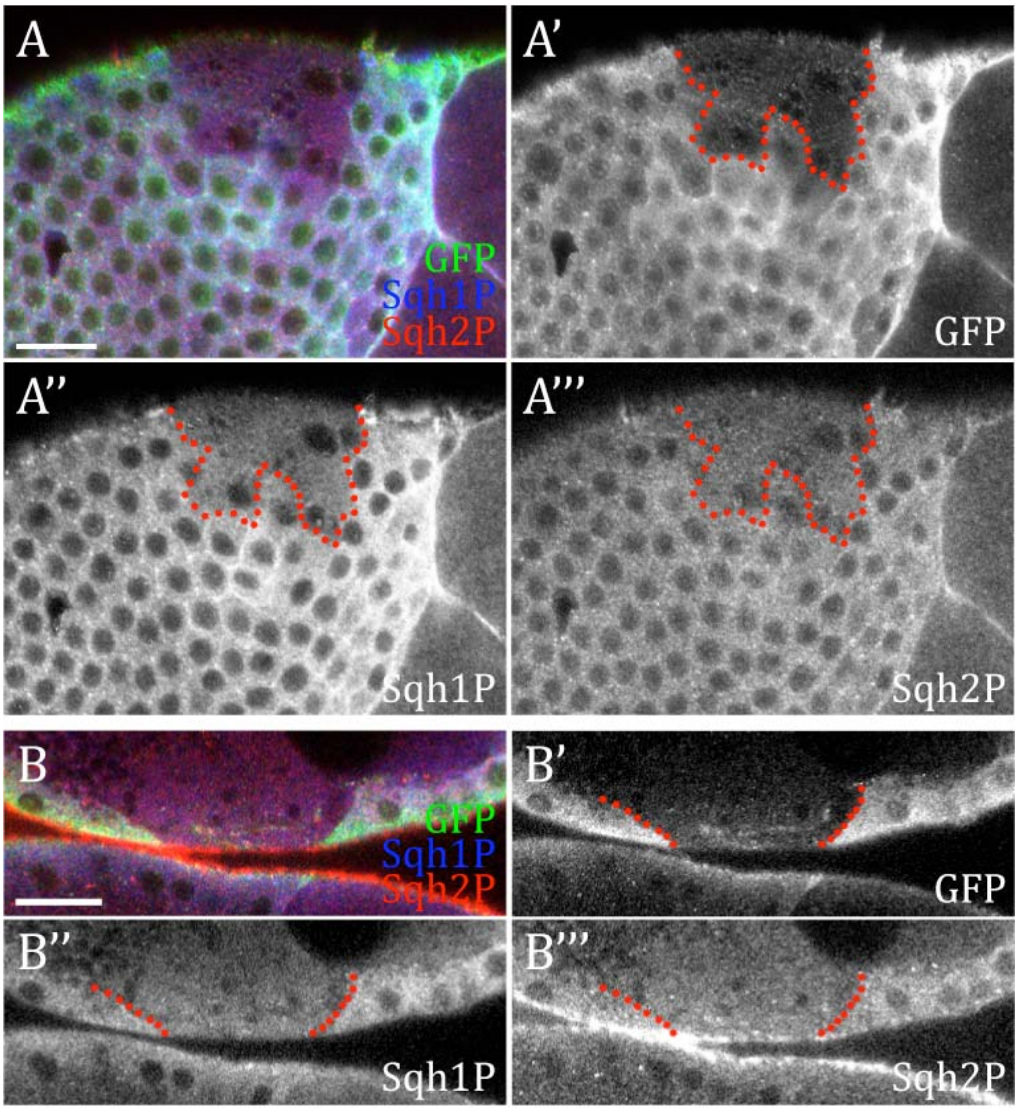

Figure 2.2
Sqh1P and Sqh2P levels are strongly reduced in follicle cell clones of *sqh^{AX3}*.
(A) Confocal optical section of the surface of the follicular epithelium in an ovary stained with antibodies against GFP (green, and singly labeled in A'), Sqh1P (blue, and in A") and Sqh2P (red, and in A"') antibodies. Red dotted lines indicate the boundary between mutant and wild type cells. The absence of GFP indicates a clone of cells homozygous for the null allele *sqh^{AX3}*. Note that Sqh1P and Sqh2P are strongly reduced in the mutant cells.
(B) Confocal optical section of a sagittal view of a *sqh^{AX3}* follicle cell clone, stained in the same manner as shown in A. Both Sqh1P and Sqh2P levels are reduced in *sqh^{AX3}* homozygous mutant cells, which are marked by absence of GFP.
(Scale bars = 20μm)

Next, we tested the specificity of the antibodies on immunostaining of *Drosophila* tissues. We generated *sqh*^{AX3} homozygous mutant clones in follicle cells in the ovary and stained the tissue with Sqh1P and Sqh2P antibodies. We observed clearly decreased levels of both Sqh1P and Sqh2P in the homozygous mutant cells compared to the heterozygous background tissue (Figure 2.2). Taken together, the immunoblots and immunostaining demonstrate the specificity of the Sqh1P and Sqh2P antibodies for the phosphorylated forms of the MRLC in *Drosophila*.

Sqh1P and Sqh2P have distinct subcellular localization in imaginal discs

Using the antibodies we developed, we first examined the distribution of Sqh1P and Sqh2P in the imaginal discs of late 3rd instar larvae, and observed that Sqh1P and Sqh2P have different subcellular localizations (Figure 2.3 A). Sqh1P appeared to be uniform in the imaginal disc and outlined the cells (Figure 2.3 A'), whereas Sqh2P strongly localized to the epithelial folds (Figure 2.3 A''). There was little overlapping between Sqh1P and Sqh2P. The epithelial cells of imaginal discs are highly polarized. From apical to basal, there are cell junctions including marginal zone (MZ), adherens junction (AJ) and septate junction (SJ) on the lateral membrane (Figure 2.3 B) [29]. At the center of a fold is the juxtaposition of two apical surfaces, with lateral junctions spreading basally on both sides of the fold (schematic drawing in Figure 2.3 C). Thus, the staining pattern indicates

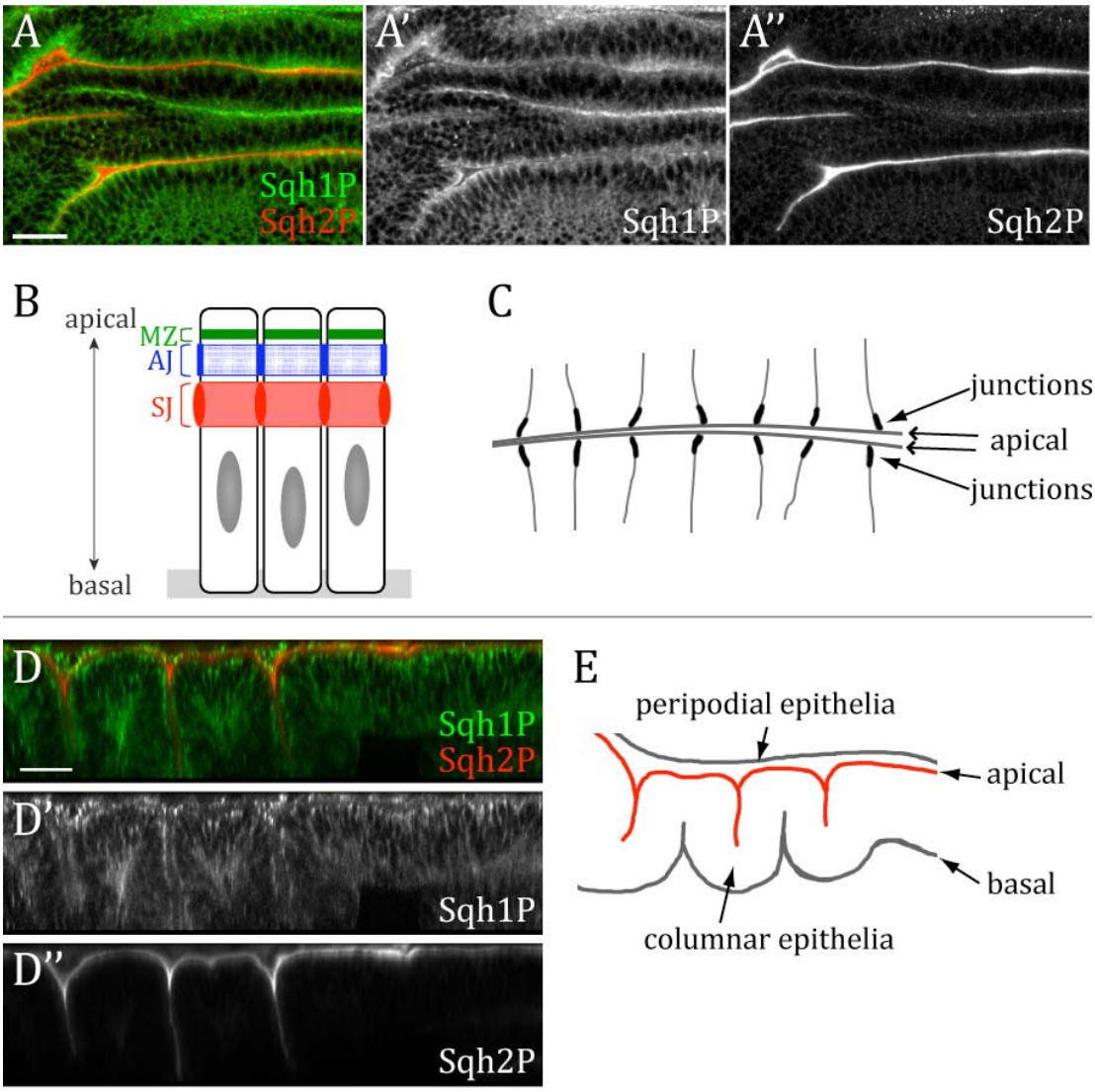
A
Sqh1P
Sqh2P
A'
Sqh1P
A''
Sqh2P
B
apical
MZ
AJ
SJ
basal
C
junctions
apical
junctions
D
Sqh1P
Sqh2P
D'
Sqh1P
D''
Sqh2P
E
peripodial epithelia
apical
basal
columnar epithelia

Figure 2.3
Sqh1P and Sqh2P have distinct subcellular localizations in wing imaginal discs.
(A-A'') Confocal optical section of a 3rd instar wing disc stained with antibodies against Sqh1P (green, and in A') and Sqh2P (red, and in A").
(B) Schematic illustration of the wing epithelium. On the apico-lateral membrane is a marginal zone (MZ), an adherens junction (AJ) and a septate junction (SJ).
(C) Schematic illustration of a single confocal optical section through the lateral junctions as they are arrayed in the fold of the wing epithelium. The apical surfaces of the cells on both sides of the fold appear to meet at the center of the fold. Lateral junctions can then be visualized on both sides of the fold.
(D-D'') XZ projection of a Z-stack confocal image of a wing imaginal disc double labeled with antibodies against Sqh1P (green, and in D') and Sqh2P (red, and in D").
(E) Schematic illustration of a sagittal section of a wing disc. (Scale bars = 20μm)

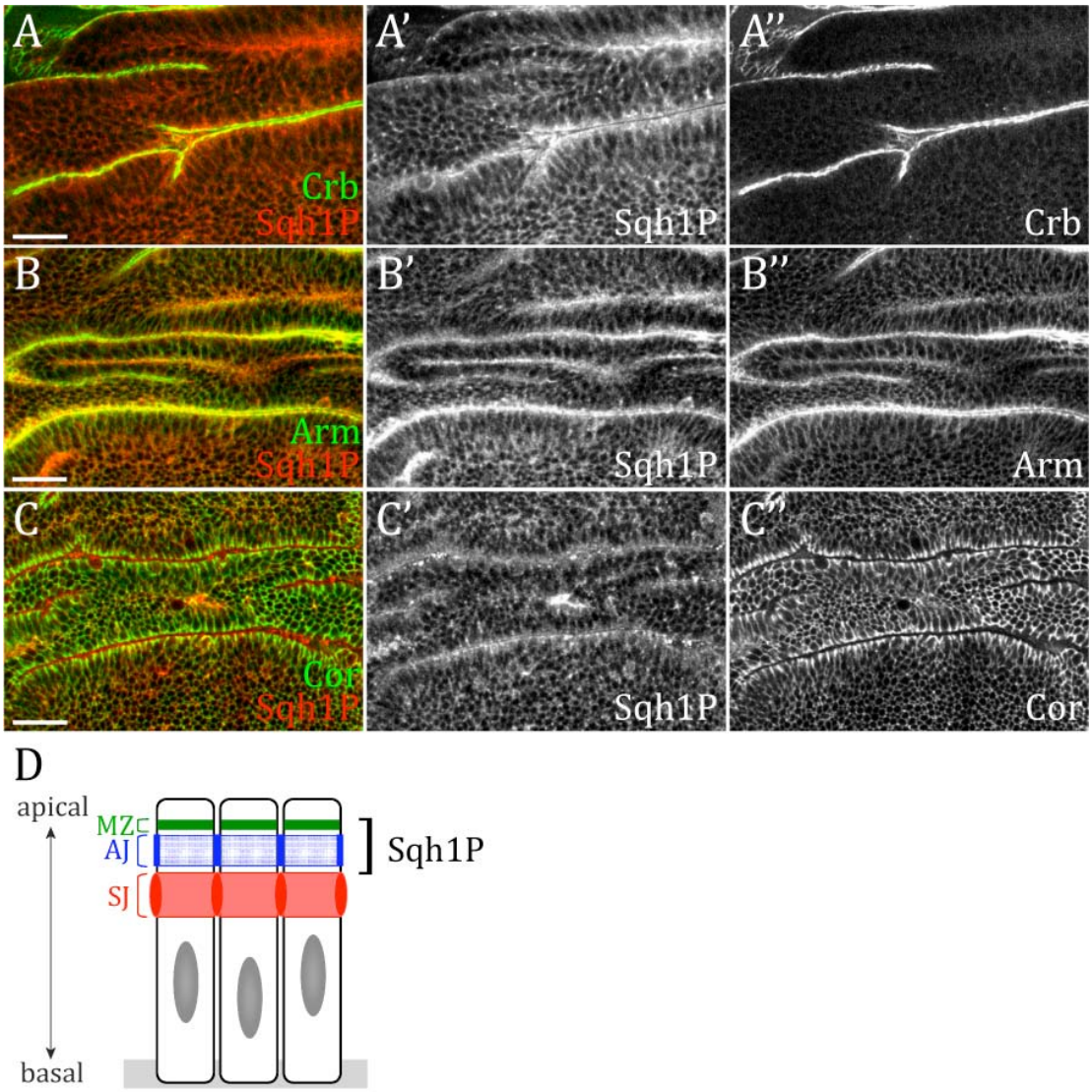

Figure 2.4
Sqh1P localizes primarily to the adherens junction in wing imaginal disc cells.
(A-C) Confocal optical sections of 3rd instar wing discs double labeled with Sqh1P (red) and Crb (green) (A), Sqh1P (red) and Arm (green) (B), and Sqh1P (red) and Cor (green) (C). Individual Sqh1P channels are shown in ', with the second antibody shown in ". Note the strongest colocalization is between Sqh1P and Arm, an adherens junction marker.
(D) Schematic illustration indicating the primary localization for Sqh1P in imaginal disc epithelial cells.
(Scale bars = 20μm)

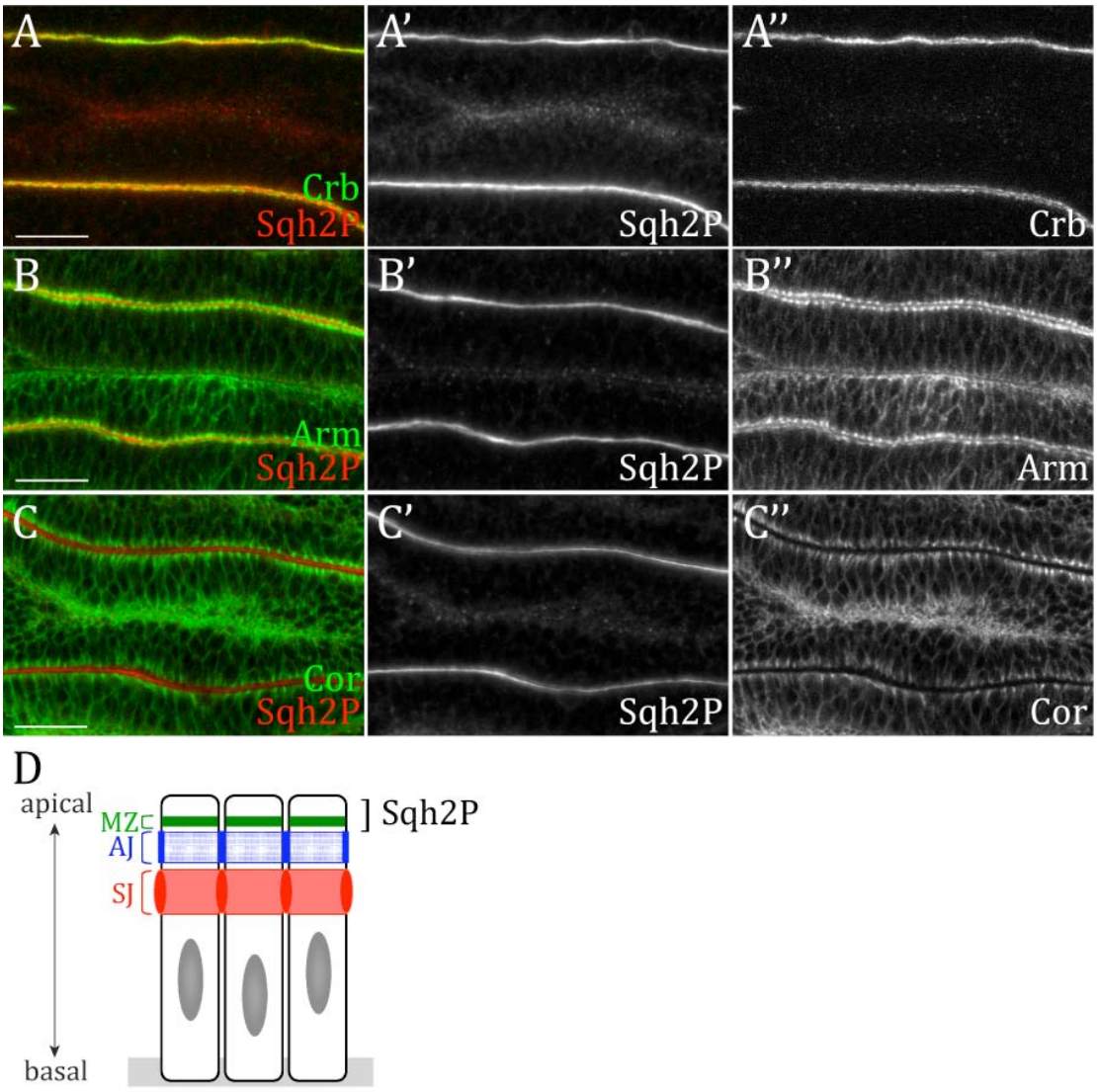

Figure 2.5
Sqh2P localizes primarily to the apical surface of wing imaginal disc cells.
(A-C) Confocal optical sections of 3rd instar wing discs double labeled with Sqh2P (red) and Crb (green) (A), Sqh2P (red) and Arm (green) (B), and Sqh2P (red) and Cor (green) (C). Individual Sqh2P channels are shown in ', with the second antibody shown in ". Note the strongest colocalization is between Sqh2P and Crb, a marginal zone marker, although Sqh2P is clearly even more apical than Crb.
(D) Schematic illustration indicating the primary localization for Sqh2P in imaginal disc epithelial cells.
(Scale bars = 20μm)

that Sqh2P is more apically localized than Sqh1P, since Sqh2P is found at the center of the folds whereas Sqh1P is found along the lateral membrane. To confirm this, we took a confocal Z-series through the whole depth of the imaginal disc. Figure 2.3 D shows the XZ projection that represents a sagittal cross section through the disc (schematic drawing shown in Figure 2.3 E). This view confirms that Sqh2P is more apically localized than Sqh1P. Moreover, sagittal cross section reveals that Sqh2P is expressed in all cells.

To further determine the subcellular localization of Sqh1P and Sqh2P, we co-stained imaginal discs with Sqh1P and Sqh2P and different cellular markers of the lateral membrane including septate junction marker Coracle (Cor), adherens junction marker Armadillo (Arm) and marginal zone maker Crumbs (Crb). We observed that Sqh1P localizes more apical than Cor, mainly co-localizes with Arm and partially co-localizes with Crb (Figure 2.4). Sqh2P localizes more apically than both Cor and Arm, and co-localizes with Crb. Interestingly, the distribution of Sqh2P includes a domain that is even more apical than Crb (Figure 2.5). Thus, Sqh1P mainly localizes to adherens junction with some expression in the marginal zone, whereas Sqh2P mainly localizes in the marginal zone and the apical plasma membrane.

Expression patterns of Sqh1P and Sqh2P in the embryos

During embryogenesis, Sqh1P can first be detected at the cleavage furrows during cellularization (Figure 2.6 A, B). The cell-outlining pattern suggests that Sqh1P mainly localizes to the cell junctions. At following stages, Sqh1P is expressed in nearly all embryonic tissues including the epidermis, foregut, hindgut, midgut, the central nerve system, and the extraembryonic amnioserosa (Figure 2.6 C-E, Figure 2.7 A-C). During all stages, the expression pattern of Sqh1P reminisces that of Zip [4, 30]. In contrast, Sqh2P can only be detected in a few places, including invaginating tissues and the tissues undergoing morphogenesis, for example, cephalic furrow at stage 6, stromodeal at stage 9, and tracheal placodes at stage 11-13 (Figure 2.6 G, H and data not shown). Sqh2P is also strongly expressed in the segmental boundaries and the pre-hair structures on the epidermis (Figure 2.6 H and data not shown).

Midway through embryogenesis (stage 12), germband retraction leaves behind a "dorsal hole", which is covered by a layer of squamous cells known as extraembryonic amnioserosa. Lateral epidermal sheets on both sides then migrate toward the mid line and close the opening (stage 13–15). This process is the last major morphogenetic movement during embryogenesis and is referred to as dorsal closure. Interestingly, Sqh1P and Sqh2P are localized differently in the leading edge cells, which are the dorsal most cells of the migrating lateral epidermis. Similar to Zip, Sqh1P is expressed in a "bars-on-a-string" distribution in the leading edge cells at all stages of dorsal closure [4, 31] (Figure 2.7 A-C). In contrast, during initiation of dorsal closure at stage 13, Sqh2P is up regulated in

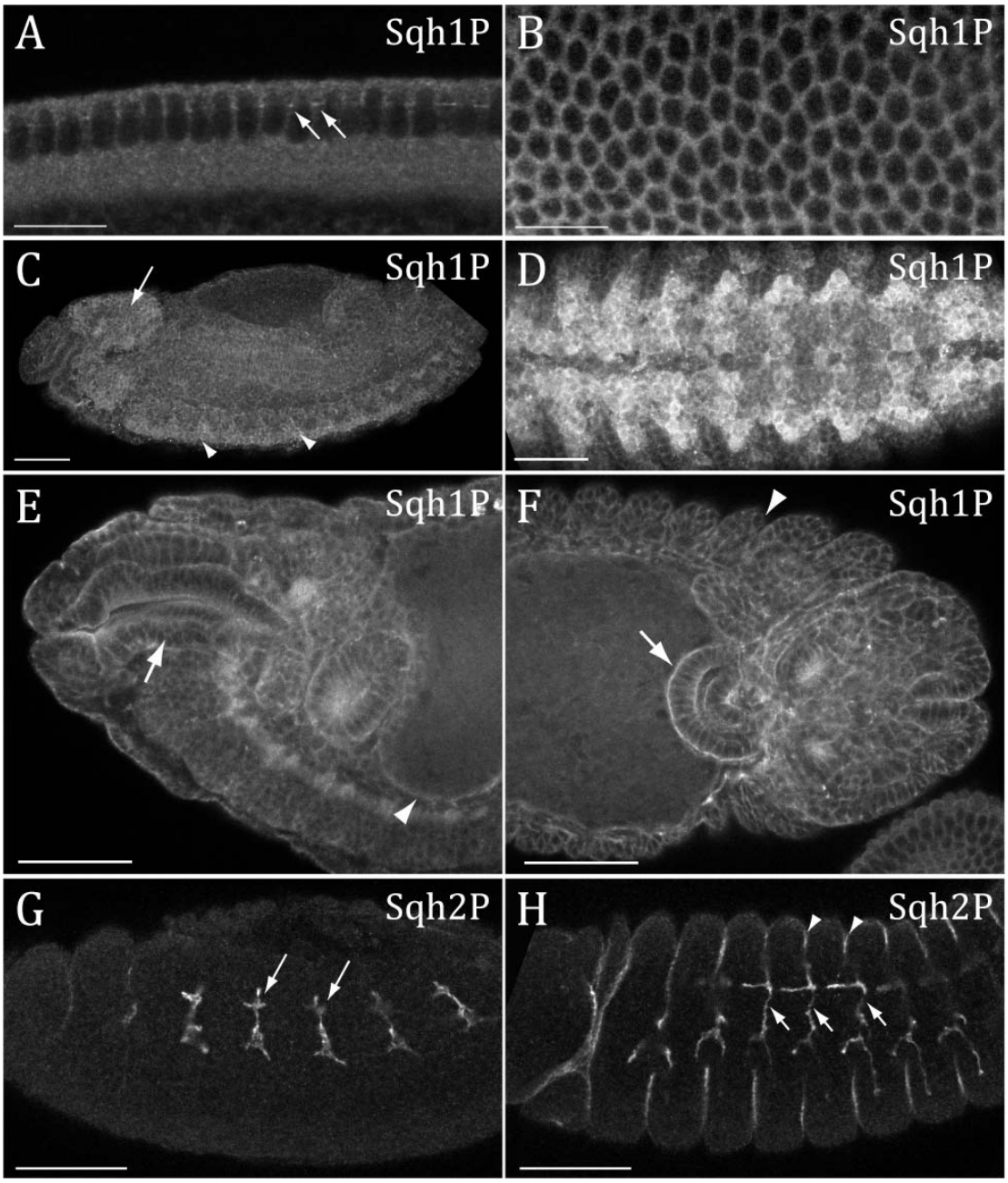
A
Sqh1P
B
Sqh1P
C
Sqh1P
D
Sqh1P
E
Sqh1P
F
Sqh1P
G
Sqh2P
H
Sqh2P

Figure 2.6
Sqh1P and Sqh2P are differently expressed in embryos.
Confocal optical sections of wild type embryos stained with antibodies against Sqh1P (A-F) or Sqh2P (G, H).
(A) A cross section through the middle of a cellularizing embryo shows Sqh1P staining in the cleavage furrows (arrows).
(B) A surface view of the same embryo in (A) reveals cell outlining and indicates that it is ubiquitously expressed at this stage.
(C) Sqh1P is strongly expressed in the brain (arrow) and ventral nerve cord (arrowhead) of a stage 14 embryo.
(D) Ventral view of a stage 14 embryo showing high level of Sqh1P in the nerve cells.
(E) Sqh1P is strongly expressed in the foregut (arrow) and mid gut (arrowhead) of a stage 14 embryo.
(F) Sqh1P is also expressed at high levels in the hindgut (arrow) and epidermis (arrowhead) of a stage 14 embryo. Note that the expression in the hindgut is on both the apical and basal surfaces of these cells.
(G) Sqh2P is strongly expressed in the invaginating tracheal placodes (arrows) in stage 12 embryos.
(H) Sqh2P is expressed throughout the tracheal system (arrows) and in the segmental boundaries (arrowheads) of stage 13 embryos.
(Scale bars = 20μm in A and B, 50μm in C-H)

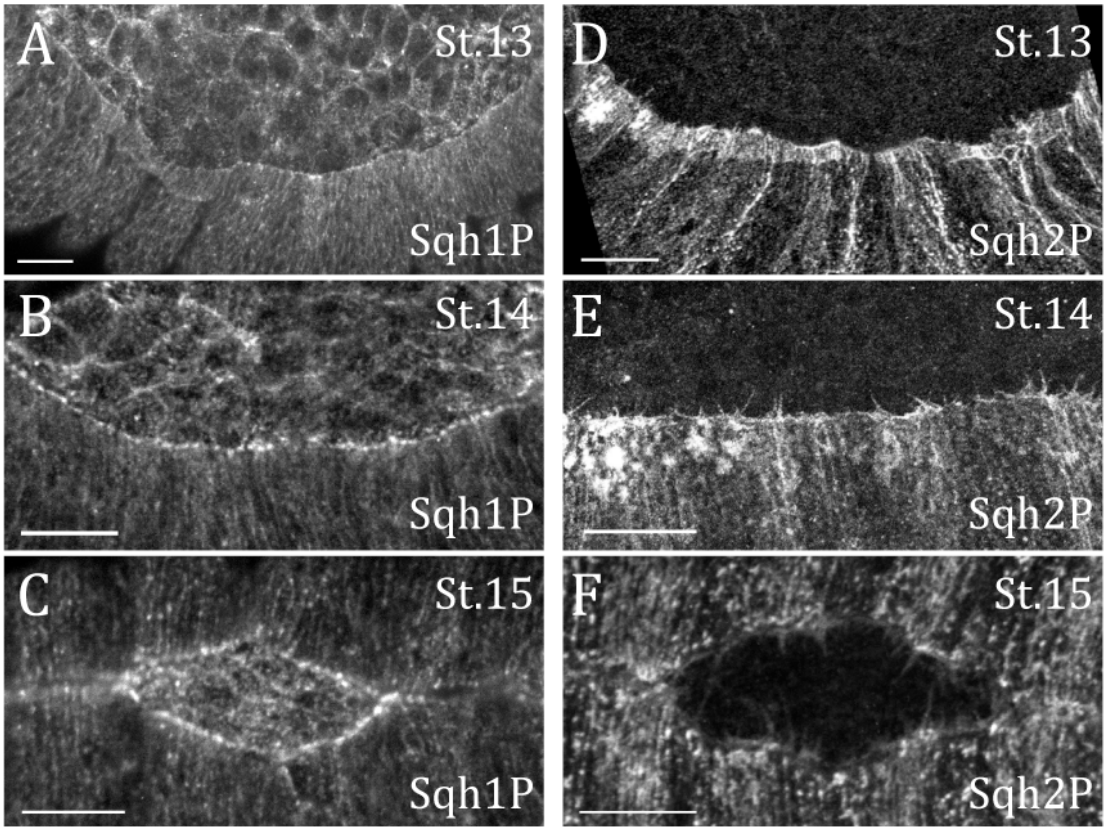

Figure 2.7
Examination of Sqh1P and Sqh2P in DME cells during dorsal closure.
(A-C) Confocal optical sections of stage 13-15 w^{1118} embryos stained with antibodies against Sqh1P. At all stages, Sqh1P is strongly upregulated at the leading edge of the DME cells, and localizes in a "bars-on-a-string" distribution at this leading edge. This distribution of Sqh1P is identical to the pattern observed with antibodies against Sqh and Zip and is consistent with a localization on the actinomyosin cable that has been well described in these cells during dorsal closure.
(D-F) Confocal optical sections of stage 13-15 w^{1118} embryos stained with antibodies against Sqh2P. At stage 13 (D), Sqh2P is strongly upregulated throughout the DME cells. Large aggregates of Sqh2P are often seen in these cells, particularly near the anterior end of the DME cells. Long filopodia filled with Sqh2P become apparent at this stage as well. During stages 14 – 15, Sqh2P is strongly expressed at the leading edge of the DME cells and in filopodial protrusions, although the distribution along the leading edge is continuous and does not correlate with the "bars-on-a-string" distribution seen with Sqh1P. (Scale bars = 20μm)

the leading edge cells (Figure 2.7 D). At stage 14–15, Sqh2P can be detected on the continuous actin cable and dynamic filopodial protrusions (Figure 2.7 E, F).

Examination of phospho-Sqh in response to Rho signaling

I generated *Rho kinase* (*rok*) homozygous mutant clones and examined the expression of Sqh1P and Sqh2P in these clones in white prepual imaginal discs (~72 hours after clone induction). Interestingly, I observed no obvious difference of Sqh1P/Sqh2P expression level or distribution between the *rok* homozygous mutant cells and the wild type background (Figure 2.8). This observation is in contrast to that of Winter et al., who showed that the level of Sqh1P is significantly reduced in *rok* clones in 32-hour pupal wing (~104 hours after clone induction) [32]. It is well recognized that beside Rho kinase, MRLC kinase and Rho-dependent Citron kinase can also phosphorylate MRLC. Ueda et al. showed that only ~30% of MRLC diphosphorylation was induced by Rho kinase in HeLa cell extracts [15]. Therefore, possibly the loss of *rok* function in the mutant imaginal disc cells can be compensated by other kinases at this stage of development, whereas Rho kinase may be the only relevant kinase capable of phosphorylating Sqh in the pupal wings.

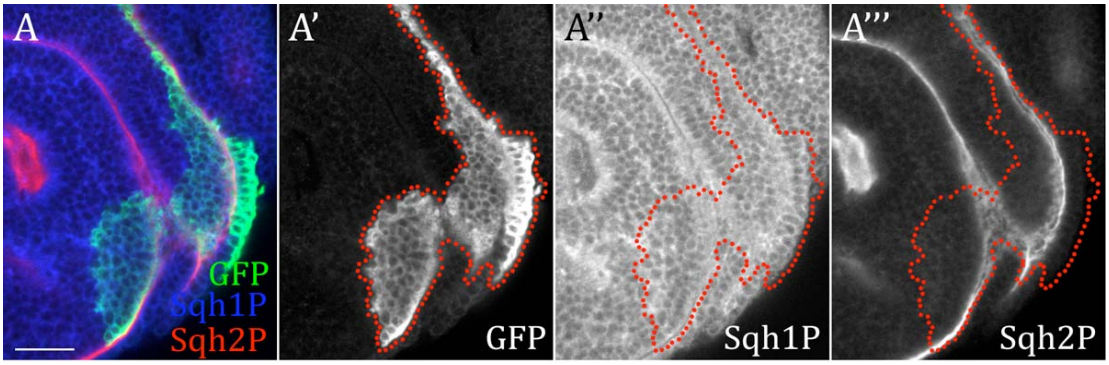

Figure 2.8
The expression pattern of Sqh1P and Sqh2P in *rok* clone
A white prepupal wing disc triple labeled with anti-GFP (green), anti-Sqh1P (blue) and anti-Sqh2P (red) antibodies. Separated channels are shown in A'-A'''. Homozygous *rok* mutant cells are marked by presence of GFP (circled with red dotted line). The level and localization of Sqh1P and Sqh2P do not seem to be different in *rok* mutant cells comparing to the wild type background.
(Scale bar = 20μm)

Discussion

To monitor the activation of nonmuscle myosin II during morphogenesis, we have generated two antibodies against phosphorylated forms of Sqh, one of which recognizes phospho-Serine-21 (Sqh1P) and the other recognizes phospho-Serine-21 and phospho-Threonine-20 (Sqh2P). We demonstrated the specificity of the antibodies on both immunoblots and immunostaining. We observed that Sqh1P and Sqh2P have different expression pattern and subcellular localization in *Drosophila* tissue during development. In imaginal disc cells, Sqh1P predominantly localizes in the adherens junction, whereas Sqh2P concentrates at the apical surface. During embryogenesis, Sqh1P can be detected in nearly all tissues, while Sqh2P can only be detected in a few tissues that are undergoing extensive cell shape change or cell movement. Interestingly, on the actomyosin cable in the leading edge cells during dorsal closure, Sqh1P localizes in a "dotted-line" pattern, whereas Sqh2P is distributed continuously on the cable and is enriched in the filopodial protrusions. In 3rd instar larval and white prepupal imaginal disc, the expression patterns of Sqh1P and Sqh2P in homozygous *Rho kinase* mutant clones are similar to those in wild type background, indicating that Rho kinase is not the relevant kinase for MRLC phosphorylation during these stages of imaginal disc development and that the loss of *Rho kinase* can be compensated by other kinases in larval imaginal discs.

In the future, we will use these antibodies to monitor myosin activation and to identify regulators of myosin activity during development.

Distinct subcellular localization of Sqh1P and Sqh2P in imaginal discs

Previous studies have described different subcellular localizations of monophosphorylated MRLC and diphosphorylated MRLC in cultured vertebrate cells [33, 34]. Here we showed that Sqh1P and Sqh2P also have distinct subcellular localizations in *Drosophila* imaginal discs and embryos. In imaginal disc cells, Sqh1P mainly localizes to the adherens junction, while Sqh2P localizes to the very apical surface of the cells. What could be possible reasons for the different subcellular distribution of Sqh1P and Sqh2P? Sakurada et al. reported that treatment with a protein phosphatase inhibitor, calyculin A, strongly induced diphosphorylation of MRLC in cultured SM-3 smooth muscle cells [34]. Other investigators have observed that the myosin binding subunit of *Drosophila* myosin phosphatase (MYPT) localizes to the adherens junction [35, 36]. Thus, one possible explanation could be that myosin phosphatase in the adherens junction may reduce the level of Sqh2P there. Previous studies also indicated that double phosphorylation of MRLC requires a higher level of myosin regulatory light chain kinase [12, 13]. Therefore, alternatively, it is possible that the kinases that can phosphorylate Sqh mainly localize to the very apical area of the cell since previous studies showed that diphosphorylation of MRLC in

vertebrate cells requires much higher concentration of myosin light chain kinase or Rho kinases than does monophosphorylation of MRLC [12, 13, 15]. Further studies will be done to check if these kinases co-localize with Sqh2P subcellularly. A third possibility could be that diphosphorylation of MRLC and monophosphorylation of MRLC are regulated through different mechanisms, as suggested by Sakurada and his colleagues who observed that diphosphorylation of MRLC is more sensitive to certain protein kinase inhibitors in rabbit aortic smooth muscle cells [34].

What might be the function of Sqh2P at the very apical area of the cells in imaginal discs? Concentrating of Sqh2P may suggest that higher myosin activity is necessary, since diphosphorylation of MRLC result in higher actin-dependent myosin ATPase activity and motor activity of myosin than monophosphorylation of MRLC [11]. Previous studies showed that columnar epithelial cells and the opposing peripodial epithelial cells both send out filopodial protrusions, which might play an important role in signal exchange between the two different types of epithelial cells [37, 38]. Possibly high levels of myosin activity are necessary for vesicle transport in the filopodial protrusions. It would be interesting to examine at high resolution to see if Sqh2P concentrates there.

Distinct distribution of Sqh1P and Sqh2P at the leading edge during dorsal closure in the embryo

Previous studies showed that myosin heavy chain (Zip) localizes in a "bars-on-a-string" distribution in the leading edge cells of the lateral epidermis during dorsal closure [4, 31], whereas F-actin forms a continuous cable in the leading edge and dynamic filopodial structures emanating from the cells towards the dorsal midline [31, 39-41]. Interestingly, we observed that Sqh1P and Sqh2P have distinct localization at the leading edge. Sqh1P localizes in a similar pattern as Zip during all stages of dorsal closure, whereas Sqh2P is first upregulated in the leading edge cells at the initiation phase of dorsal closure and is enriched in the actin-rich filopodial protrusions at later stages. Localization of Sqh1P on the actin cable should be essential for generation of the contractile force, which contributes to maintenance of a uniform migrating front and closure of the dorsal hole [39, 42]. Upregulation of Sqh2P in the leading edge cells during initial phase of dorsal closure indicate that possibly high level of myosin activity is necessary for transition of the leading edge cells from stationary to migratory. What might be the function of Sqh2P in the filopodia? Jacinto et al. reported that these filopodial protrusions are remarkably dynamic and may play an important role in scanning opposing epithelial cells and dragging the cell sheets of both sides together [41]. Tokuo et al. showed that myosin X is crucial for actin reorganization leading to formation of filopodia in African green monkey kidney COS7 cells and NIH3T3 fibroblasts [43]. Myosin X also plays an important role in formation and elongation of filopodia [44, 45]. There is no homolog of myosin X in *Drosophila*. The function of myosin X might be carried out by other myosins.

Therefore, possibly myosin II is required for formation and elongation of filopodial protrusions at the leading edge during dorsal closure. And possibly higher level of myosin II activation is required in these processes.

Reference

1. Conti, M.A., and Adelstein, R.S. (2008). Nonmuscle myosin II moves in new directions. Journal of cell science *121*, 11-18.
2. Bosgraaf, L., and van Haastert, P.J. (2006). The regulation of myosin II in Dictyostelium. European journal of cell biology *85*, 969-979.
3. Zhao, D.B., Cote, S., Jahnig, F., Haller, J., and Jackle, H. (1988). Zipper encodes a putative integral membrane protein required for normal axon patterning during Drosophila neurogenesis. The EMBO journal *7*, 1115-1119.
4. Young, P.E., Richman, A.M., Ketchum, A.S., and Kiehart, D.P. (1993). Morphogenesis in Drosophila requires nonmuscle myosin heavy chain function. Genes & development *7*, 29-41.
5. Gotwals, P.J., and Fristrom, J.W. (1991). Three neighboring genes interact with the Broad-Complex and the Stubble-stubbloid locus to affect imaginal disc morphogenesis in Drosophila. Genetics *127*, 747-759.
6. Halsell, S.R., and Kiehart, D.P. (1998). Second-site noncomplementation identifies genomic regions required for Drosophila nonmuscle myosin function during morphogenesis. Genetics *148*, 1845-1863.
7. Karess, R.E., Chang, X.J., Edwards, K.A., Kulkarni, S., Aguilera, I., and Kiehart, D.P. (1991). The regulatory light chain of nonmuscle myosin is encoded by spaghetti-squash, a gene required for cytokinesis in Drosophila. Cell *65*, 1177-1189.
8. Edwards, K.A., and Kiehart, D.P. (1996). Drosophila nonmuscle myosin II has multiple essential roles in imaginal disc and egg chamber morphogenesis. Development (Cambridge, England) *122*, 1499-1511.
9. Korn, E.D., and Hammer, J.A., 3rd (1988). Myosins of nonmuscle cells. Annual review of biophysics and biophysical chemistry *17*, 23-45.
10. Tan, J.L., Ravid, S., and Spudich, J.A. (1992). Control of nonmuscle myosins by phosphorylation. Annual review of biochemistry *61*, 721-759.
11. Ikebe, M., Koretz, J., and Hartshorne, D.J. (1988). Effects of phosphorylation of light chain residues threonine 18 and serine 19 on the properties and conformation of smooth muscle myosin. The Journal of biological chemistry *263*, 6432-6437.
12. Ikebe, M., and Hartshorne, D.J. (1985). Phosphorylation of smooth muscle myosin at two distinct sites by myosin light chain kinase. The Journal of biological chemistry *260*, 10027-10031.
13. Ikebe, M., Hartshorne, D.J., and Elzinga, M. (1986). Identification, phosphorylation, and dephosphorylation of a second site for myosin light chain kinase on the 20,000-dalton light chain of smooth muscle myosin. The Journal of biological chemistry *261*, 36-39.

14. Lee, J.H., Koh, H., Kim, M., Kim, Y., Lee, S.Y., Karess, R.E., Lee, S.H., Shong, M., Kim, J.M., Kim, J., et al. (2007). Energy-dependent regulation of cell structure by AMP-activated protein kinase. Nature *447*, 1017-1020.
15. Ueda, K., Murata-Hori, M., Tatsuka, M., and Hosoya, H. (2002). Rho-kinase contributes to diphosphorylation of myosin II regulatory light chain in nonmuscle cells. Oncogene *21*, 5852-5860.
16. Kosako, H., Yoshida, T., Matsumura, F., Ishizaki, T., Narumiya, S., and Inagaki, M. (2000). Rho-kinase/ROCK is involved in cytokinesis through the phosphorylation of myosin light chain and not ezrin/radixin/moesin proteins at the cleavage furrow. Oncogene *19*, 6059-6064.
17. Yamashiro, S., Totsukawa, G., Yamakita, Y., Sasaki, Y., Madaule, P., Ishizaki, T., Narumiya, S., and Matsumura, F. (2003). Citron kinase, a Rho-dependent kinase, induces di-phosphorylation of regulatory light chain of myosin II. Molecular biology of the cell *14*, 1745-1756.
18. Vicente-Manzanares, M., Ma, X., Adelstein, R.S., and Horwitz, A.R. (2009). Non-muscle myosin II takes centre stage in cell adhesion and migration. Nature reviews *10*, 778-790.
19. Hartshorne, D.J. (1998). Myosin phosphatase: subunits and interactions. Acta physiologica Scandinavica *164*, 483-493.
20. Vereshchagina, N., Bennett, D., Szoor, B., Kirchner, J., Gross, S., Vissi, E., White-Cooper, H., and Alphey, L. (2004). The essential role of PP1beta in Drosophila is to regulate nonmuscle myosin. Molecular biology of the cell *15*, 4395-4405.
21. Jordan, P., and Karess, R. (1997). Myosin light chain-activating phosphorylation sites are required for oogenesis in Drosophila. The Journal of cell biology *139*, 1805-1819.
22. Ward, R.E., Evans, J., and Thummel, C.S. (2003). Genetic modifier screens in Drosophila demonstrate a role for Rho1 signaling in ecdysone-triggered imaginal disc morphogenesis. Genetics *165*, 1397-1415.
23. Patch, K., Stewart, S.R., Welch, A., and Ward, R.E. (2009). A Second-Site Noncomplementation Screen for Modifiers of Rho1 Signaling during Imaginal Disc Morphogenesis in Drosophila. PLoS ONE *4*, e7574.
24. Laemmli, U.K. (1970). Cleavage of structural proteins during the assembly of the head of bacteriophage T4. Nature *227*, 680-685.
25. Seto, M., Sasaki, Y., and Sasaki, Y. (1990). Alteration in the myosin phosphorylation pattern of smooth muscle by phorbol ester. The American journal of physiology *259*, C769-774.
26. Fehon, R.G., Dawson, I.A., and Artavanis-Tsakonas, S. (1994). A Drosophila homologue of membrane-skeleton protein 4.1 is associated with septate junctions and is encoded by the coracle gene. Development (Cambridge, England) *120*, 545-557.

27. Xu, T., and Rubin, G.M. (1993). Analysis of genetic mosaics in developing and adult Drosophila tissues. Development (Cambridge, England) *117*, 1223-1237.
28. Perrie, W.T., and Perry, S.V. (1970). An electrophoretic study of the low-molecular-weight components of myosin. The Biochemical journal *119*, 31-38.
29. Tepass, U., Tanentzapf, G., Ward, R., and Fehon, R. (2001). Epithelial cell polarity and cell junctions in Drosophila. Annual review of genetics *35*, 747-784.
30. Young, P.E., Pesacreta, T.C., and Kiehart, D.P. (1991). Dynamic changes in the distribution of cytoplasmic myosin during Drosophila embryogenesis. Development (Cambridge, England) *111*, 1-14.
31. Franke, J.D., Montague, R.A., and Kiehart, D.P. (2005). Nonmuscle myosin II generates forces that transmit tension and drive contraction in multiple tissues during dorsal closure. Curr Biol *15*, 2208-2221.
32. Winter, C.G., Wang, B., Ballew, A., Royou, A., Karess, R., Axelrod, J.D., and Luo, L. (2001). Drosophila Rho-associated kinase (Drok) links Frizzled-mediated planar cell polarity signaling to the actin cytoskeleton. Cell *105*, 81-91.
33. Uchimura, T., Fumoto, K., Yamamoto, Y., Ueda, K., and Hosoya, H. (2002). Spatial Localization of Mono-and Diphosphorylated Myosin II Regulatory Light Chain at the Leading Edge of Motile HeLa Cells. Cell Structure and Function *27*, 479-486.
34. Sakurada, K., Seto, M., and Sasaki, Y. (1998). Dynamics of myosin light chain phosphorylation at Ser19 and Thr18/Ser19 in smooth muscle cells in culture. The American journal of physiology *274*, C1563-1572.
35. Inagaki, N., Nishizawa, M., Ito, M., Fujioka, M., Nakano, T., Tsujino, S., Matsuzawa, K., Kimura, K., Kaibuchi, K., and Inagaki, M. (1997). Myosin binding subunit of smooth muscle myosin phosphatase at the cell-cell adhesion sites in MDCK cells. Biochemical and biophysical research communications *230*, 552-556.
36. Mitonaka, T., Muramatsu, Y., Sugiyama, S., Mizuno, T., and Nishida, Y. (2007). Essential roles of myosin phosphatase in the maintenance of epithelial cell integrity of Drosophila imaginal disc cells. Developmental biology *309*, 78-86.
37. Demontis, F., and Dahmann, C. (2007). Apical and lateral cell protrusions interconnect epithelial cells in live Drosophila wing imaginal discs. Dev Dyn *236*, 3408-3418.
38. Gibson, M.C., and Schubiger, G. (2000). Peripodial cells regulate proliferation and patterning of Drosophila imaginal discs. Cell *103*, 343-350.

39. Jacinto, A., Wood, W., Woolner, S., Hiley, C., Turner, L., Wilson, C., Martinez-Arias, A., and Martin, P. (2002). Dynamic analysis of actin cable function during Drosophila dorsal closure. Curr Biol *12*, 1245-1250.
40. Jacinto, A., Woolner, S., and Martin, P. (2002). Dynamic analysis of dorsal closure in Drosophila: from genetics to cell biology. Developmental cell *3*, 9-19.
41. Jacinto, A., Wood, W., Balayo, T., Turmaine, M., Martinez-Arias, A., and Martin, P. (2000). Dynamic actin-based epithelial adhesion and cell matching during Drosophila dorsal closure. Curr Biol *10*, 1420-1426.
42. Kiehart, D.P., Galbraith, C.G., Edwards, K.A., Rickoll, W.L., and Montague, R.A. (2000). Multiple forces contribute to cell sheet morphogenesis for dorsal closure in Drosophila. The Journal of cell biology *149*, 471-490.
43. Tokuo, H., Mabuchi, K., and Ikebe, M. (2007). The motor activity of myosin-X promotes actin fiber convergence at the cell periphery to initiate filopodia formation. The Journal of cell biology *179*, 229-238.
44. Berg, J.S., and Cheney, R.E. (2002). Myosin-X is an unconventional myosin that undergoes intrafilopodial motility. Nature cell biology *4*, 246-250.
45. Tokuo, H., and Ikebe, M. (2004). Myosin X transports Mena/VASP to the tip of filopodia. Biochemical and biophysical research communications *319*, 214-220.

Chapter 3

Cloning and characterization of *uninflatable* (*uif*), a novel gene required for embryonic tracheal inflation, and larval tracheal growth and molting

Introduction

Over the past decade genetic and cell biological approaches have provided extensive knowledge regarding the mechanisms involved in the patterning of the *Drosophila* tracheal metameres and how adjacent metameres fuse to form a complete tracheal system (reviewed in [1, 2]). In recent years the mechanisms required for final maturation of the tracheal tubes have started to come into focus. Tracheal maturation is a multistep process necessary to produce tracheal tubes of appropriate length and diameter to effectively deliver air to the peripheral tissues while sustaining an inflated state. Steps in this process include the secretion of chitinous extracellular matrix into the lumen of the newly formed tracheal system, and the eventual clearance of lumenal protein to leave liquid filled tracheal tubes (Figure 3.1). The first step in this process requires a chitin synthase encoded by the gene *krotzkopf verkehrt* (*kkv*) and an UDP-*N*-acetylglucosamine diphosphorylase encoded by the *mummy* (*mmy*) gene to produce a chitinous matrix in the lumen of stage 14 embryos [3-5]. This early phase of tube maturation also requires the small GTPase encoded by *sar1* that

tube maturation processes **essential genes (function)**

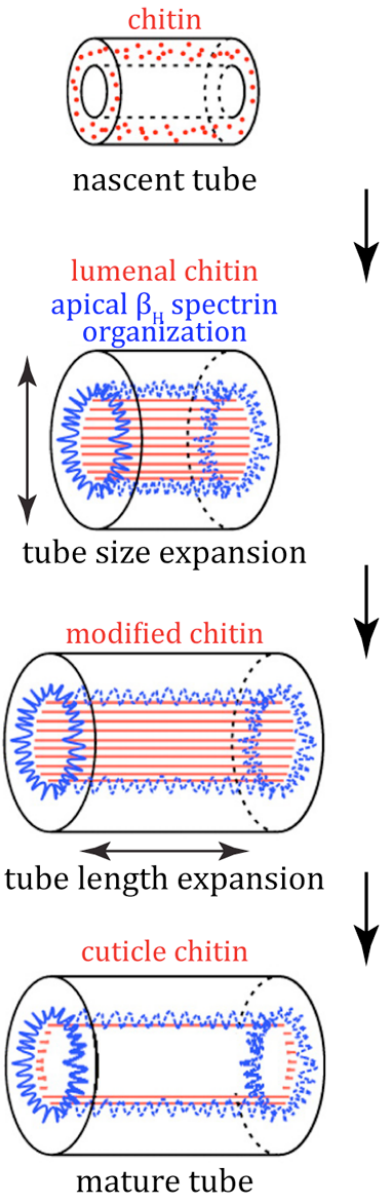

kkv (chitin synthase)
mmy (UPD-N-acetylglucosaminee diphosphorylase)

sar1, *sec13*, *sec23*, etc. (secretion)

serp, *verm* (chitin modification)
septate junction components (proper secretion of Serp and Verm into tracheal lumen)

rab5, *chc*, *shi*, *wurst,* etc. (endocytosis)

daam (taenidial organization)
ppk (liquid removal)

Figure 3.1
Schematic drawing of *Drosophila* tracheal tube maturation
Tracheal epithelial cells synthesize and secrete chitin into the lumen of the nascent tube. This luminal chitinous matrix is required for expansion of tube diameter and length, and also for normal organization of the apical β_H spectrin cytoskeleton. Subsequently, the luminal chitin is modified and endocytosed, leaving behind a liquid filled tubular system of proper size and length. Shortly before larval hatching, the luminal liquid is quickly replaced by gas. Essential genes and their functions during each step of tube maturation are listed on the right. (This figure is adapted from Swanson and Beitel 2006 [6]).

regulates vesicle traffic from the endoplasmic reticulum to the Golgi apparatus [7], and thereby controls the secretion of key matrix proteins. Together these proteins regulate the dilation of the tracheal lumen to adopt the appropriate diameter. Subsequently, the secretion of a pair of putative chitin deacetylase enzymes encoded by *serpentine* (*serp*) and *vermiform* (*verm*) regulates the size of the apical surface of the tracheal cells, and thereby controls tracheal length, through an unknown mechanism [8, 9]. Interestingly, mutations in genes encoding components of the septate junction, a lateral membrane domain analogous to the vertebrate tight junction in its paracellular barrier function, also result in tracheal length defects, likely through a requirement for intact septate junctions in the proper secretion of Serp and Verm (and possibly other proteins) into the tracheal lumen [29-34]. Later, during stage 17 of embryogenesis, the modified chitin and other luminal proteins are cleared through a process that requires clathrin-mediated endocytosis, rab5, and a transmembrane protein encoded by *wurst* that appears to regulate tracheal endocytosis through its cytoplasmic clathrin binding motifs and a J-domain that binds to the chaperone Hsc70-4 [7, 10].

The final stages of tracheal maturation including the organization of the tracheal cuticle and subsequent air filling are less well understood. When the chitinous material is being secreted into the tracheal lumen in preparation for tube dilation, the tracheal cells also begin to secrete proteins into the apical extracellular matrix that eventually assembles into a characteristic cuticle

containing densely packed parallel rows of cuticular ridges called taenidia. This cuticle provides an important barrier to dehydration and infection while the taenidial organization provides mechanical stability to the tubes. This mechanical role of the taenidia is best demonstrated by mutations in the formin homology gene *daam*. *daam* encodes an actin polymerizing protein, and mutations in *daam* affect a subapical actin cytoskeleton that forms circumferential rings in register with the taenidial ridges. *daam* mutations result in disorganized taenidia and collapsed tracheal tubes [11]. Finally the tracheal lumen is cleared of fluid and inflated with air via a mechanism that is still unclear, yet likely requires the action of epithelial sodium channels [12].

During larval stages, the tracheal system continues to grow to meet the oxygen needs of the developing larva. Beitel and Krasnow [13] observed that tracheal length increases gradually throughout larval development, whereas tracheal diameter increases in a saltatory fashion coupled to the tracheal molts. Since there is no cell proliferation in the larval trachea, these changes result from growth of the tracheal cells that somehow must be coupled to the growth of the larva. The mechanisms involved in this process have yet to be elucidated, as all of the tube size control genes that have been characterized affect embryonic development rather than larval tracheal growth.

In this report, we describe the cloning and initial characterization of *uninflatable* (*uif*), a novel gene that encodes an apically localized transmembrane protein expressed at high levels in the developing tracheal system. The large

extracellular domain of Uif contains several different carbohydrate binding domains and epidermal growth factor repeats, whereas the short cytoplasmic domain is devoid of conserved domains. Uif is highly conserved in insect species. Zygotic loss of *uif* results in defects in tracheal inflation during late embryogenesis without obviously affecting tracheal patterning or maturation prior to air filling. In addition, *uif* mutant larvae display a tracheal growth defect and fail to effectively molt their tracheal cuticle. RNAi-induced knockdown of *uif* in the imaginal discs produces *Notch* loss-of-function phenotypes in corresponding adult tissues.

Part of this chapter is adapted from a published manuscript by Zhang and Ward, 2009 [14].

Materials and methods

Drosophila strains

The *uif*^{1} allele is an EMS induced second-site mutation on the *E(br)155* chromosome reported in [15]. *uif*^{2B7} and *uif*^{1A15} were isolated in an F_2 EMS mutagenesis screen described below. *UAS-CG9138RNAi* strains (v1047 and v1050; hereafter referred to as *UAS-uifRNAi*) were obtained from the Vienna *Drosophila* RNAi Center (VDRC, Vienna, Austria; [16]. *Df(2L)Exel7029*, *breathless* (*btl*)-*Gal4*, *daughterless* (*da*)-*Gal4*, *engrailed* (*en*)-*Gal4*, *distalless* (*dll*)-*Gal4*, *apterous* (*ap*)-*Gal4*, *yw ; Bl L / CyO, P{w*$^{+}$*, hs-hid}* and *w*^{1118} were obtained from the Bloomington *Drosophila* Stock Center (Bloomington, IN). *w*^{1118} was used as the wild type strain for the experiments reported here. *uif*^{1}, *uif*^{2B7}, and *uif*^{1A15} were balanced with *CyO, P{w*$^{+}$*, Dfd-EYFP}* [17]. All *Drosophila* stocks were maintained on media consisting of corn meal, sugar, yeast, and agar in incubators maintained at a constant temperature of 21°C or in a room that typically fluctuated between 21°C and 22.5°C. Genetic experiments were conducted in incubators controlled at a constant temperature of 25ºC.

EMS Mutagenesis and screening

Two cohorts of approximately thirty 3-5 day old w^{1118} males were treated with 25 mM methanesulfonic acid ethyl ester (EMS) in empty plastic vials for approximately 16 hours. Each cohort was mated to approximately thirty *yw ; Bl L / Cyo, P{w+, hs-hid}* virgin females in bottles maintained at 21°C. The adults were transferred to fresh bottles after 3 days and subsequently transferred once more after an additional 2 days. Single balanced male progeny (*yw / Y ; * / Cyo, P{w+, hs-hid}*) were crossed to 5-6 *w ; uif*^{1} */ Cyo, P{w+, Act-GFP}* virgin females in narrow short vials. All single male cross vials were heat shocked in a 37°C water bath for one hour on days 5 and 6 after setting the cross to eliminate any flies bearing the *hs-hid* balancer chromosome. We established balanced stocks by sibling mating of all the vials that produced only * / *Cyo, P{w+, Act-GFP}* offspring. Two of the lines (referred to as 1A15 and 2B7) also failed to complement *Df(2L)Exel7029* (cytological breakpoints 27C4;27D4), suggesting that they were new *uif* alleles. Sequencing of genomic DNA isolated from homozygous mutant late embryos (by the DNA Facility of the Iowa State University Office of Biotechnology in Ames, IA) confirmed this notion. PCR primers are listed in supplemental table 3.1. All exonic sequences and intron/exon boundaries were sequenced on one strand of the genomic DNA. Regions containing putative mutations were verified by sequencing both strands. Specifically, both strands representing nucleotides 27207-28780 of GenBank sequence **AAC008326** were sequenced for *uif*^{1}, as were nucleotides 29856-31290 for *uif*^{2B7} and *uif*^{1A15}.

Genomic organization determination

Total RNA was collected from 12-24 hour w^{1118} embryos and late third instar larval wing imaginal discs. cDNAs were generated using SuperScript III reverse transcriptase (Invitrogen, Carlsbad, CA). DNA primers corresponding to sequences spanning predicted exon/intron boundaries were used for PCR, and the resulting products were examined for predicted sizes by gel electrophoresis. Three independent primer sets spanning exon 10 and 11 produced double bands differing by ~100 bp in both the embryonic and imaginal disc cDNA collections. These DNA fragments were recovered and sequenced at the Iowa State University DNA facility.

Phylogenetic analyses

The cytoplasmic domain of Uif (NH2-WMICVRSTKRRDPKKMLTPAIDQTGSQVNFYYGAHTPYAESIAPSHHSTYAHYYDDEEDGWEMPNFYNETYMKDGLHGGKMSTLARSNASLYGTKEDLYDRLKRHAYTGKKEKSDSDSEVQ-COOH) was BLASTed against the nonredundant protein sequence database and the following 19 sequences were identified as showing significant sequence similarity to Uif throughout the entire protein sequence: XP_002067066.1, AAF63500.1, XP_001357402.2, XP_002088091.1, XP_001988186.1, XP_001970107.1, XP_001961405.1, XP_002002737.1,

XP_002078458.1, XP_002018755.1, XP_002051404.1, XP_001861365.1, XP_001606223.1, XP_001658862.1, XP_974965.2, EEB13939.1, XP_396277.3, XP_001949468.1, XP_312182.4. Notably, the cytoplasmic domain of Uif was not found outside the insect order, and all sequences showing similarity to the cytoplasmic domain contained a full-length Uif protein. These sequences were then aligned using MUSCLE (Multiple sequence comparison by log-expectation; [18]. For simplicity sake in drawing the tree shown in Fig. 1B, we eliminated *D. virilis*, *D. persimilis*, *D. similans*, and *D. erecta*, which all mapped within the *Drosophila* subgroup. A pairwise comparison between *D. melanogaster* and *Acythosiphon pisum* was conducted using BLAST2seq on the NCBI server.

Lethal phase and phenotypic analyses

Prior to conducting lethal phase and terminal phenotypic analyses on *uif* mutants, we cleaned the uif^{1A15} and uif^{2B7} mutant chromosomes by sequentially recombining *P-* or *PiggyBac* elements onto and off of the *uif* chromosomes. For the centromere proximal side we used $P\{XP\}CG6739^{d09967}$ (in 28B4), and for the centromere distal side we used $PBac[PB]stai^{c01639}$ (in 26B7). Since we were unable to recombine uif^{1} apart from the *E(br)155* mutation, we have not included this allele in the analyses described here. uif^{1A15}, uif^{2B7}, and *Df(2L)Exel7029* were balanced with $CyO, P\{w^{+}, Dfd\text{-}EYFP\}$ such that mutant embryos and larvae could be unambiguously identified by the absence of YFP.

Embryonic staging was determined by gut morphology. RNAi experiments were performed by crossing *UAS-uifRNAi* strains (v1047 and v1050) to *btl-Gal4* or *da-Gal4* strains. It should be noted that *btl-Gal4, UAS-GFP* homozygous embryos showed greater than 40% tracheal inflation defects, but when outcrossed to w^{1118}, the *btl-Gal4, UAS-GFP/+* embryos showed no tracheal inflation defects. Embryonic lethality was determined as the percentage of unhatched embryos 48 hours after selecting non-YFP-expressing mutant embryos produced through a four-hour egg collection. Larval lethality was determined as the percentage of non-pupariating mutant larvae seven days after selecting newly hatched mutant larvae. All experiments were performed in triplicate and means with standard deviations were determined. Non-hatched embryos were dechorionated in 6% sodium hypochloride, mounted on microscope slides in Hoyer's medium and subsequently examined for cuticular phenotypes on a Nikon Eclipse 80*i* compound microscope. Similarly, mutant larvae from parallel experiments were examined for defects on Zeiss SV6 or Leica MZ7.5 stereomicroscopes and mounted in Halocarbon oil 700 (Sigma, St. Louis, MO). The non-molted larva shown in Fig. 5E was mounted in Hoyer's medium. Wild type and *uif* mutant larval tracheae were hand-dissected from appropriately staged animals in PBS and mounted in 90% glycerol, 100 mM Tris, pH 8.0. Larval staging was determined by anterior spiracle morphology, although mouthpart morphology was additionally used to confirm the stage of five-day-old uif^{2B7} second instar larvae. All cuticular phenotypes were documented on a Nikon Eclipse 80*i*

compound microscope equipped with a Photometrics CoolSNAP *ES* high performance digital CCD camera. Photomicrographs were adjusted for brightness and contrast with the Adobe Photoshop (version CS3, San Jose, CA), and figures were compiled in Adobe Illustrator (version CS3, San Jose, CA).

Time-lapse movies were generated by mounting stage 17 uif^{2B7} mutant embryos on apple juice plates, and automatically collecting brightfield images every minute for 230 minutes using MetaMorph (Molecular Devices, Sunnyvale, CA) software on a Nikon Eclipse 80*i* compound microscope equipped with a Photometrics CoolSNAP *ES* high performance digital CCD camera using a 4X Nikon Plan Apo lens. The image stack was opened in ImageJ [19] and saved as image sequences that were then changed to 8-bit images and adjusted for brightness and contrast in Adobe Photoshop. These adjusted images were then opened in ImageJ, cropped and saved as an AVI file with a rate of 4 frames per second. We subsequently cropped the image sequence files to visualize one embryo using ImageJ, and selected individual frames that were compiled in Adobe Illustrator to make Fig. 3.

To quantify the tracheal length defects in *uif* mutant third instar larvae, we collected newly hatched w^{1118}, uif^{2B7}, uif^{1A15}, and *btl-Gal4/UAS-uifRNAi* larvae and grew them on separate apple juice plates at 25ºC until they were either second or third instar larvae (as judged by anterior spiracles). Individual live larvae were then mounted in halocarbon oil on microscope slides with cover slips. After approximately 5 minutes, brightfield photomicrographs were taken

on a Nikon Eclipse 80*i* compound microscope equipped with a Photometrics CoolSNAP *ES* high performance digital CCD camera using a 4X Nikon Plan Apo lens. Individual images were opened in MetaMorph and lines were drawn using multi-line to record the total body length or tracheal length. Pixel lengths were then obtained from the MetaMorph software using the region measurements tool. For tracheal length, we measured the distance along the dorsal trunk from the posterior spiracles to the transverse connective that originated in abdominal segment 4 during embryogenesis. It should be noted that in the *uif* mutant larvae, this TC was always physically located in more posterior segments, whereas this TC was almost always found in A4 in the w^{1118} larvae. For each larva, we determined the ratio of the partial tracheal length to full body length. We then determined the mean with standard deviation for each genotype.

RNA *in situ* hybridization

RNA *in situ* hybridization was performed as described in Choksi et al., (2006). A 646 nucleotide anti-sense probe for *uif* (corresponding to nucleotides 4216 to 4864 of GenBank sequence **AF239608**) was generated using a T7 DIG RNA labeling kit (Roche Applied Science, Indianapolis, IN). The template for anti-sense probe synthesis was generated by PCR amplification from a 12-24 hour embryo cDNA collection using the following primers: 5'-ACTGCGATGTCAATGCCTACTGC-3' and 5'-CAGTAATACGACTCACTATTACTACTG

CACTTCGCTATCACTATCACTC-3' (T7 promoter sequence is underlined). A complementary sense probe was used as a control. The template for sense probe synthesis was generated by PCR amplification from a 12-24 hour embryo cDNA collection using the following primers: 5'-CAGTAATACGACTCACTATTAACTGCGATGTCAATGCCTACTGC-3' and 5'-CTACTGCACTTCGCTATCACTATCACTC-3 (T7 promoter sequence is underlined).

Generation of anti-Uif antibodies

To generate antiserum against Uif, nucleotides 2832 to 3659 of GenBank nucleotide sequence **AF239608** were cloned into a modified pET21a vector. This represents amino acids 2882-3157 of Uif, and its location is depicted in Fig. 1. The protein was overexpressed in *E.Coli* BL21 (DE3) cells, solubilized in binding buffer (20mM Tris-HCl pH8.0 500mM NaCl, 5mM Imidazole) with 6M urea, and purified through Ni^{2+} affinity chromatography. Purified protein was pooled and dialysis against PBS, in which it formed a precipitate. Purified precipitated protein was used for antibody generation in guinea pigs at the Pocono Rabbit Farm and Laboratory Inc. (PRF&L, Canadensis, PA). The guinea pig anti-Uif serum was subsequently affinity purified at PRF&L.

Immunostaining and dye exclusion experiments

Embryos were fixed and processed for antibody staining as described in [20]. For larval expression studies, the larvae were torn in half, turned inside out and fixed at room temperature for 20 minutes in 4% paraformaldehyde in PBS. The following primary antibodies were used at the given dilutions: affinity purified guinea pig anti-Uninflatable 1:20, mouse anti-Crumbs 1:100 (clone Cq4 from the Developmental Studies Hybridoma Bank at the University of Iowa, Iowa City, IA), mouse anti-Armadillo 1:100 (clone N27A1, DSHB), mouse anti-Dlg 1:100 (clone 4F3, DSHB), mouse anti-Fasiclin 3 1:300 (clone 7G10, DSHB), mouse anti-Cut 1:300 (clone 2B10, DSHB), and mouse anti-Coracle 1:400 (gift from Richard Fehon, University of Chicago; [21]. Secondary antibodies were obtained from Jackson ImmunoResearch Laboratories (West Grove, PA) and used at 1:400. Alexa Fluor 555 conjugated wheat germ agglutinin (WGA) was used at a concentration of 1μg/ml (Invitrogen, Carlsbad, CA). Rhodamine conjugated Chitin Binding Probe (CBP) was used at 1:500 according to the manufacturers recommendation (New England Biolabs Inc., Beverly, MA). Congo red staining was performed by incubating fixed embryos (ten minutes in 4% paraformaldehyde at room temperature) with a 1.5 μg/ml solution of Congo Red (Sigma, St. Louis, MO) in PBS plus 0.1% Trition X-100 for four hours at room temperature, followed by three 15 minutes washes of PBS plus Triton X-100. Dye exclusion experiments to test the integrity of the tracheal septate junctions were performed as described in Lamb et al., (1998). Confocal images were acquired on a Zeiss LSM510 Meta Laser Scanning Confocal Microscope (Carl Zeiss Inc,

Thornwood, NY). Photomicrographs were adjusted for brightness and contrast with the Adobe Photoshop, and figures were compiled in Adobe Illustrator.

Results

uif encodes a novel transmembrane protein that is highly conserved in insect species

While mapping an EMS-induced mutation that dominantly enhances a malformed leg phenotype associated with a hypomorphic mutation in the transcription factor *broad* (*E(br)155* [15]), we identified a second-site mutation that failed to complement the molecularly defined deficiency *Df(2L)Exel7029* (cytology 27C4;27D4). Sequence analysis of genomic DNA isolated from *E(br)155* mutant embryos revealed a nonsense mutation in the gene *CG9138* (also known as *SP1070*; CG to TA transition at nucleotide 29974 of GenBank sequence **AC008326** generating a Glu^{2407} to stop mutation; Figure 3.2 A, Supplemental Figure 3.1 A). Based on the defective tracheal inflation phenotype (described in more detail below), we renamed the gene *uninflatable* (*uif*). We recovered two additional alleles of *uif* while conducting an F_2 screen of EMS-induced mutations that failed to complement the *E(br)155* chromosome. Sequence analysis indicated that uif^{1A15} results from a missense mutation changing Val^{1424} into Glu (TA to AT transversion at nucleotide 31022 of GenBank sequence **AC008326**), whereas uif^{2B7} results in a nonsense mutation (Gln^{1741} to stop; CG to TA transition at nucleotide 28856 of GenBank sequence **AC008326**; Figure 3.2 A, Supplemental Figure 3.1 A).

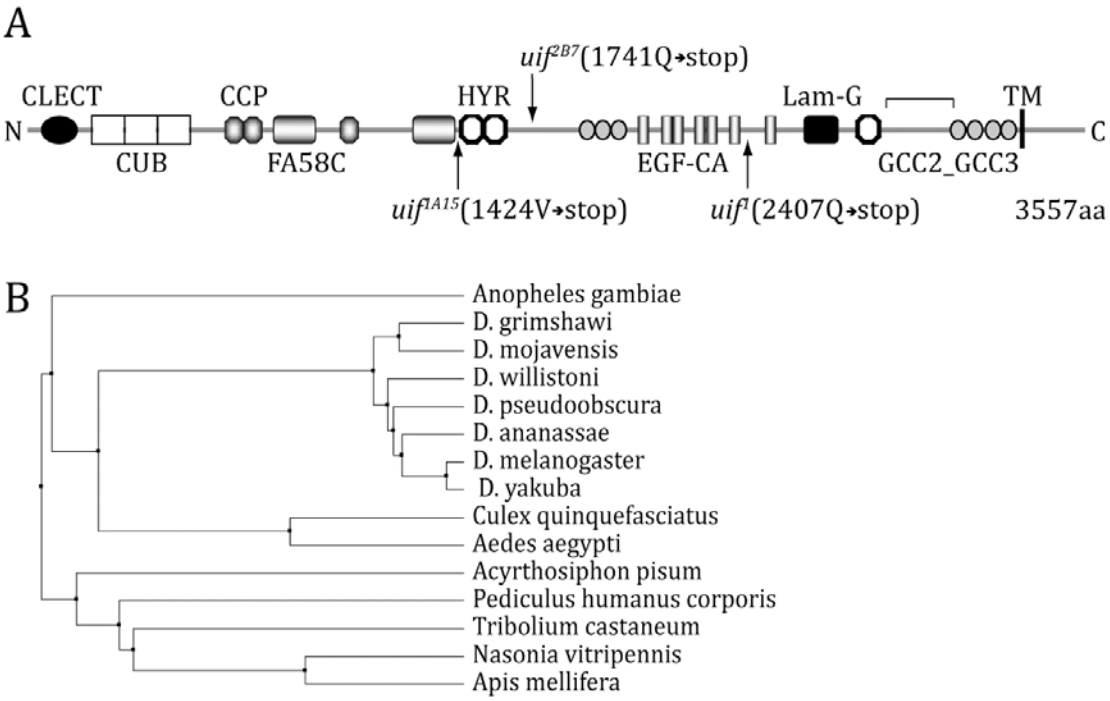

Figure 3.2
Molecular organization and conservation of Uif
(A) Predicted domain organization of Uif protein. A signal sequence is predicted at the N terminus and a single transmembrane (TM) domain is predicted near the C terminus. Molecular details of the mutant alleles are indicated. *uif*^{1} and *uif*^{2B7} result from premature stop codons, whereas *uif*^{1A15} results from a missense mutation changing Val^{1424} into Glu. CLECT, C-type lectin-like domain; CUB, complement C1r/C1s, Uegf, Bmp1 domain; CCP, complement control protein domain; FA58C, coagulation factor 5/8 C-terminal domain; HYR, hyaline repeat domain; EGF-CA, calcium binding Epidermal Growth Factor-like domain; Lam-G, laminin G domain. The region of Uif used for antibody generation is indicated by the bracket above the model.
(B) Phylogenetic tree of Uif orthologs based upon full-length protein sequences. The sequence divergence of Uif correlates precisely with the evolutionary relationships found within the insect order, and no Uif homologs could be identified outside this order.

The predicted Uif protein contains 3557 amino acids with a molecular mass of ~380 KD (Figure 3.2 A). Uif possesses a signal sequence at the amino terminus and contains a single transmembrane domain from amino acids 3415-3437 (based on TMHMM; [22]), generating a Type I transmembrane protein. The large extracellular domain contains one C-type lectin-like (CLECT) domain (a domain known to function in carbohydrate binding), three CUB domains (a structural motif of unknown function often found in extracellular or plasma membrane proteins with developmental roles), three complement control protein (CCP) domains (likely protein interaction domains found in a number of complement proteins and adhesion molecules), and one coagulation factor 5/8 C-terminal (FA58C) domain (another putative carbohydrate binding domain). In addition, the extracellular domain contains three hyaline repeat (HYR) domains (an immunoglobulin fold domain likely involved in cell adhesion), seven GCC2_GCC3 domains (cysteine-rich domains of unknown function), seven calcium binding EGF-like domains (protein interaction domains often involved in cell signaling), and one laminin-G domain (a domain found in a number of proteins involved in cell adhesion and signaling) (Figure 3.2 A). The transmembrane domain contains a GxxxG transmembrane helix dimerization domain [23], suggesting that Uif might exist as a dimer or in higher order protein complexes at the membrane.

Uif is highly conserved in insect species, but does not appear to have a true ortholog in vertebrate species. Through BLAST searching we found a single Uif protein in each of the insect species shown in Figure 3.2 B. The domain

organization and relative positions of the conserved extracellular domains are identical in all of these species. The Uif proteins found in *Drosophila melanogaster* and *Acyrthosiphon pisum* (Pea Aphid), which last shared a common ancestor ~350 million years ago [24], are 69% identical with 82% similarity and only 1% gaps. The cytoplasmic domain, which is devoid of any conserved domains, share >80% sequence identity in all the insect species shown in Fig. 1B, but cannot be identified by homology searches outside of the insect class.

uif mutant larvae have partially inflated trachea

Genetic evidence suggests that uif^{2B7} is an amorphic allele, consistent with the sequence analysis showing a premature stop codon in the extracellular domain. Specifically, uif^{2B7} shows an identical level of embryonic lethality to $uif^{2B7}/Df(2L)Exel7029$ (~15%), and all the animals that hatch in both genotypes die as larvae (Table 3.1). Cuticle preparations of the dead embryos in both genotypes showed mostly normal cuticular structures. Specifically greater than 90% of $uif^{2B7}/Df(2L)Exel7029$ dead embryos showed no obvious patterning defects nor defects in morphogenesis including germ band retraction, dorsal closure or head involution, with the remaining embryos showing mild defects in head involution (n=27 mutant embryos; data not shown). Similarly, 83% of uif^{2B7} dead embryos showed no obvious defects with the remaining 17% showing head involution or mild head skeleton defects (n=41 mutant embryos; data not

Table 3.1
Lethal-phase analysis of *uif* mutant animals

Genotype	%Embryonic lethality[a] (*n*)[b]	%Larval lethality[a] (*n*)[b]
uif^{2B7}/uif^{2B7}	16 ± 1 (218)	100 (183)
uif^{1A15}/uif^{1A15}	3 ± 1 (180)	92 ± 3 (175)
uif^{1A15}/uif^{2B7}	10 ± 2 (228)	100 (204)
uif^{2B7}/Df(2L)Exel7029	15 ± 5 (140)	100 (177)
uif^{1A15}/Df(2L)Exel7029	13 ± 5 (140)	100 (122)
btl-Gal4/UAS-uifRNAi	5 ± 2 (260)	87 ± 6 (247)
UAS-uifRNAi/+; da-Gal4/+	18 ± 5 (294)	86 ± 2 (240)

[a] mean ± sd from three independent experiments
[b] total number of animals of indicated genotype that were scored

shown). In contrast, *uif*^{1A15} is likely a hypomorphic allele since homozygous mutant animals show almost no embryonic lethality, but still display a nearly completely penetrant larval lethality, while *uif*^{1A15}*/Df(2L)Exel7029* mutant animals again show 13% embryonic lethality (Table 3.1).

One completely penetrant phenotype found in all unhatched embryos and newly hatched larvae for all of these mutations was a failure in tracheal inflation (Figure 3.3 and data not shown). Although the penetrance of this phenotype is complete, the expressivity is variable, ranging from animals having completely uninflated trachea to animals having only a small section of uninflated trachea. The entire range of expressivity was found in all genotypes. Brightfield and differential interference contrast (DIC) microscopy of the mutant animals showed clearly that the tracheae were present. Notably, the junctions between inflated and non-inflated regions of the dorsal trunk did not correlate with the location of fusion between adjacent tracheal metameres.

As a means to demonstrate that the tracheal inflation defects resulted from loss of *uif*, we used the UAS-GAL4 system [25] to express a double stranded *uif* RNA construct either ubiquitously in the embryo (using *da-Gal4*) or specifically in the developing tracheal system (using *btl-Gal4*). Expression studies indicated that *btl>uifRNAi* strongly and specifically reduced Uif protein levels in tracheae (Supplemental Figure 3.2). Using either the *da-* or *btl-Gal4* line to induce *uifRNAi*, we observed 5-20% embryonic lethality, with the majority of the hatched embryos dying as larvae (Table 3.1). Importantly, we also observed

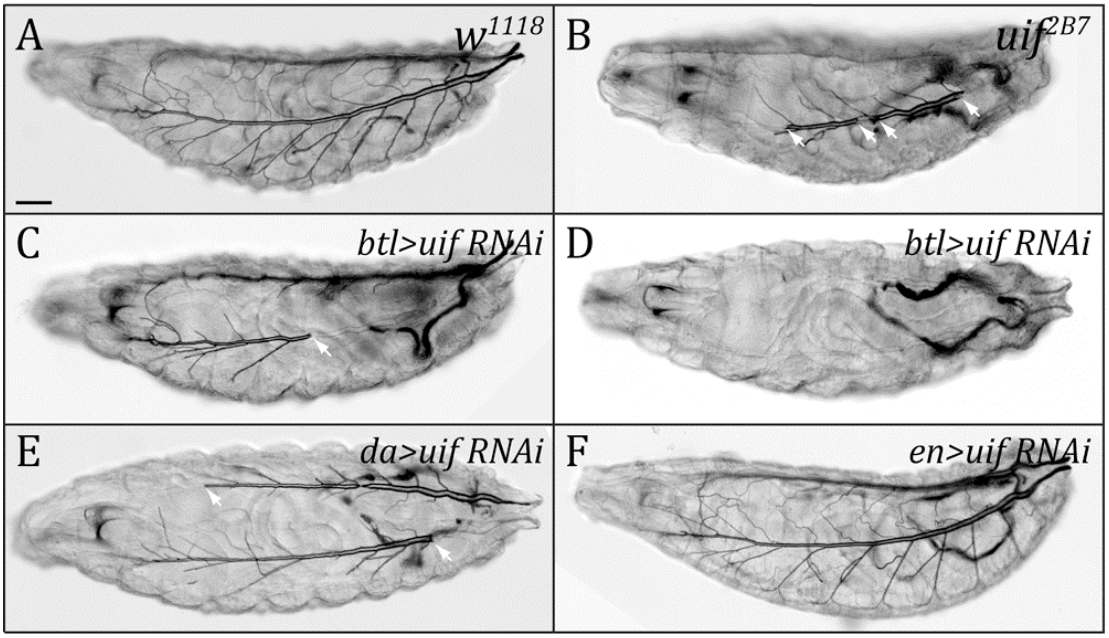

Figure 3.3
***uif* mutant first instar larvae have defects in tracheal inflation**
Brightfield photomicrographs of (A) *w*^{1118}, (B) *uif*^{2B7}, (C, D) *btl-Gal4/UASuifRNAi*, (E) *UASuifRNAi/+; da-Gal4/+*, (F) *en-Gal4/UASuifRNAi*, newly hatched first instar larvae. All animals are depicted with anterior to the left. Refracted light makes the inflated trachea clearly visible in the wild type larva and shows that the tracheae of *uif* mutant animals are partially to completely uninflated. The boundary of inflated/uninflated trachea are marked by arrows in B, C and E. Note that *en>uifRNAi* larvae have normally inflated tracheae. (Scale bar = 50μm.)

a nearly completely penetrant tracheal inflation defect in both cases (Figure 3.3 C-E). Similar to the *uif* loss of function alleles described above, the inflation defects showed variable expressivity with both *Gal4* line used. For example, some *btl>uifRNAi* animals showed mostly inflated tracheae (Figure 3.3 C), whereas other animals had completely uninflated tracheae (Figure 3.3 D). Neither *da-Gal4/+*, *btl-Gal4/+* nor *uif RNAi/+* animals showed any tracheal inflation defects. In contrast, *en>uifRNAi* animals had completely inflated tracheae (n>50 animals, Figure 3.3 E). Therefore, the phenocopied tracheal inflation defects by *uifRNAi*, the lack of tracheal inflation defects associated with *uifRNAi* in posterior compartments of the epidermis, and with the genetic results showing completely penetrant tracheal inflation defects in *uif* homozygous, hemizygous and transheterozygous animals strongly argue that these defects result from loss of *uif* function.

Although in general the tracheal tube length and diameter appeared to be mostly normal in *uif* mutant larvae, we did notice some localized irregularities, including twists, constrictions, and crumpled dorsal trunks (Figure 3.4 B-D). When we used *btlGAl4* to drive the expression of both *uifRNAi* and cytoplasmic green fluorescent protein (*act-GFP*) in the tracheal system, we observed the same defects (Figure 3.4 F). Using fluorescence microscopy, we visualized that it is the apical surface of the tube that display the same patterns as those in the brightfield image, whereas the basal surface of the tracheal tubes generally

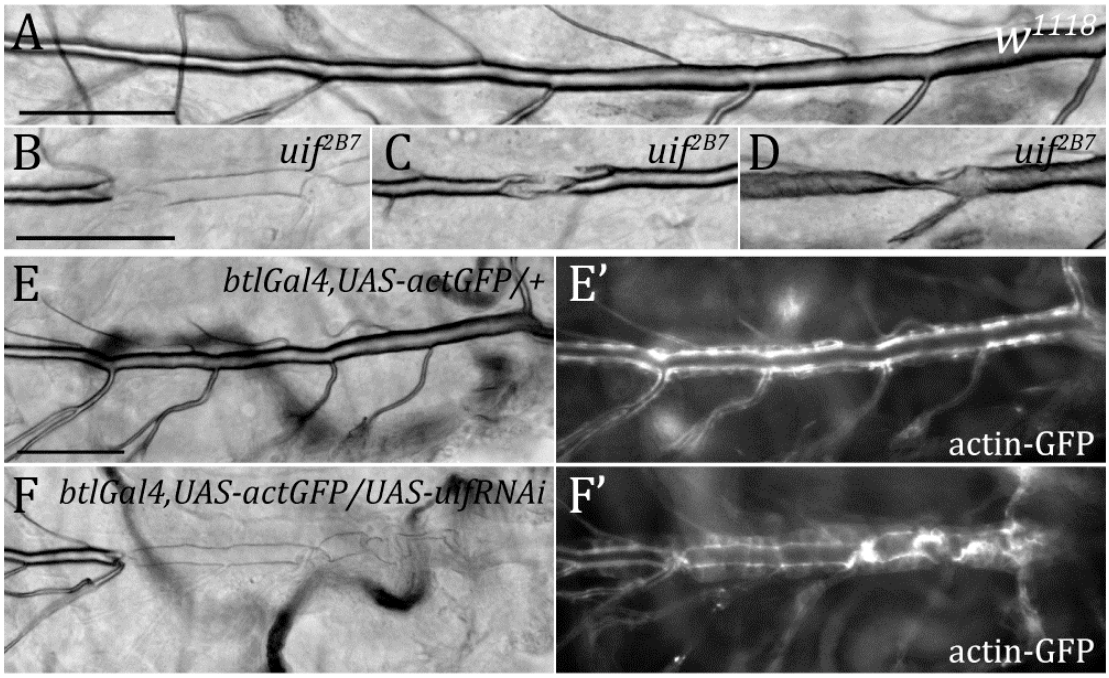

Figure 3.4
***uif* mutant first instar larvae have damaged tracheal tubes**
Brightfield photomicrographs of dorsal tracheal trunks in w^{1118} (A), uif^{2B7} (B-D), *btl-Gal4, UASactGFP/+* (E) and *btl-Gal4, UASactGFP/UASuifRNAi* (F) newly hatched first instar larvae. Note the regular diameter of the inflated dorsal trunk in the wild type larva as it gradually tapers towards the anterior, and contrast that to *uif* mutant tracheae that appear twisted or crushed and show discontinuous regions that are uninflated. Similarly, fluorescent photomicrographs showed smooth and clear dorsal trunk in the wild type larvae (E'), whereas *uif* mutant larvae showed pinched and obstructed dorsal trunk (F'). (Scale bars = 50μm.)

appeared continuous (Figure 3.4 F'). It seems that the tubes are collapsed and obstructed.

uif is required for the establishment rather than the maintenance of tracheal inflation

To determine whether the tracheal inflation defects in *uif*^{2B7} mutant animals resulted from a failure to establish an inflated tracheal system in late embryos or the ability to maintain fully inflated tracheae in early larval life, we used live imaging to monitor tracheal inflation in mutant embryos. As shown in Supplemental Movie 3.1 and Figure 3.5, tracheal inflation begins in late stage 17 after the embryo begins to experience dramatic muscular contractions. In the *uif*^{2B7} embryo shown in Figure 3.5, complete inflation of the dorsal trunk occurred over a 7-minute period, whereas there was little or no inflation of tracheal branches distal to the transverse connective in each segment. The dynamics of tracheal inflation are in strong agreement with that found in wild type animals, which was shown to result in complete inflation of the tracheal system in ~10 minutes [7]. There was no additional inflation of the *uif*^{2B7} tracheae over the next 173 minutes, after which the animal hatched and crawled away. In all, we imaged more than 30 *uif*^{2B7} mutant animals and observed either no inflation, or partial inflation that occurred over a short period of time (<10 minutes) and then remained unchanged throughout the period of observation

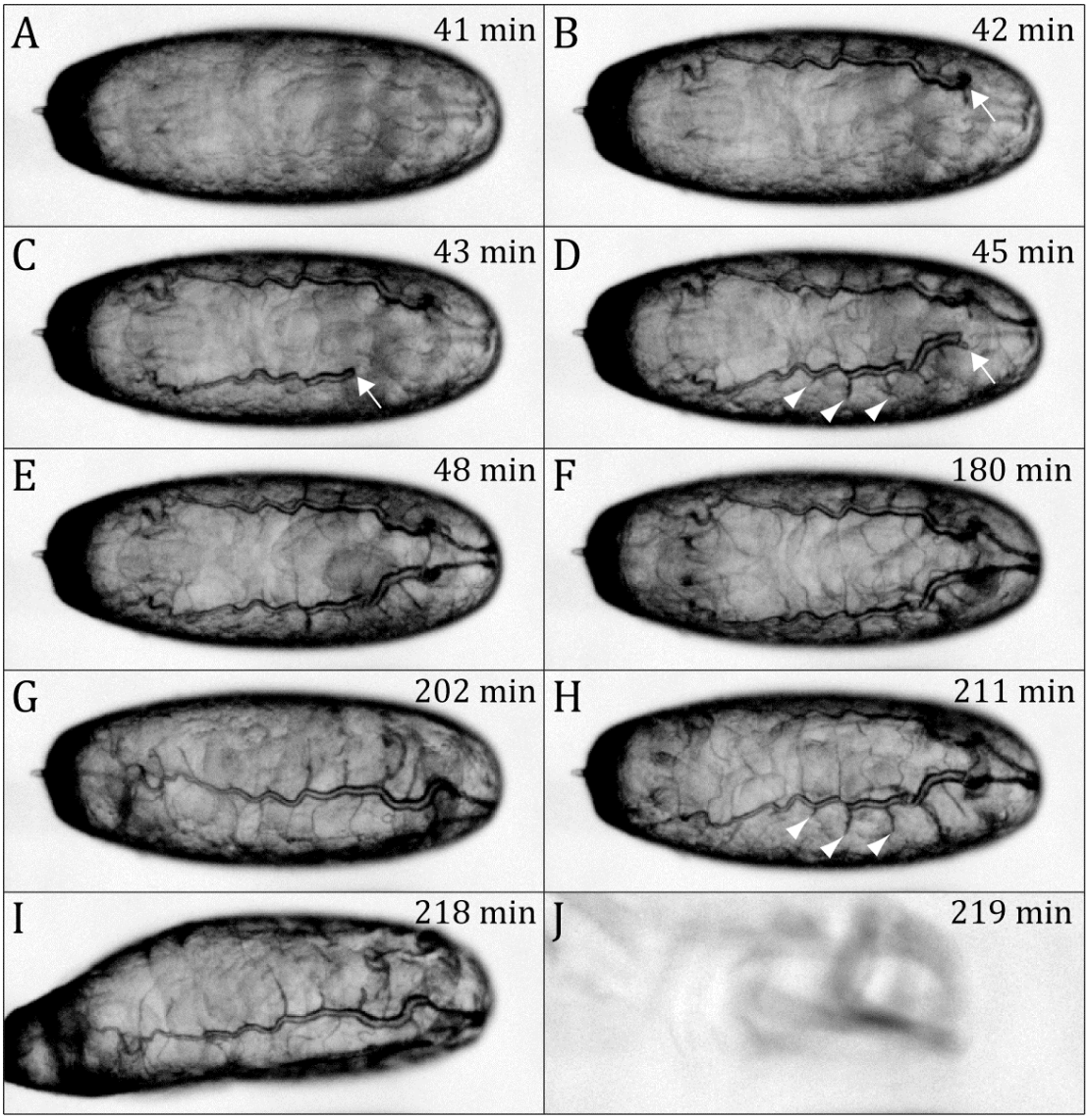
A
41 min
B
42 min
C
43 min
D
45 min
E
48 min
F
180 min
G
202 min
H
211 min
I
218 min
J
219 min

Figure 3.5
***uif*^{2B7} mutant animals fail to establish fully inflated tracheae during embryogenesis.**
Selected brightfield photomicrographs from a time-lapse series of an *uif*^{2B7} mutant embryo showing a rapid period of tracheal inflation (A-E), followed by more than two hours with no additional inflation (F-I). Times given are relative to the start of observation which occurred in mid stage 17 of embryogenesis. The full time series can be seen in Supplemental movie 3.1. Note that the inflation phase lasts for seven minutes and results in fully inflated dorsal trunks with little inflation distal to the transverse connectives in each metamere. Arrows indicate the extent of inflation of the dorsal trunk during the initial inflation phase. Arrowheads in D and H indicate the extent of inflation in three adjacent metameres and show that there is no additional inflation of these segments over a 166 minute period. Even though the animal has not completed tracheal inflation, it hatches and crawls away (J).

(Supplemental Movie 3.1 and data not shown). We additionally collected newly hatched *uif*^{2B7} first instar larvae, separated them into individual apple juice plates, and recorded the degree of tracheal inflation two to three times per day for two days. We observed no obvious changes in the degree of tracheal inflation over those two days (data not shown). Thus we conclude that the tracheal inflation defects seen in *uif* mutant larvae result from a defect in the establishment of inflated tracheae during embryogenesis rather than a defect in maintaining inflated tracheae throughout embryogenesis or into larval life.

Tracheal morphogenesis and maturation are unaffected in *uif* mutant embryos

How might tracheal inflation defects arise in *uif* mutant embryos? It is possible that a defect in tracheal morphogenesis or tube maturation may lead to tubes that are open to the hemocoel or are physically obstructed, thereby preventing complete air filling. To address these possibilities we examined tracheal morphogenesis and maturation in *uif* mutant animals. Here we are presenting the results from our analysis of the amorphic allele *uif*^{2B7}, although identical results were observed with the hypomorphic allele *uif*^{1A15} (data not shown).

Embryos stained with monoclonal antibody 2A12 that recognizes an epitope on the tracheal lumen or with chitin binding probe (CBP) revealed that

tracheal patterning and tube size control are normal in *uif*^{2B7} mutant embryos (Figure 3.6 A-D). Specifically, the metameric pattern of dorsal trunk, dorsal branch, lateral trunk and visceral branch are present and indistinguishable between *uif*^{2B7} and *uif*^{2B7}*/+* embryos (Figure 3.6 A-D and data not shown). Fusion of adjacent metameres was also observed by the correct formation of a three ring E-Cadherin structure at the junction of the two fusion cells (data not shown, but note the three ring structure of these cells by Crumbs staining in *uif*^{2B7} and *uif*^{1A15} mutant embryos in Supplemental Figure 3.2). By stage 16, the diameter of the dorsal trunk in *uif*^{2B7} mutant embryos had expanded to the same degree as it had in *uif*^{2B7}*/+* embryos, and the length of the dorsal trunk was similar between *uif*^{2B7} and *uif*^{2B7}*/+* embryos (Figure 3.6 A-D). Since tube diameter expansion and tube length regulation both require the secretion of chitin into the lumen of the trachea, followed by subsequent endocytosis of the chitin, we stained *uif*^{2B7} mutant embryos with CBP, wheat germ agglutinin (WGA) and Congo Red to verify that these events occurred normally in *uif* mutant embryos. CBP staining demonstrates that the chitin is secreted into the lumen of *uif*^{2B7} mutant tracheal tubes and forms a continuous dense cable through the trachea at stage 16 (Figure 3.6 C-F). Note also that the cable is continuous through the fusion cells joining adjacent metameres, further demonstrating that fusion and cavitation of the dorsal tube had occurred. By stage 17, chitin had been cleared from the center of the tracheal lumen and CBP only recognizes the apical surfaces of the tracheae, exactly as observed in *uif*^{2B7}*/+* animals (Figure 3.6 G-H). We similarly

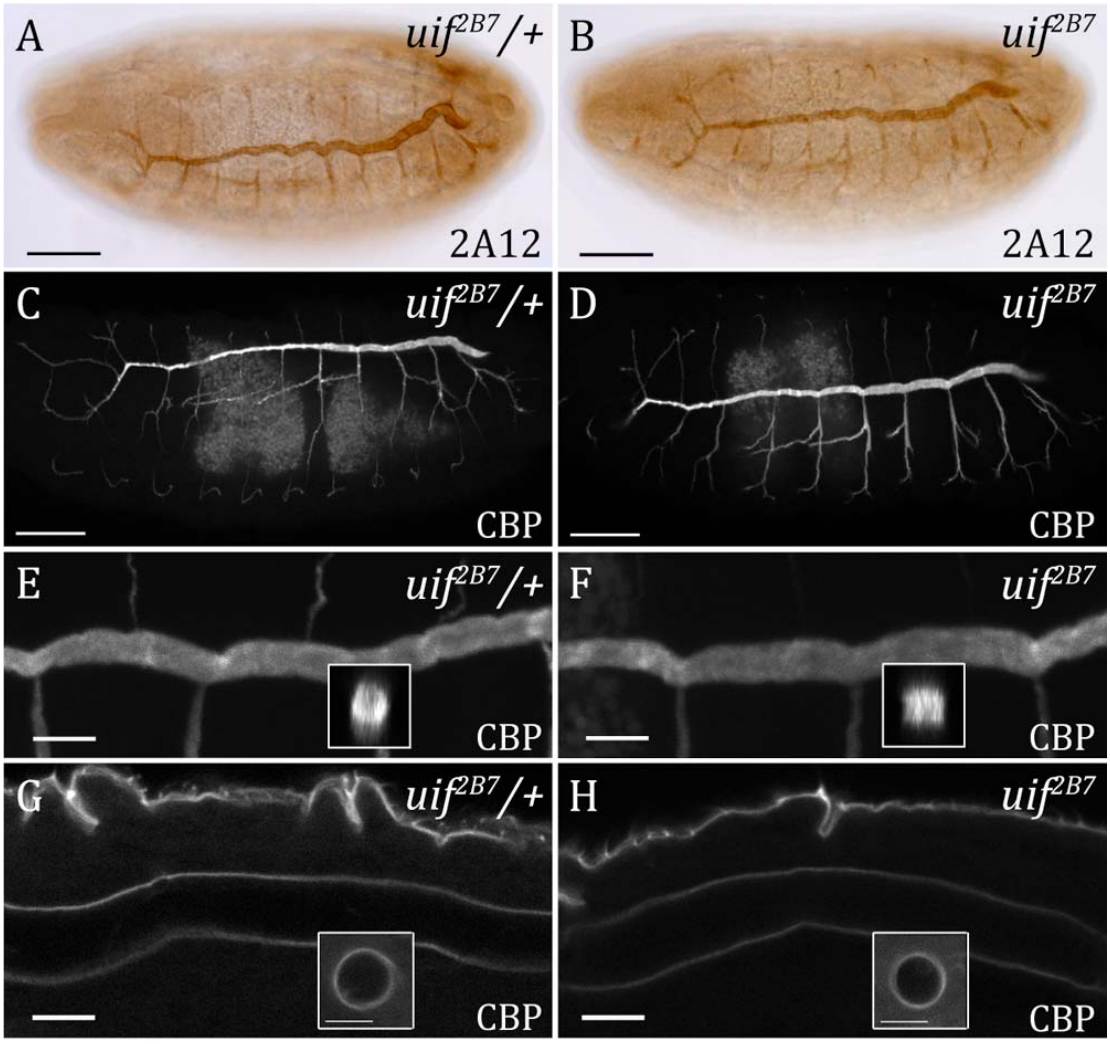
A
uif2B7/+
2A12
B
uif2B7
2A12
C
uif2B7/+
CBP
D
uif2B7
CBP
E
uif2B7/+
CBP
F
uif2B7
CBP
G
uif2B7/+
CBP
H
uif2B7
CBP

Figure 3.6
***uif* mutant embryos have normal tracheal patterning and maturation**
(A-D) 2A12 (A, B) and chitin binding probe (CBP) (C, D) staining of stage16 $uif^{2B7}/+$ and uif^{2B7} embryos demonstrates that tracheal patterning as well as dorsal trunk tube length and diameter are normal in *uif* mutants at this stage of development.
(E-H) Confocal optical sections of $uif^{2B7}/+$ and uif^{2B7} embryos stained with CBP show a continuous chitin cable in the lumens of wild type and *uif* mutant animals at stage 16 (insets in E and F show xz projections of the dorsal trucks) that is completely cleared by mid-stage 17 (insets in G and H show optical cross sections of the dorsal trunk that can be visualized near the posterior of the animals). Note that CBP staining still outlines the apical surface of the dorsal trunk in mid-stage 17 mutant embryos indicating the presence of a chitinous cuticle. In all panels, anterior is to the left. (Scale bars = 50μm in A-D; 10μm in E-H.)

observed a thick chitin cable in stage 16 *uif*^{2B7} mutant embryos using WGA and Congo Red, with only residual staining on the apical surface of stage 17 embryos (data not shown), suggesting that endocytosis of tracheal luminal material had occurred normally in *uif* mutant embryos.

Another possible mechanism that could result in liquid permeable trachea is a defect in the paracellular barrier function of the septate junction in tracheal cells. Intact septate junctions are necessary for the secretion of chitin modifying enzymes into the tracheal lumen and thus play critical roles in tube diameter and length control (described in introduction). However, Paul et al., [26] demonstrated that there is not a perfect correlation between the septate junction barrier function and tube size control, and thus although tube size control appears normal in *uif* mutants, it is possible that Uif could specifically affect the barrier function of the septate junction. To address this possibility we stained *uif*^{2B7}*/+* and *uif*^{2B7} mutant embryos with antibodies against the septate junction proteins Coracle (Cor), Fasciclin III, and Discs Large to assess the integrity of this junction. All three septate junction proteins were correctly localized in the trachea, salivary glands and epidermis of *uif*^{2B7} mutant embryos (Figure 3.7 and data not shown). To test the paracellular barrier function of the septate junctions we performed a dye permeability assay [27]. We found that a 10 kD Rhodamine-labeled dextran injected into the hemocoel of stage 16 *uif*^{2B7} mutant embryos failed to cross the salivary gland and tracheal epithelium into the lumen, indicating that the septate junctions were functionally tight in these

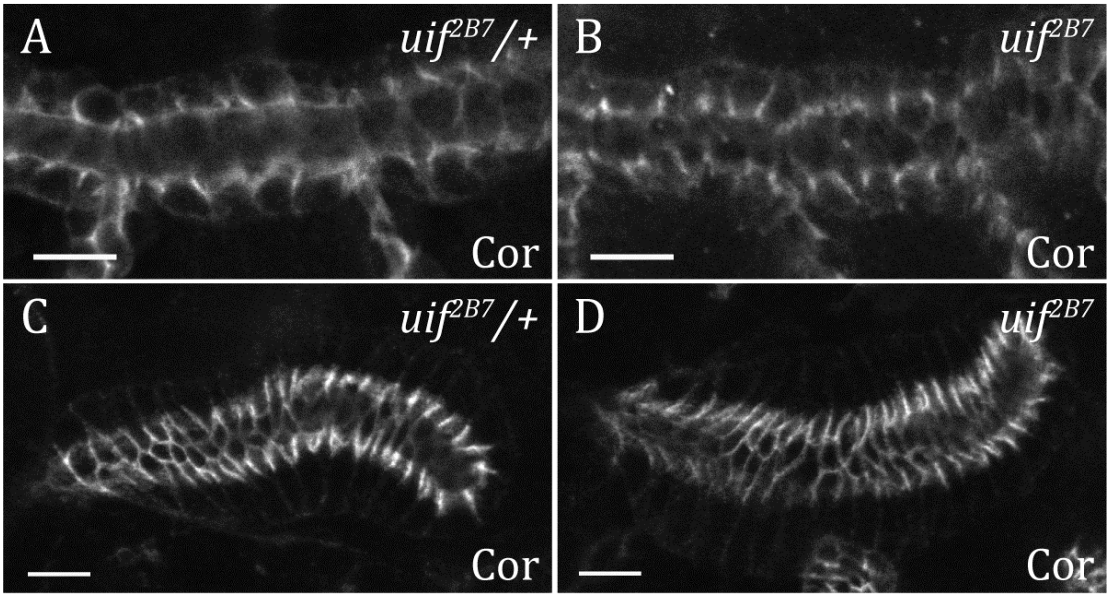

Figure 3.7
***uif* mutant embryos have have intact septate junctions**
Confocal photomicrograph of *uif*^{2B7}/+ and *uif*^{2B7} embryos stained with antibodies against the septate junction protein Coracle (Cor) show the correct localization of this protein in an *uif* mutant trachea (B) and salivary gland (D). In all panels, anterior is to the left. (Scale bars = 10μm.)

animals (data not shown). Taken together, these results demonstrate that tracheal morphogenesis and tube maturation occur normally in *uif* mutant embryos, and that the tracheal inflation defects are likely not a consequence of impaired development of the trachea during embryogenesis.

uif is required for larval tracheal growth

All uif^{2B7} and most uif^{1A15} mutant animals that hatch as larvae die prior to pupariation, with the majority dying as small first instar larvae. We examined three independent cohorts of uif^{2B7} (n=226 mutant animals) and uif^{1A15} (n=124) mutant animals five days after hatching and determined that 25% (± 6%) of the uif^{2B7} and 40% (± 7%) of the uif^{1A15} were still alive. Interestingly, only 13% (± 6%) of the uif^{2B7} and 27% (± 10%) of the uif^{1A15} mutants had advanced to third instar. It was not uncommon to find mutant third instar larvae that were more than 10 days post hatching. The mutant larvae did grow much slower than their heterozygous siblings and typically the largest mutant larvae were only about half the size of their siblings at the time when their siblings pupariated (Figure 3.8 A). A larger percentage of uif^{1A15} larvae grow to this larger size than uif^{2B7} mutant larvae, consistent with the suggestion that uif^{2B7} is an amorphic allele, whereas uif^{1A15} is a strong hypomorphic allele. Interestingly, *btl>uifRNAi* larvae also displayed this strong growth defect, whereas *btl-GAL4/+* and *UAS-uifRNAi/+* larvae did not (data not shown). It is possible that this larval growth defect is

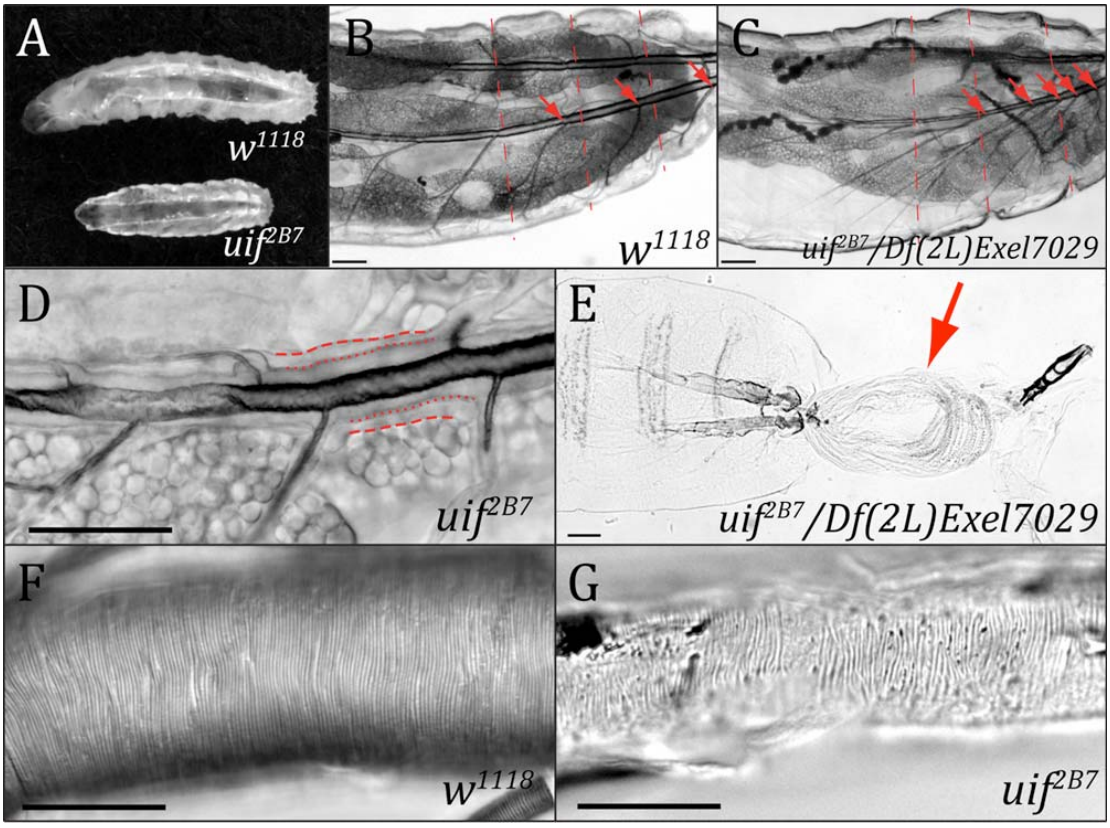
A
w^{1118}
uif^{2B7}
B
w^{1118}
C
$uif^{2B7}/Df(2L)Exel7029$
D
uif^{2B7}
E
$uif^{2B7}/Df(2L)Exel7029$
F
w^{1118}
G
uif^{2B7}

Figure 3.8
***uif* mutant second and third instar larvae have tracheal growth and molting defects**
(A) Brightfield photomicrograph of a 5-day-old w^{1118} 3rd instar larva and a 5-day-old uif^{2B7} 3rd instar larva. Note the smaller overall size of the uif^{2B7} mutant larva. (B, C) Brightfield photomicrograph of a w^{1118} 2nd instar larva and a similarly sized $uif^{2B7}/Df(2L)Exel7029$ 3rd instar larva showing a tracheal growth defect in the *uif* mutant larva. Red lines indicate the relative boundaries of the body segments, whereas red arrows indicate the junction of the transverse connective (TC) branch along the dorsal trunk in each metamere. Note that in the wild type larva one TC emanates from each dorsal trunk in each body segment, whereas in the *uif* mutant larva five TCs emanate from the dorsal trunk in the final two body segments. Also note that the *uif* mutant larva has less fat than the w^{1118} larva. (D) *uif* mutant larvae frequently fail to molt their tracheal cuticle. In this 5-day-old uif^{2B7} mutant 2nd instar larva the dashed lines indicate the basal membrane of the tracheal cells, whereas the dotted lines indicate the apical surface of the tracheal cells. Note the presence of two layers of cuticle with only the inner or 1st instar lumen being inflated.
(E) $uif^{2B7}/Df(2L)Exel7029$ mutant 3rd instar larva that has failed to complete its molt. The previous epidermal cuticle (arrow) is connected at the posterior spiracles.
(F, G) DIC photomicrographs of w^{1118} and uif^{2B7} 3rd instar larval posterior dorsal tracheal trunks. Note the regular pattern of the taenidial folds in the wild type trachea. Although the trachea in G is uninflated, taenidia are present and are organized into roughly parallel rows that run perpendicular to the long axis of the trachea. Scale bars = 100μm in B, C and E; 50μm in D, F and G.

associated with hypoxia as we observed that mutant larvae (*uif*^{2B7}, *uif*^{1A15}, and *btl>uifRNAi*) spend very little time in the food and instead wander around the plate, even if they appear to have mostly inflated trachea. Wingrove and O'Farrell [28] noted similar behavioral responses to hypoxia in larvae. One consequence of this wandering away from food behavior is that the mutant larvae accumulate much less fat and are more transparent than their heterozygous siblings (Figure 3.8 B, C).

An examination of *uif* mutant third instar larvae (*uif*^{2B7}, *uif*^{1A15}, and *btl>uifRNAi*) revealed a strong reduction in tracheal tube length (Figure 3.8 B, C and data not shown). Whereas *uif* mutant tracheal tube length and diameter were indistinguishable from wild type prior to inflation (Figure 3.6 A-D) and still were of wild type size in newly hatched larvae (Figure 3.3 A, B), third instar *uif* tracheae were substantially shorter than those in wild type larvae (even of second instar of comparable size; Figure 3.8 B, C). The most obvious manifestation of this defect was the location of the transverse connective (TC) relative to the body segments. In wild type second and third instar, each abdominal segment had one TC emanating from each dorsal trunk (Figure 3.8 B). In contrast, in *uif* mutant third instar larvae, most of the TCs emanated from portions of the dorsal trunk that corresponded to the final two abdominal segments, with the visceral branches and lateral trunk stretching far anteriorly to tracheate the correct segment (Figure 3.8 C). To gain a quantitative measure of the severity of this growth defect we compared partial tracheal length (along

the dorsal trunk from the posterior spiracle to the TC that originated in abdominal segment 4 during embryogenesis) to full body length for w^{1118} and *uif* mutant larvae (Table 3.2). Interestingly, this ratio did not change in w^{1118} from second to third instar larvae and thus does not appear to be influenced by developmental stage. We found that *uif* mutant third instar larvae had substantially reduced relative tracheal length compared to wild type larvae (Table 3.2).

uif is required for larval tracheal molting

Microscopy of live uif^{2B7} mutant second instar larvae revealed a tracheal molting defect in which two tracheal cuticle layers were clearly present with neither tracheal layer being inflated, or only the first instar trachea being inflated (Figure 3.8 D and data not shown). To more closely examine this tracheal molting defect we dissected portions of the dorsal trunk from w^{1118} and uif^{2B7} and uif^{1A15} third instar larvae and examined them by DIC microscopy. Notably, the *uif* mutant tracheae were substantially more brittle than w^{1118} trachea. Both *uif* mutations showed a completely penetrant defect in tracheal molting in which at least two distinct tracheal cuticles were present and occasionally three cuticular layers could be observed. The molting defect was always detected in the posterior segments closest to the spiracles, but was not always observed in more anterior segments (data not shown). We also observed

Table 3.2
Relative tracheal length in wild type and *uif* mutant larvae

Genotype	Partial tracheal length[a] / total body length (*n*)[b]
w^{1118}, 2nd instar	0.37 ± 0.02 (32)
w^{1118}, 3rd instar	0.37 ± 0.02 (26)
uif^{1A15}, 3rd instar	0.19 ± 0.03 (25)
btl-Gal4/UAS-uifRNAi, 3rd instar	0.24 ± 0.03 (14)

[a] Partial tracheal length = Distance along the dorsal trunk from the posterior spiracle to the TC that originated in body segment A4
[b] total number of animals of indicated genotype that were scored

a weakly penetrant epidermal molting defect in which the previous cuticle remained affixed to the larva at its posterior spiracles (Figure 3.8 E), possibly related to this tracheal molting defect. We inspected the organization of the taenidia in these dissected tracheae by DIC microscopy and found that the tightly packed parallel rows of taenidia were present in the tracheae of uif^{1A15} and uif^{2B7} mutant larvae, although the density of the taenidia appeared lower in uif^{2B7} mutant larvae and there were some local irregularities, most notably regions where the rows converged and appeared to cross each other (Figure 3.8 G). In addition, the taenidia remain in focus for a greater depth in the Z-axis of wild type dorsal trunks than in uif^{2B7} mutant larvae, suggesting that the taenidia might be shallower in mutant tracheae compared to wild type (Figure 3.8 F, G).

Uif localizes to the apical plasma membrane in ectodermally derived epithelia

We performed both RNA *in situ* hybridization and immunostaining of w^{1118} embryos to determine the tissue distribution of *uif* RNA and Uif protein, as well as the subcellular localization of the protein. Expression of *uif* RNA is first detected in stage 5 embryos in cells that are fated to become ectodermal (Figure 3.9 B). *uif* is noticeably reduced or absent in mesodermal and neurectodermal precursors. In later stage embryos, *uif* expression persists in ectodermal tissues and is very strongly expressed in the developing tracheal system (Figure 3.9 C-

F). We generated a polyclonal antiserum against a unique region of the extracellular domain (noted on Figure 3.2 A). This antiserum appears specific as it recognizes an epitope in w^{1118} embryos (Figure 3.10), but not in uif^{2B7} or *Df(2L)Exel7029* mutant embryos (Supplemental Figure 3.2 and data not shown). Interestingly, the antiserum recognizes a protein that is strongly expressed in the tracheae in uif^{1A15} mutant embryos, but rather than localizing to the plasma membrane, the protein remains inside the cell (Supplemental Figure 3.2 E). In wild type embryos, Uif is first detected in the cephalic furrow and ventral furrow at stage 7 (data not shown). Subsequently, Uif staining is detected in the epidermis, foregut, hindgut, salivary gland and is particularly robust in the trachea (Figure 3.10 A).

Subcellularly, Uif localizes to the apical plasma membrane. To determine if Uif spreads into the lateral junctions, we costained w^{1118} embryos with antibodies that recognize Uif and markers for the adherens junction (Armadillo, Arm), septate junction (Coracle, Cor) and the marginal zone (Crumbs, Crb). Uif was found to be more apically localized than Arm and Cor in every embryonic tissue that it was expressed (data not shown). Uif partially co-localizes with Crb in the marginal zone of embryonic epidermal cells, but as detected in cross section views, is also strongly expressed on the apical plasma membrane in a domain where Crb expression is lower (Figure 3.10 B). This apical plasma membrane localization of Uif is most apparent in the tracheal system where Uif localizes in a domain more apical than Crb. For example, during stage 11 when

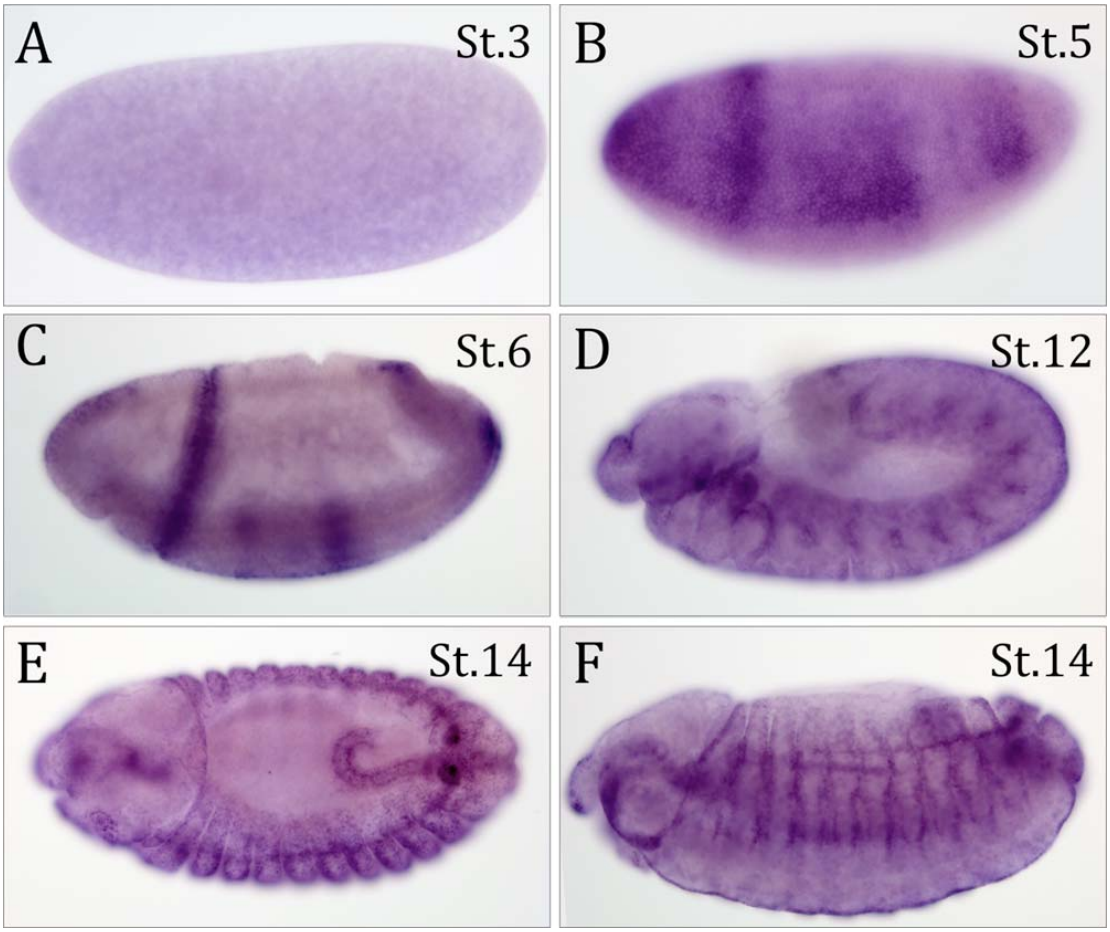

Figure 3.9
***uif* is expressed zygotically in epithelial cells during embryogenesis**
(A) *In situ* hybridization of w^{1118} embryos with an *uif* RNA probe revealed no expression in stage 1-4 embryos (stage 3 embryo shown).
(B) Strong zygotic expression of *uif* RNA can first be detected in stage 5 embryos.
(C) By stage 6, *uif* RNA expression can be detected in ectodermaly-derived epithelial tissues, for example the cephalic furrow and posterior midgut rudiment.
(D) High level *uif* expression is detected in the tracheal placodes of stage 12 embryos.
(E, F) In stage 14 embryos *uif* is expressed at high levels in the hindgut and the tracheae. In all cases anterior is to the left.

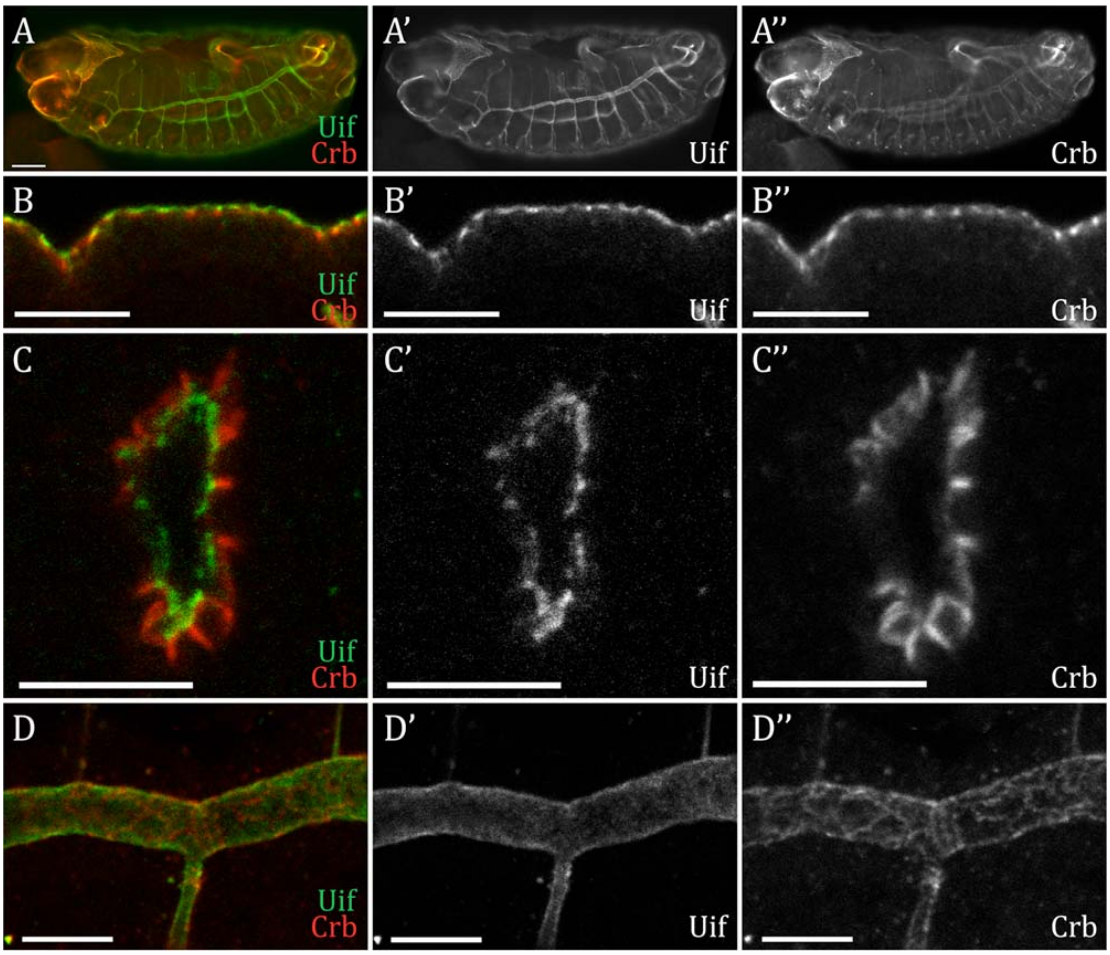

Figure 3.10
Uif is expressed on the apical plasma membrane of ectodermally derived epithelial cells during embryogenesis
(A) Open pinhole confocal micrograph of a stage 15 w^{1118} embryo double labeled with anti-Uif (green) and anti-Crb (red) antibodies. Individual channels are shown for Uif (A') and Crb (A''). Uif expression can be detected in the fore- and hindgut, the epidermis and most strongly in the tracheal system.
(B-D) Higher magnification confocal optical sections of w^{1118} embryos stained with anti-Uif (green) and anti-Crb (red) antibodies. Individual channels are shown for Uif (') and Crb ('). Tissues include the epidermis at stage 14 (B-B"), the tracheal placode at stage 11 (C-C"), and the tracheal dorsal trunk at stage 14 (D-D"). Note that Uif is expressed in a domain that is more apical than Crbs in all of these tissues. In all cases anterior is to the left. In panel B apical is up. In panel C apical is to the center of the placode. Scale bars = 50μm in A; 10μm in B-D.

the tracheal placode is invaginating, Uif is clearly on the apical plasma membrane in a domain distinct from that labeled by Crb (Figure 3.10 C). Similarly, in the dorsal tracheal trunk of stage 14 embryos, Uif protein appears to define the apical lumen of the trachea, whereas Crb staining maintains a cross hatched appearance that defines the marginal zone of the tracheal cells (Figure 3.10 D).

We stained wild type 3rd instar larvae and found that Uif expression persists at high levels in the tracheal system, and is also abundant in the imaginal discs (Figure 3.11). In the adult, we found no expression of Uif in oocytes or in follicle cells (data not shown). The lack of *uif* RNA and Uif protein in early embryos, coupled with the lack of Uif expression in oocytes suggests that *uif* expression is from zygotic transcription and that there is no maternal contribution.

Knockdown of *uif* in imaginal discs leads to Notch-like phenotypes in adult structures

Lethal phase analysis indicated that *UAS-uifRNAi/+; daGal4/+* animals displayed 86% larval lethality (Table 3.1). The remaining animals survived to the adult stage and showed specific defects resembling those of loss of Notch signaling, including notched wings and extra thoracic bristles (Figure 3.12 and data not shown). To examine these phenotypes further, we expressed *uifRNAi*

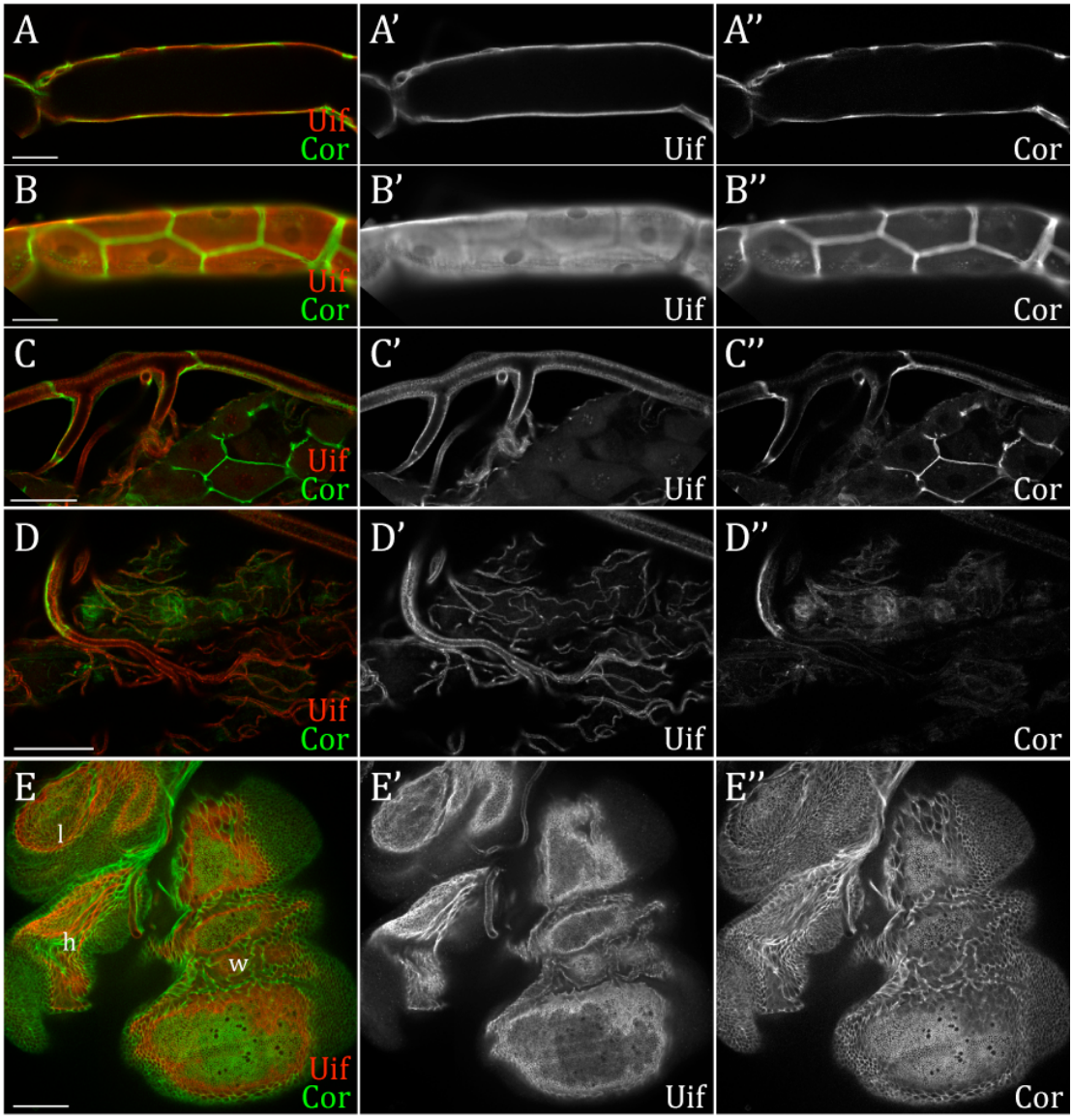
A
Uif
Cor
A'
Uif
A''
Cor
B
Uif
Cor
B'
Uif
B''
Cor
C
Uif
Cor
C'
Uif
C''
Cor
D
Uif
Cor
D'
Uif
D''
Cor
E
l
h
w
Uif
Cor
E'
Uif
E''
Cor

Figure 3.11
Uif is expressed at high level in the larval tracheal system and imaginal discs
Photomicrographs of tissues from w^{1118} 3rd instar larvae double labeled with anti-Uif (red) and anti-Cor (green) antibodies. Individual channels are shown for Uif (') and Cor ('').
(A) Confocal optical sections of tracheal dorsal trunk.
(B) Open pinhole confocal micrograph of the same tracheal trunk in panel A.
(C) Confocal optical sections of some secondary tracheal branches.
(D) Confocal optical sections of terminal tracheal branches around the foregut.
(E) Confocal optical sections of a wing (w), a leg (l) and a haltere (h) imaginal disc.
Note that in A-D, Uif is expressed in the apical domain while Cor is expressed in the junctions of the tracheal cells. Furthermore, Cor cannot be detected in the terminal branches, which are just cytoplasmic extensions of the tracheal cells.
(Scale bars = 50μm.)

using a variety of Gal4 lines and consistently observed Notch phenotypes. Specifically, knockdown of *uif* using *engrailed Gal4* (*enGal4*, expressed in the posterior compartment of the wing disc) resulted in loss of adult wing tissue only in the posterior compartment (Figure 3.13 C). When *apterous Gal4* (*apGal4*) was used to knockdown *uif* in the dorsal compartment of the wing disc, the veins on the dorsal side of the adult wings where thickened (Figure 3.12 D), which is another Notch related phenotype [29]. *distal-less Gal4* (*dllGal4*) was also used to drive *uifRNAi* expression in the wing margin and the leg segments distal to mid tibia. In *dll>uifRNAi* animals, the wings also showed notched margins (data not shown). More interestingly, tarsal segments of adult legs were shortened and the joints between the tarsal segments were missing (Figure 3.12E-F). These defects are all associated with reduced Notch signaling.

To determine if Notch signaling was indeed attenuated by the reduction of *uif* expression in above conditions, we examined the expression of Cut, which has been used as specific readout for Notch signaling [30, 31]. As expected, in *en>uifRNAi* wing discs, both Uif and Cut protein levels are strongly reduced in the posterior compartments (Figure 3.13), confirming a specific reduction in Notch signaling in the *uif* mutant tissues.

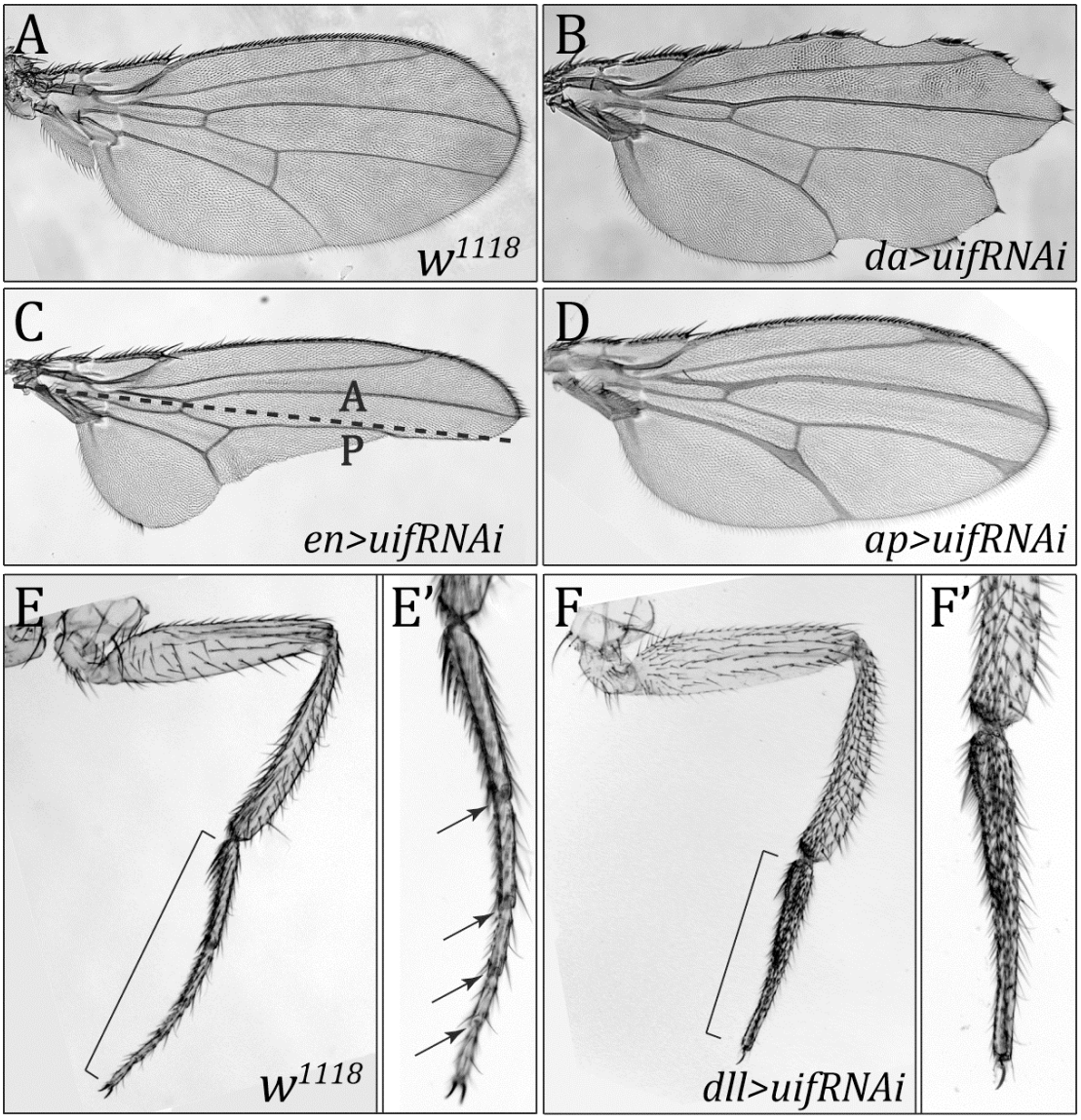
A
w^{1118}
B
da>uifRNAi
C
A
P
en>uifRNAi
D
ap>uifRNAi
E
E'
w^{1118}
F
F'
dll>uifRNAi

Figure 3.12
RNAi-induced knockdown of *uif* leads to Notch-like phenotypes
(A-D) Adult wings from w^{1118} and *uifRNAi* driven by various *Gal4* lines. Expression of *uifRNAi* ubiquitously in the wing disc using *da-Gal4* resulted in notches around the wing margin (B), while expression of *uifRNAi* only in the posterior compartment of the wing disc using *en-Gal4* led to loss of wing tissue only in the posterior half of the wing (C). The line indicates the anterior/posterior boundary. When *ap-Gal4* was used to drive the expression of *uifRNAi* in the dorsal compartment of the wing disc, wing veins on the dorsal side of the adult wings are thickened, which is another Notch-like phenotype (D). (E-F) Adult legs of w^{1118} and *dll>uifRNAi* flies. *Dll-Gal4* was used to drive the expression of *uifRNAi* in the center of the leg disc that will develop into the adult leg segments distal to mid tibia. Note the tarsal segment (brackets in E and F; Higher magnification in E' and F') is much shorter and the joints (arrows in E') are missing in the *uifRNAi* leg (F, F').

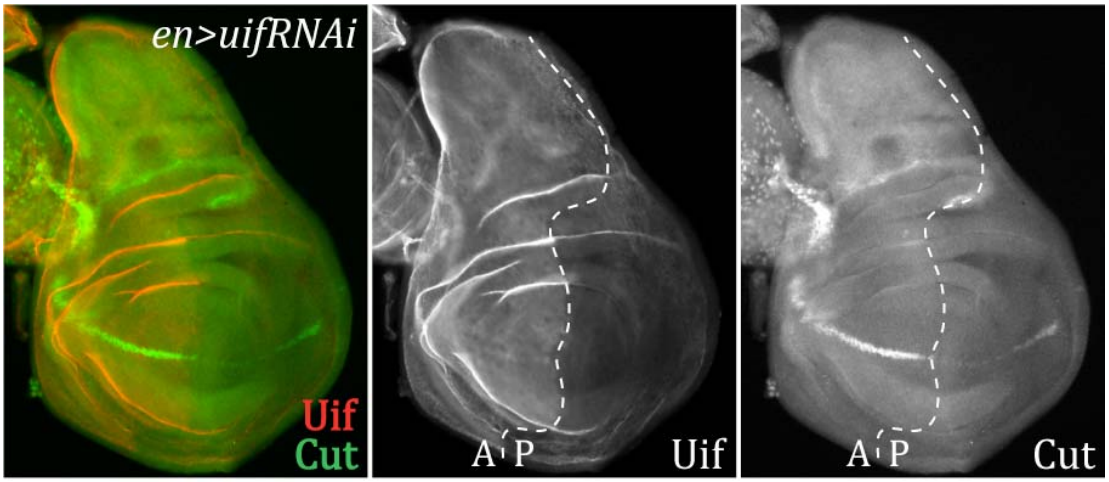

Figure 3.13
RNAi-induced knockdown of *uif* leads to attenuation of Notch signaling
(A) Open pinhole confocal micrograph of a third instar *en> uifRNAi* wing discs double labeled with anti-Uif (green) and Cut (red). Dashed line indicates the anterior/posterior boundary. Uif expression is strongly reduced in the posterior compartment (A'), as is Cut expression (A'').

Discussion

In this report we have described the initial characterization of a novel gene, *uninflatable*, which encodes a single-pass type I transmembrane protein with several different carbohydrate binding motifs and epidermal growth factor repeats in its extracellular domain. This gene is highly conserved in insect species, but does not appear to have a true ortholog in mammals or other vertebrate organisms. Uninflatable is expressed on the apical surface of ectodermally-derived epithelial cells including the epidermis, trachea, salivary gland and fore- and hindgut, although it is most highly expressed in tracheal epithelia starting as the tracheal placode invaginates and persisting throughout its development. We isolated three mutant alleles of *uif*, and found that the predominant defects associated with loss of *uif* were defective air inflation at the end of embryogenesis, and tracheal growth and molting defects in larvae. Loss of *uif* attenuates Notch signaling in the imaginal discs, giving rise to a range of Notch-like phenotypes in the adults.

Functions of *uif* during embryogenesis

The most obvious defects observed in *uif* mutant late embryos and newly hatched first instar larvae were incomplete inflation of the trachea coupled with tracheal tubes that often appeared pinched or stretched. Live imaging of

individual *uif* mutant embryos and larvae revealed that these tracheal inflation defects result from the inability to completely inflate the trachea at the end of embryogenesis rather than a defect in the maintenance of an inflated tracheal system after hatching. Interestingly, tracheae in *uif* mutant embryos are normally patterned and appear to mature in a manner indistinguishable to tracheae in wild type animals. Thus this tracheal inflation defect likely results from a requirement for *uif* function late during embryogenesis.

Several genes have been characterized whose defects include incomplete tracheal inflation. Included in these genes are those that function at the end of embryogenesis to modify or clear the trachea of solid luminal material. This process requires clathrin-mediated endocytosis and includes the proteins clathrin heavy chain, the GTPase dynamin (encoded by *shibire*), and a clathrin binding transmembrane protein encoded by *wurst* [10]. Notably, mutations in all of these genes also result in elongated tracheal tubes suggesting a defect in tracheal tube size control. Gas filling defects were also observed by Behr et al., [10] for mutations in *serp* and *verm*, two putative matrix chitin deacytlases that function to regulate tracheal tube length [8, 9]. Tracheal maturation appears normal in *uif* mutant embryos, including the secretion of chitin into the tracheal lumen and the subsequent uptake of luminal solids near the end of embryogenesis (as indicated by chitin binding probe staining in Figure 3.4, and WGA and Congo Red staining that were not shown). In addition, *uif* mutant tracheae do not show diameter or length defects, suggesting that the luminal

chitin cylinder forms normally and that Serp and Verm are correctly functioning during the maturation process. Taken together these results suggest that the air filling defects observed in *uif* mutant embryos occurs through a mechanism independent of that linked to endocytosis of solid luminal material.

A second class of proteins that likely function in proper air inflation is the epithelial sodium channels (ENaCs). In mammals, ENaC proteins are required to help remove liquid from embryonic lung prior to birth [32]. There are 16 *ENaC* genes (also referred to as *pickpocket* or *ppk* genes) in the *Drosophila* genome, of which 9 are expressed in the embryonic tracheal system [12]. It is thought that the influx of sodium through these channels drives water from the lumen into the epithelial cells, and that degassing of this liquid inflates the trachea. Although there are no loss of function mutations in ENaCs that result in air filling defects in *Drosophila*, RNA interference mediated knockdown of *ppk4* and *ppk11* results in partially liquid-filled tracheae in larvae [12]. In addition, inhibiting these channels using amiloride also results in fluid filled tracheae in larvae. Although both of these examples affected air filling after a molt, it seems likely that ENaC proteins may also contribute to air filling at the end of embryogenesis. At this point we cannot exclude the possibility that *uif* may regulate the expression or activity of *ENaC* encoded proteins in tracheal epithelia.

A third possibility, and one that we favor, is that *uif* is playing primarily a structural role in embryonic tracheal maturation. Two pieces of evidence support this notion. First, in early stage 17 mutant embryos the tracheae are of

normal length and diameter and have a stereotypic appearance that is indistinguishable from that of wild type animals, whereas in newly hatched mutant larvae the tubes are often crushed or twisted. Second, while dissecting tracheae from wild type and *uif* mutant third instar larvae it was clear that the mutant tracheae were more brittle. Wild type tracheae have an elastic property that makes them difficult to break, whereas we had to be very careful dissecting *uif* tracheae in order to get a section that included more than one metameric unit. Together these observations suggested a model in which the mechanical properties of *uif* mutant tracheae are compromised, thereby allowing the tracheal cuticle to fail when the embryo initiates violent muscular contractions prior to hatching. As noted in the live imaging, tracheal inflation initiates well after the embryo begins these dramatic muscular contractions. We predict that a combination of crushed tubes and small cracks in the tracheal cuticle prevent complete inflation.

Functions of *uif* in larvae

uif mutant larvae that survive to second or third instar show striking defects in tracheal growth and tracheal molting. The tracheae in these *uif* mutant larvae have short dorsal trunks that are well out of proportion to the body length of the animal. It is difficult to accurately assess the diameter of the dorsal trunk in these animals, however, because the mutant animals fail to completely shed

their tracheal cuticle, and often only the first instar lumen is inflated. This tracheal molting defect was nearly completely penetrant in all third instar *uif*^{2B7} and *uif*^{1A15} mutant larvae examined, but the severity seemed to vary along the anterior-posterior axis, with some middle and anterior sections showing no molting defects, whereas the sections near the posterior spiracles showed at least two and sometimes three tracheal cuticles. Beitel and Krasnow (2000) conducted morphometric analyses of larval tracheal growth and observed that the tracheae lengthen in a continuous fashion, whereas the diameter increases in a stepwise manner coincident with the molt, suggesting that tube length is controlled independently from tube diameter. Our results clearly indicate that *uif* plays a role in regulating the growth of the tracheae along their length.

How might *uif* regulate larval tracheal tube length? One possibility is that Uif might regulate the interface between the tracheal epithelium and the cuticle, possibly by providing lubrication through its hyalin domains. Loss of *uif* would therefore result in a situation where the epidermis is too tightly bound to the overlying cuticle to allow for growth along the long axis of the tracheae. This type of mechanism could also account for the tracheal molting defects and thereby couple these phenotypes. Page-McCaw et al., [33] identified mutations in the Matrix Metalloproteinase encoded by *Mmp1* and found similar defects in tracheal elongation. They also speculated that the *Mmp1* tracheal defects might be caused by the inability of the tracheal epithelial cells to loosen their attachment to the cuticle. Since *uif*^{2B7} mutant larvae have no full length Uif

protein, it is unlikely that Uif is a primary target of MMP1 in tracheal cells. In addition, we observed no genetic interaction between *uif* and *Mmp1* by second-site noncomplementation (data not shown).

An alternative hypothesis is that Uif might serve as a receptor or co-receptor for a systemic signal that couples tracheal growth with larval growth. The extracellular domain of Uif contains multiple EGF domains and a laminin G domain, and the cytoplasmic domain is remarkably conserved in all insect species. A combination of structure/function analysis and genetic and biochemical approaches to identify Uif interacting proteins should help to shed light on this functions of *uif*. Understanding how Uif couples tracheal growth to the growth of the larva may serve as an important paradigm for similar couplings of organ growth to organismal growth in other species.

Finally, hypoxia may account for all the other larval phenotypes associated with loss of *uif*, including early larval lethality, slow growth, developmental arrest and failure to pupariate. Most *uif* mutant larvae die as first instars, and those that die early almost invariably have the most severe tracheal inflation defects. *uif* mutant larvae that survive to second or third instar grow much slower than their heterozygous siblings. *btl>uifRNAi* larvae that have only lost *uif* function in their tracheae show an identical slow growth phenotype. We consistently observed *uif* mutant larvae wandering away from food, suggesting that they were experiencing hypoxia [28]. Not surprisingly these larvae accumulate less fat and have a transparent appearance. Examination of the

tracheae in these mutant animals revealed that the inflated portion of the trachea was often just through the first instar tracheal lumen, and therefore these animals were likely oxygen starved as well. Consistent with this notion, we observed additional tracheal branching in these mutant animals suggesting that the hypoxia induced factor pathway had been engaged (data not shown). Thus, hypoxia could explain the growth defects observed in *uif* mutant larvae. And these growth defects may have resulted in the observed developmental delays. For example, mutant third instar larvae may not have reached a critical weight threshold needed for pupariation, and thus would not have been able to pupariate even if they experienced the metamorphic pulse of ecdysone (we have not determined if they received this signal). Interestingly, many *uif* mutants even failed to advance to third instar, but this did not reflect a defect in molting or ecdysis, as we found no evidence for an extra set of head skeleton or epidermal cuticle. Rather the animals just arrested as first or second instars. It is possible that hypoxia-induced growth defects contributed to this phenotype as well, since larvae have to attain a critical size to be competent for molting, just as they do for pupariation [34].

uif could be a positive regulator of Notch signaling

Reduction of *uif* in the imaginal discs gives rise to *Notch*-like phenotypes in corresponding adult tissues, including notched wings, thickened wing veins,

and shortened and fused leg segments. Previous studies indicated that Notch signaling specifies and promotes development of the cells at the dorsoventral boundary in the wing imaginal discs. Consequently, attenuation of Notch signaling in these cells results in loss of margin tissue in adult wings (reviewed in Lai 2004 [35]). Notch signaling is also involved in refining the broad proveins into narrower mature veins. Removal of either *Notch* or its ligand *Delta* during the pupal stages causes broad veins in adult wings (reviewed in Blair 2007 [36]). In the legs, activation of Notch signaling is necessary and sufficient for specifying the joints between the segments and is sufficient for promoting growth [37]. Thus, all the defects resulted from knockdown of *uif* are Notch loss-of-function phenotypes. In addition, the expression of Cut, which is a downstream factor and target of Notch, was strongly reduced in the area where *uif* expression was reduced. Taken together, these results suggest that Uif may be a positive regulator or co-activator of Notch signaling. More experiments are still need to further support this notion. For example, we would like to determine the expression and subcellular distribution of components of the Notch signaling pathway in *uifRNAi* backgrounds or *uif* homozygous mutant clones.

Although all the phenotypes seem to be Notch specific, we still need to examine the possibility that *uif* is affecting certain general cellular events that can result in defects resemble Notch defects but may also be affecting other signaling events as well. For example, *uif* may be generally involved in endocytosis. Since Notch needs to be endocytosed and processed to function

after ligand binding, these defects may seem Notch specific. In this case, loss of endocytosis may affect other signaling pathways as well. For example, loss of endocytosis may result in increased Egfr signaling. The thickened vein in *ap>uifRNAi* may be consistent with this hypothesis. During embryonic tracheal morphogenesis, *uif* does not seem to affect endocytosis, thus this may reflect a tissue specific requirement for Uif during endocytosis in imaginal disc. The examination of other signaling pathways in imaginal discs, including Egfr and Dpp may shed light on this hypothesis, or may suggest alternative possibility of the role of Uif in imaginal discs.

Reference

1. Affolter, M., and Caussinus, E. (2008). Tracheal branching morphogenesis in Drosophila: new insights into cell behaviour and organ architecture. Development *135*, 2055-2064.
2. Ghabrial, A., Luschnig, S., Metzstein, M.M., and Krasnow, M.A. (2003). Branching morphogenesis of the Drosophila tracheal system. Annual review of cell and developmental biology *19*, 623-647.
3. Araujo, S.J., Aslam, H., Tear, G., and Casanova, J. (2005). mummy/cystic encodes an enzyme required for chitin and glycan synthesis, involved in trachea, embryonic cuticle and CNS development--analysis of its role in Drosophila tracheal morphogenesis. Dev. Biol. *288*, 179-193.
4. Devine, W.P., Lubarsky, B., Shaw, K., Luschnig, S., Messina, L., and Krasnow, M.A. (2005). Requirement for chitin biosynthesis in epithelial tube morphogenesis. Proc. Natl. Acad. Sci. U S A *102*, 17014-17019.
5. Tonning, A., Hemphala, J., Tang, E., Nannmark, U., Samakovlis, C., and Uv, A. (2005). A transient luminal chitinous matrix is required to model epithelial tube diameter in the Drosophila trachea. Dev. Cell *9*, 423-430.
6. Swanson, L.E., and Beitel, G.J. (2006). Tubulogenesis: an inside job. Curr Biol *16*, R51-R53.
7. Tsarouhas, V., Senti, K.A., Jayaram, S.A., Tiklova, K., Hemphala, J., Adler, J., and Samakovlis, C. (2007). Sequential pulses of apical epithelial secretion and endocytosis drive airway maturation in Drosophila. Dev. Cell *13*, 214-225.
8. Luschnig, S., Batz, T., Armbruster, K., and Krasnow, M.A. (2006). serpentine and vermiform encode matrix proteins with chitin binding and deacetylation domains that limit tracheal tube length in Drosophila. Curr. Biol. *16*, 186-194.
9. Wang, S., Jayaram, S.A., Hemphala, J., Senti, K.A., Tsarouhas, V., Jin, H., and Samakovlis, C. (2006). Septate-junction-dependent luminal deposition of chitin deacetylases restricts tube elongation in the Drosophila trachea. Curr. Biol. *16*, 180-185.
10. Behr, M., Wingen, C., Wolf, C., Schuh, R., and Hoch, M. (2007). Wurst is essential for airway clearance and respiratory-tube size control. Nat. Cell Biol. *9*, 847-853.
11. Matusek, T., Djiane, A., Jankovics, F., Brunner, D., Mlodzik, M., and Mihaly, J. (2006). The Drosophila formin DAAM regulates the tracheal cuticle pattern through organizing the actin cytoskeleton. Development *133*, 957-966.
12. Liu, L., Johnson, W.A., and Welsh, M.J. (2003). Drosophila DEG/ENaC pickpocket genes are expressed in the tracheal system, where they may

be involved in liquid clearance. Proc. Natl. Acad. Sci. U S A *100*, 2128-2133.
13. Beitel, G.J., and Krasnow, M.A. (2000). Genetic control of epithelial tube size in the Drosophila tracheal system. Development *127*, 3271-3282.
14. Zhang, L., and Ward, R.E. (2009). uninflatable encodes a novel ectodermal apical surface protein required for tracheal inflation in Drosophila. Developmental biology *336*, 201-212.
15. Ward, R.E., Evans, J., and Thummel, C.S. (2003). Genetic modifier screens in Drosophila demonstrate a role for Rho1 signaling in ecdysone-triggered imaginal disc morphogenesis. Genetics *165*, 1397-1415.
16. Dietzl, G., Chen, D., Schnorrer, F., Su, K.C., Barinova, Y., Fellner, M., Gasser, B., Kinsey, K., Oppel, S., Scheiblauer, S., et al. (2007). A genome-wide transgenic RNAi library for conditional gene inactivation in Drosophila. Nature *448*, 151-156.
17. Le, T., Liang, Z., Patel, H., Yu, M.H., Sivasubramaniam, G., Slovitt, M., Tanentzapf, G., Mohanty, N., Paul, S.M., Wu, V.M., et al. (2006). A new family of Drosophila balancer chromosomes with a w- dfd-GMR yellow fluorescent protein marker. Genetics *174*, 2255-2257.
18. Edgar, R.C. (2004). MUSCLE: multiple sequence alignment with high accuracy and high throughput. Nucleic Acids Res. *32*, 1792-1797.
19. Rasband, W.S. (1997-2009). ImageJ. National Institutes of Health, Bethesda, MD, USA.
20. Fehon, R.G., Johansen, K., Rebay, I., and Artavanis-Tsakonas, S. (1991). Complex cellular and subcellular regulation of notch expression during embryonic and imaginal development of *Drosophila*: implications for notch function. The Journal of cell biology *113*, 657-669.
21. Fehon, R.G., Dawson, I.A., and Artavanis-Tsakonas, S. (1994). A Drosophila homologue of membrane-skeleton protein 4.1 is associated with septate junctions and is encoded by the coracle gene. Development *120*, 545-557.
22. Krogh, A., Larsson, B., von Heijne, G., and Sonnhammer, E.L. (2001). Predicting transmembrane protein topology with a hidden Markov model: application to complete genomes. J. Mol. Biol. *305*, 567-580.
23. Russ, W.P., and Engelman, D.M. (2000). The GxxxG motif: a framework for transmembrane helix-helix association. J. Mol. Biol. *296*, 911-919.
24. Consortium, T.H.G.S. (2006). Insights into social insects from the genome of the honeybee Apis mellifera. Nature *443*, 931-949.
25. Brand, A.H., and Perrimon, N. (1993). Targeted gene expression as a means of altering cell fates and generating dominant phenotypes. Development *118*, 401-415.
26. Paul, S.M., Ternet, M., Salvaterra, P.M., and Beitel, G.J. (2003). The Na+/K+ ATPase is required for septate junction function and epithelial tube-size control in the Drosophila tracheal system. Development *130*, 4963-4974.

27. Lamb, R.S., Ward, R.E., Schweizer, L., and Fehon, R.G. (1998). Drosophila coracle, a member of the protein 4.1 superfamily, has essential structural functions in the septate junctions and developmental functions in embryonic and adult epithelial cells. Mol. Biol. Cell *9*, 3505-3519.
28. Wingrove, J.A., and O'Farrell, P.H. (1999). Nitric oxide contributes to behavioral, cellular, and developmental responses to low oxygen in Drosophila. Cell *98*, 105-114.
29. Huppert, S.S., Jacobsen, T.L., and Muskavitch, M.A. (1997). Feedback regulation is central to Delta-Notch signalling required for Drosophila wing vein morphogenesis. Development (Cambridge, England) *124*, 3283-3291.
30. Gonzalez, A., Chaouiya, C., and Thieffry, D. (2006). Dynamical analysis of the regulatory network defining the dorsal-ventral boundary of the Drosophila wing imaginal disc. Genetics *174*, 1625-1634.
31. Jack, J., and DeLotto, Y. (1992). Effect of wing scalloping mutations on cut expression and sense organ differentiation in the Drosophila wing margin. Genetics *131*, 353-363.
32. Hummler, E., Barker, P., Gatzy, J., Beermann, F., Verdumo, C., Schmidt, A., Boucher, R., and Rossier, B.C. (1996). Early death due to defective neonatal lung liquid clearance in alpha-ENaC-deficient mice. Nat. Genet. *12*, 325-328.
33. Page-McCaw, A., Serano, J., Sante, J.M., and Rubin, G.M. (2003). Drosophila matrix metalloproteinases are required for tissue remodeling, but not embryonic development. Dev. Cell *4*, 95-106.
34. Nijhout, H.F. (1981). Physiological control of molting in insects. Am. Zool. *21*, 631-640.
35. Lai, E.C. (2004). Notch signaling: control of cell communication and cell fate. Development (Cambridge, England) *131*, 965-973.
36. Blair, S.S. (2007). Wing vein patterning in Drosophila and the analysis of intercellular signaling. Annual review of cell and developmental biology *23*, 293-319.
37. Rauskolb, C., and Irvine, K.D. (1999). Notch-mediated segmentation and growth control of the Drosophila leg. Developmental biology *210*, 339-350.
38. Tweedie, S., Ashburner, M., Falls, K., Leyland, P., McQuilton, P., Marygold, S., Millburn, G., Osumi-Sutherland, D., Schroeder, A., Seal, R., et al. (2009). FlyBase: enhancing Drosophila Gene Ontology annotations. Nucleic acids research *37*, D555-559.

Supplemental information

Genomic organization of *uif*

The *uif* gene spans 37kb in cytological region 27D1-D3 on the left arm of the second chromosome. Flybase [38] predicts two transcripts containing either 13 exons (*uif-RA*) or 14 exons (*uif-RB*), differing only by an intron that divides the final exon in two (Supplemental Figure 3.1 A). These transcripts are predicted to produce mRNAs of either 11,701 or 11,636 nucleotides, respectively. We tested all the predicted exon/intron boundaries through sequence analysis of RT-PCR products derived from RNA isolated from w^{1118} late embryos and wing imaginal discs and confirmed all predicted boundaries, except that we only observed the divided terminal exon (*uif-RB*), suggesting that *uif-RA* is not expressed. In support of this notion, there are no reported ESTs for the *uif-RA* isoform, although there are many ESTs for the *uif-RB* isoform [38]. In addition, the protein sequences predicted in the other insect species (see Figure 3.2 B) support the identity of *uif-RB*, but not *uif-RA*. Taken together, these results suggest that *uif-RA* is likely a prediction artifact and is not really expressed in *Drosophila*.

By using primer sets for various combinations of upstream and downstream exons, we uncovered an alternative splice variant of *uif* (referred to as *uif-RC*) resulting from the inclusion of a new exon between exon 10 and 11 of

uif-RB (Supplemental Figure 3.1 A). This exon contains 96 base pairs (Supplemental Figure 3.1 C), and thus its inclusion results in the addition of 32 extra amino acids while retaining the reading frame for the gene (Supplemental Figure 3.1), resulting in a protein of 3589 amino acids. Based upon our RT-PCR results (non-quantitative), both transcripts appear to be well represented in both embryos and imaginal discs (Supplemental Figure 3.1 B).

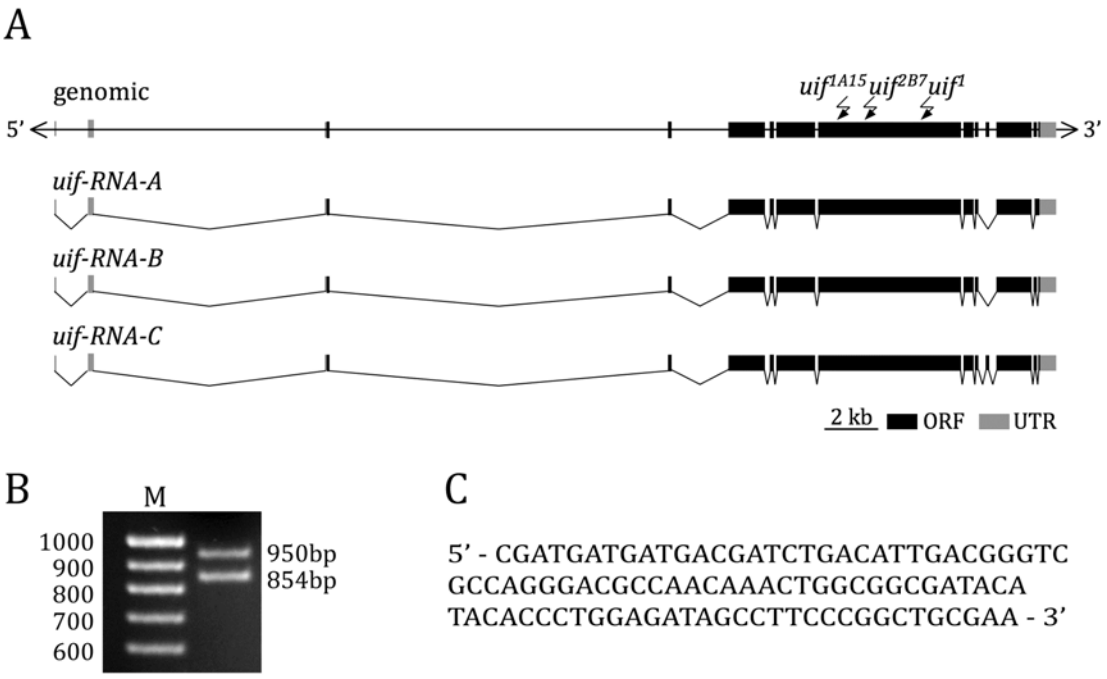

Supplemental Figure 3.1
Genomic organization of *uif*
(A) Structure of the *uif* genomic locus. Black bars indicate coding exons whereas grey bars indicate noncoding exons. *uif-RNA-A* and *uif-RNA-B* isoforms were predicted by flybase [38], whereas the *uif-RNA-C* isoform was detected in this study. The relative positions of the uif^{1A15}, uif^{2B7} and uif^{1} mutations are shown. (B) PCR from an embryonic cDNA library using primers from exons 9 and 11 of *uif-RNA-B* reveals the presence of two alternative spliced variants differing by 96 bp. Lane marked by M shows a 100 bp ladder. (C) Nucleotide sequence of the newly identified exon between exon 10 and 11 of *uif-RB*. This exon comprises the reverse complement to nucleotides 25674-25769 of GenBank sequence **AC008326**.

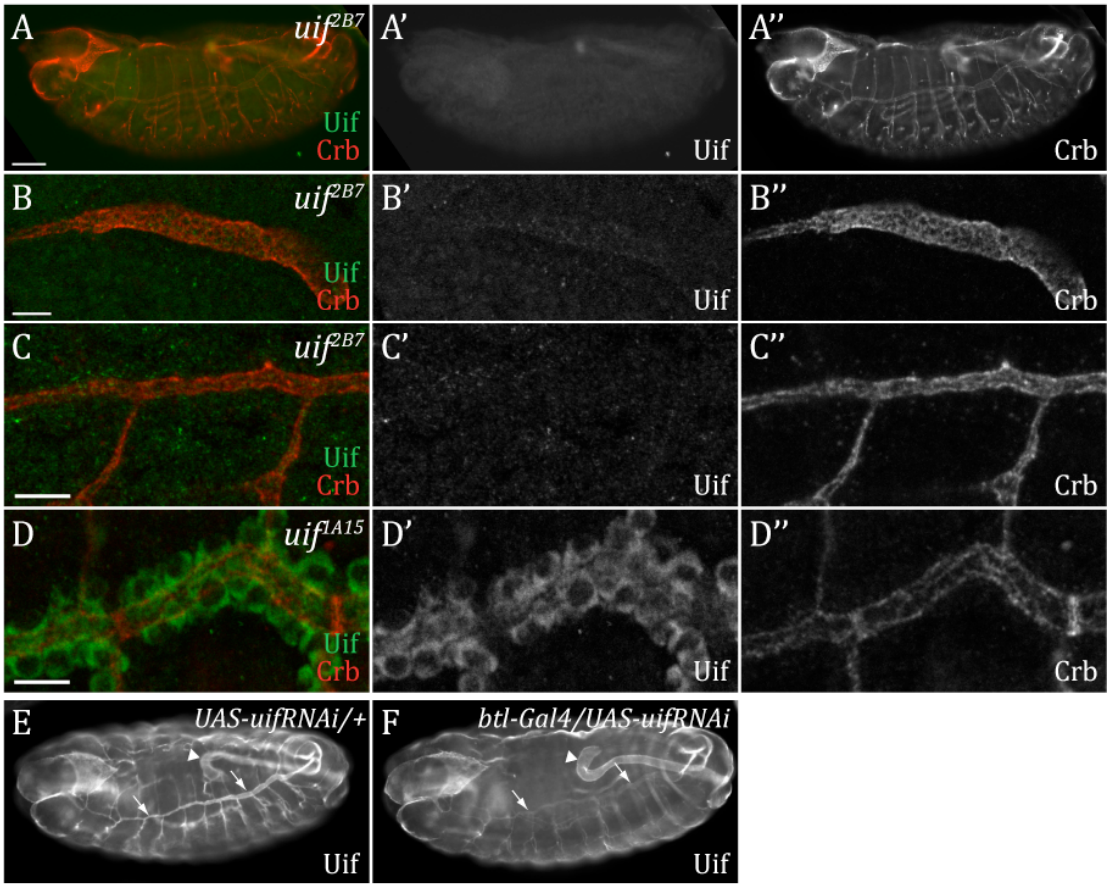

Supplemental Figure 3.2
The anti-Uif antibody is specific and demonstrates that Uif is largely localized within the cell in *uif^{1A15}* mutant embryos
(A) Open pinhole confocal micrograph of a *uif^{2B7}* stage 15 embryo stained with antibodies against Uif (green) and Crb (red) showing no Uif staining in the mutant embryo. Individual channels are shown for Uif (A') and Crb (A''). (B, C) Higher magnification confocal optical sections of *uif^{2B7}* embryos stained with anti-Uif (green) and anti-Crb (red) antibodies. Individual channels are shown for Uif (') and Crb ('). Tissues include the salivary gland at stage 14 (B-B") and the dorsal tracheal trunk at stage 15 (C-C"). (D) Confocal optical section of a stage 16 *uif^{1A15}* mutant embryo stained with antibodies against Uif (green) and Crb (red). Note that Uif protein is trapped inside of the cell. (E, F) Confocal optical sections of a stage 15 *UAS-uifRNAi/+* embryo (E) and a *btl-Gal4/UAS-uifRNAi* (F) embryo stained with antibodies against Uif. *btl* driven *uifRNAi* strongly and specifically reduces Uif expression in the tracheal system (arrows), without affecting its expression elsewhere (e.g. hindgut, arrowhead). In all cases anterior is to the left. (Scale bars = 50μm in A; 10μm in B-D.)

Supplemental Movie 3.1
Brightfield time-lapse movie of live *uif*^{2B7} mutant embryos during late embryogenesis showing defective tracheal inflation.
Eight mid stage 17 *uif*^{2B7} mutant embryos were imaged by brightfield microscopy every minute for 230 minutes. Note that partial tracheal inflation occurs in the embryos on the top left and the second from the bottom right. During this time series a completely uninflated larva (at bottom left) and a partial inflated larva (at top left) hatch and crawl away. All embryos were deemed to be alive during the time course, as muscular contractions continued through the end of the sequence for all of the embryos. Selected images of the embryo at the top left were compiled into Figure 3.5.

Supplemental Table 3.1
PCR primers for sequencing *uif* genomic region

Name	Sequence
5.1	TCT GAT TGC AGA TTG GCA AGA
3.1	GCA CAC CCA ATA GAC AGA CTA AC
5.2	ACC TTG TCT AAT ATG CCA ACT CCT
3.2	GAA CAA GTT GGC GAC TTC CT
5.3	AGC CAT ACT GAA TCG GTC ATA TCC T
3.3	ATT GTG CAG TGC ATC CGA GGT
5.4	ACA ATG TCC AGG TGT TCG ATG G
3.4	TCA GAT CGT TGG TGT ACT GC
5.5	AAC TGG ATA CTC ATC GAC CTG AAG G
3.5	AGA TCC ACG CTC ACA TAG GTG
5.6	AGC CAG AGT GCA AGG TCA TCA AG
3.6	ATC TTG ACC ACA TTC TCC TCC AGC A
5.7	ACT CAA CCA GTT GCT CTC GCA
3.7	AAC AGG CAG GGA TTC TCC GAA C
5.8	GAT CAG TGC GAC GTG ACC AT
3.8	CGT CGT TGA CGG AAG TGT ACT
5.9	AGT TTG CCC AGA AGG ACG ATC
3.9	ATT GTT CTG CGT ACC TCG GTA GTG G
5.10	AGA AGG TGA CCA ACT CGG TTA ATG GC
3.10	ATA GCT CAC AGC TAA AGG AAC CCT
5.11	GAT TGC TGG AAG ACC AGG AGT
3.11	GTT CTG ACA GTG AGT TAG CTG CTG
5.NdeI*	GGCCGGC<u>CATATG</u>GACTTCTGTCCAGCGTTGGC
3.BamHI*	GCTA<u>GGATCC</u>TTAAGTCACTCCTGGTCTTCCAGC

* Primers used to clone extracellular region of Uif protein for antibody generation. Restriction enzyme sites are underlined.

Chapter 4

Conclusion and future directions

In this dissertation, I have presented my research contributed to better understanding of tissue morphogenesis in the model organism *Drosophila melanogaster*. I have studied the expression pattern of the phosphorylated forms of myosin regulatory light chain (MRLC, Sqh in *Drosophila*) during imaginal disc development and embryogenesis. I have cloned and characterized a novel gene named *uninflatable* (*uif*), which is essential for embryonic tracheal air filling and larval tracheal growth. In the appendix, I have included my efforts in characterizing two *enhancer of broad* mutations that may play important roles during embryogenesis and imaginal disc morphogenesis.

In Chapter 2, I presented my work on studying the expression pattern of the phosphorylated forms of Sqh (nonmuscle myosin regulator light chain in *Drosophila*) using two phosphorylation site-specific antibodies, anti-Sqh1P and anti-Sqh2P. First, I demonstrated the specificity of the antibodies on immunoblots and immunostaining. Then I examined the expression pattern of Sqh1P and Sqh2P in imaginal discs and embryos. Interestingly, I observed that Sqh1P and Sqh2P have distinct subcellular localizations in imaginal discs. Sqh1P mainly localizes to the adherens junction, whereas Sqh2P mainly localizes to the

apical domain of the cell. In the embryos, Sqh1P and Sqh2P are differently expressed. Sqh1P is expressed fairly ubiquitous while Sqh2P concentrates in places undergoing extensive cell shape change or cell movement. During dorsal closure, Sqh1P is localized in a "dotted-line" pattern at the leading edge, whereas Sqh2P is enriched in the dynamic filopodial protrusions. These antibodies are useful tools to monitor myosin activation and can be used to identify upstream factors and signaling pathways that affect myosin activity during development. We have generated *Rho kinase* homozygous mutant clones and observed that the level and distribution of Sqh1P and Sqh2P are not affected in the mutant cells in late 3rd instar and white prepupal imaginal discs, indicating Rho kinase may not be the only relevant kinase capable of phosphorylating Sqh in the larval wing discs. Currently, we are examining the expression pattern of Sqh1P and Sqh2P in Rho mutant background (*Rho$^{E(br)246}$*, *en>RhoRNAi*, and *en>RhoV14*).

In chapter 3, I have included my work on *uif* gene. Loss of *uif* function results in tracheal air filling defects in embryos. Severity of the defects ranges from no inflation at all to almost complete inflation. Expression of *uifRNAi* ubiquitous or only in the tracheal system produces the same defects, indicating that *uif* is responsible for this phenotype. We have determined that the tracheal inflation defects in *uif* mutant animals result from a failure to establish an inflated tracheal system in late embryos rather than the ability to maintain fully inflated tracheae in early larval life. We have also determined that the inflation

defects are not due to improper tracheal maturation or disrupted paracellular barrier junction. However, we did observe that the tracheal tubes seemed crushed in *uif* mutant late embryos or early 1st instar larvae. We speculate that *uif* may play a structural role in the embryonic tracheae. The tracheal inflation defects in *uif* mutant embryos might result from violent muscular contractions that compromise tracheal tubes and generate cracks or obstructions in the cuticular lining that prevent complete air inflation. To test our hypothesis, we will perform transmission electron microscopy (TEM) to examine the ultra structure of the tracheal trunks in *uif* mutant animals. We will also use muscimol (a GABA agonist) to inhibit muscular contraction during embryogenesis and see if the tracheal tubes in *uif* embryos will remain intact and can be fully inflated.

Loss of *uif* also gives rise to tracheal growth defects in larvae. Previous study indicated that the larval tracheal length increases in a continuous fashion [1]. The ratio of tracheal length to overall body length does not change during larval stages. However, tracheae in *uif* 3rd instar are out of proportion to the body length of the animal. The control mechanisms of tracheal growth remain largely unknown. To date, the only two genes known to affect tracheal growth in *Drosophila* larvae are *uif* and *Mmp1* that encodes a Matrix Metalloproteinase [2]. Second-site noncomplementation test suggested that *uif* does not interact with *Mmp1* genetically. Interestingly, knockdown of *uif* in imaginal discs attenuates Notch activation and results in *Notch*-like growth defects that produce *Notch*

loss-of-function phenotypes in adults. This observation raised the suspicion that *uif* may also work through the Notch signaling pathway to regulate growth in larval tracheal. Larval tracheal tissue becomes polyploidy by exiting mitotic cell cycle and entering an endoreplication cycle, a process that is thought to be important in its rapid growth. Previous studies indicated that the mitotic-to-endocycle switch was controlled by Notch signaling in follicle cells during *Drosophila* oogenesis [3-5]. Based on these facts, we hypothesize that Notch signaling may also regulate endoreplication cycle during *Drosophila* larval tracheal development. To test the hypothesis, we will first knockdown the expression of Notch in the larval tracheal system and examine the effect on tracheal growth. If Notch signaling is required for tracheal growth, we will next test whether activation of Notch signaling is regulated by *uif* in the tracheal system.

Uif protein remains high conservation in insect species after 350 million years of evolution. The extracellular domain of Uif contains various functional domains including carbohydrate binding domains and signaling domains. It is possible that Uif plays different roles in various tissues during different stages of development. For example, Uif may play a structural role and provide mechanic support to the embryonic tracheal system, whereas may be a signaling molecular and co-activator of Notch during imaginal disc development. We will perform structure/function analysis to identify regions of the Uif protein required for embryonic tracheal inflation, larval tracheal growth, and imaginal disc cell

specification and growth. Full length and various deletion *uif* constructs will be generated and introduced in the *Drosophila* genome by recombineering [6, 7]. We expect the full-length *uif* construct will fully rescue embryonic and larval defects in *uif* mutant animals. The different deletion constructs will help us to further understand the functions of each domain of Uif. The cytoplasmic domain of Uif protein maintains over 80% protein sequence conservation in insect species after ~350 million years of evolution. This suggests that the cytoplasmic domain contains important functional domains. However, this domain also does not contain any known conserved protein binding or signal transduction motifs. One way to uncover the potential function of the domain is to identify the proteins with which it binds to. To accomplish this, we will perform yeast two-hybrid and tandem affinity purification-mass spectroscopic screening to identify proteins that physically interact with the cytoplasmic domain of Uif.

In the appendix, I have included my work on two *E(br)* (*enhancer of broad*) mutant lines, *E(br)155* and *E(br)65* [8]. *E(br)155* shows strong genetic interaction with *broad* and *Rho1*. Homozygous *E(br)155* mutant embryos have multiple defects resembling those in septate junction mutant embryos. Furthermore, septate junction markers, including Cor, Fas3 and DLG, are mislocalized in *E(br)155* mutant embryos. We have determined that there are at least 3 lethal mutations on the left arm of the second chromosome in *E(br)155*, which are in *little imaginal discs* (*lid*), *uninflatable* (*uif*), and *Macroglobulin*

complement-related (*Mcr*) gene. *Mcr* is likely the enhancer of *broad* mutation and is responsible for septate junction integrity. We have generated new alleles of *Mcr* by imprecise excision of a P-element insertion in *Mcr* genomic region. The new alleles display septate junction defects and embryonic cuticular defects similar to those in the original *E(br)155* line. To further prove that the defects are caused by a mutation in *Mcr*, we will attempt to rescue the mutant phenotypes by introducing transgenic construct of *Mcr* in the *E(br)155* mutant background. We will generate antibody against Mcr and study the expression pattern and subcellular localization of the protein. More experiments will be done to further understand the molecular function of *Mcr* and the role of *Mcr* during development.

E*(br)65* also shows strong genetic interaction with *borad* and components of *Rho* signaling pathway. Homozygous *E(br)65* mutant animals are mainly early larval lethal. Interestingly, dead *E(br)65* embryos display a low penetrant cuticular defect of missing certain abdominal dentical belts. Heterozygous *E(br)65* larvae and adults are bigger than wild type animals at the same stage, indicating *E(br)65* may have a dominant effect on growth. We have attempted to generate new alleles of *E(br)65* by EMS mutagenesis and screened through 2800 lines without isolating a new allele. Fine scale P element mapping indicated that the mutation locates in cytological region 26D-F. We have sequenced 7 candidate genes in the region without finding a specific mutation. Furthermore, *E(br)65* complements all the deficiencies (available before May,

2005) uncovering this region. Now, there are more molecularly defined deficiencies available. We should continue doing more complementation tests with the new deficiency stocks. If none of the new deficiencies fail to complement *E(br)65* and the region 26D-F is completely covered by the deficiencies, it is most likely that *E(br)65* is a dominant or gain-of-function mutation. Before continuing studying *E(br)65*, we may revert the mutation to a loss-of-function one through X-ray mutagenesis and then recover new alleles through a traditional F2 screen using chemical mutagenesis.

References

1. Beitel, G.J., and Krasnow, M.A. (2000). Genetic control of epithelial tube size in the Drosophila tracheal system. Development *127*, 3271-3282.
2. Page-McCaw, A., Serano, J., Sante, J.M., and Rubin, G.M. (2003). Drosophila matrix metalloproteinases are required for tissue remodeling, but not embryonic development. Dev. Cell *4*, 95-106.
3. Deng, W.M., Althauser, C., and Ruohola-Baker, H. (2001). Notch-Delta signaling induces a transition from mitotic cell cycle to endocycle in Drosophila follicle cells. Development (Cambridge, England) *128*, 4737-4746.
4. Shcherbata, H.R., Althauser, C., Findley, S.D., and Ruohola-Baker, H. (2004). The mitotic-to-endocycle switch in Drosophila follicle cells is executed by Notch-dependent regulation of G1/S, G2/M and M/G1 cell-cycle transitions. Development (Cambridge, England) *131*, 3169-3181.
5. Schaeffer, V., Althauser, C., Shcherbata, H.R., Deng, W.M., and Ruohola-Baker, H. (2004). Notch-dependent Fizzy-related/Hec1/Cdh1 expression is required for the mitotic-to-endocycle transition in Drosophila follicle cells. Curr Biol *14*, 630-636.
6. Venken, K.J., He, Y., Hoskins, R.A., and Bellen, H.J. (2006). P[acman]: a BAC transgenic platform for targeted insertion of large DNA fragments in D. melanogaster. Science (New York, N.Y *314*, 1747-1751.
7. Venken, K.J., Carlson, J.W., Schulze, K.L., Pan, H., He, Y., Spokony, R., Wan, K.H., Koriabine, M., de Jong, P.J., White, K.P., et al. (2009). Versatile P[acman] BAC libraries for transgenesis studies in Drosophila melanogaster. Nature methods.
8. Ward, R.E., Evans, J., and Thummel, C.S. (2003). Genetic modifier screens in Drosophila demonstrate a role for Rho1 signaling in ecdysone-triggered imaginal disc morphogenesis. Genetics *165*, 1397-1415.

Appendix Chapter

Cloning and characterization of two dominant modifiers of *broad*

broad (*br*) is a primary response early gene in the ecdysone signaling cascade and plays an important role during leg imaginal disc elongation and eversion [1]. In a screen for dominant modifiers of the malformed leg phenotype associated with a hypomorphic *br* allele (br^1), we identified mutations in at least 15 different genes (referred to as *enhancer of broad* or *E(br)* mutations) [2]. I studied 2 of these mutant lines, *E(br)155* and *E(br)65*. Both mutations show strong genetic interaction with *br* and components of *Rho* signaling pathway. Both mutations have interesting embryonic cuticular defects. We have determined that *E(br)155* is likely allelic to *Macroglobulin complement-related* (*Mcr*) gene. *E(br)65* is likely a dominant mutation and needs to be reverted to a loss-of-function one.

I. Cloning and characterization of *E(br)155*

E(br)155 shows strong genetic interaction with br^1 and *Rho1*. *E(br)155* shows complete embryonic lethality when homozygous, with poorly differentiated dentical belts (100%, n=235) and obvious defects in mid-embryonic morphogenesis. Specifically, 50% (n=235) of the dead embryos have

defects in dorsal closure, whereas 10% (n=235) show defects in head involution (Appendix Figure 1 B and data not shown). *E(br)155* also has embryonic tracheal length defects. Dorsal trunks in *E(br)155* mutant embryos are longer and appear tortuous comparing to those in wild type embryos (Appendix Figure 1 C, D). Taken together, all the embryonic defects in *E(br)155* reminisce those in septate junction (SJ) mutant embryos, indicating *E(br)155* may be a regulator of SJ. Consistently, SJ markers including Cor, Dlg and Fas3 are mislocalized in *E(br)155* mutant embryos (Appendix Figure 1 F and data not shown). Furthermore, dye permeability experiment [4] demonstrates that the paracellular barrier function of the SJ is disrupted in these mutant embryos (Appendix Figure 1 H).

Through meiotic mapping and complementation tests, we have determined that there are at least 3 lethal mutations on the left arm of the second chromosome in *E(br)155* (Appendix Figure 2). Meiotic mapping with recessive markers indicated that the *enhancer of broad* mutation is located in cytological region 28E. Consistently, *E(br)155* failed to complement a molecularly defined deficiency line *Df(2L)Exel7034* (cytology 28E1; 28F1). Furthermore, *E(br)155* failed to complement a P element line, *P{EPgy2}Mcr*^{EY07421}(cytology 28E3), which has a P insertion in the first non-coding exon of *Macroglobulin complement-related* (*Mcr*) gene. Sequence analysis of genomic DNA isolated from *E(br)155* mutant embryos revealed a Serine to Leucine missense mutation in the α2 macroglobulin domain. This serine is conserved in all insect species. We have recombined *Mcr*$^{E(br)155}$ apart from the

other second-site mutations. Without other background mutations that may had made the animals sicker, homozygous ($Mcr^{E(br)155}/Mcr^{E(br)155}$), hemizygous ($Mcr^{E(br)155}/Df(2L)Exel7034$), and trans-heterozygous ($Mcr^{E(br)155}/Mcr^{EY07421}$) mutant embryos display milder cuticular phenotypes than *E(br)155* as well as some novel defects including excessive luminal chitinous material in the salivary glands and the tracheal system. The dorsal closure defect in these embryos is much less penetrant. Septate junction defects and tracheal length defects were still present. We have generated more alleles of *Mcr* by imprecise excision of the P element allele. The new alleles display septate junction defects and embryonic cuticular defects similar to those in $Mcr^{E(br)155}$ mutant embryos. Taken together, *E(br)155* may result from the mutation in *Mcr* gene, which may be a novel regulator of SJ integrity. Current, we are trying to rescue the mutant phenotypes in *E(br)155* by introducing a full length *Mcr* cDNA construction into the mutant background. We will generate antibody against Mcr and study the expression pattern and subcellular localization of the protein.

The two second-site mutations in *E(br)155* are in the gene *uninflatable* (described in detail in chapter 2 of this dissertation and the published manuscript [2]) and the gene *little imaginal discs* (*lid*), which functions as a histone H3K4 demethylase and homologous to vertebrate Retinoblastoma binding protein 2 (RBP2) [3, 4]. This *lid* allele (refer to as lid^1) results from a nonsense mutation (19 base pair deletion at nucleotide 158410-158428 of GenBank sequence **AC092216** generating an immediate stop codon after R^{1383},

Appendix Figure 3) and fails to complement two P element *lid* alleles, *P{PZ}lid*^{10424} and *P{lacW}lid*^{k06801}. PCR primers for sequencing genomic DNA were listed in Appendix table 1.

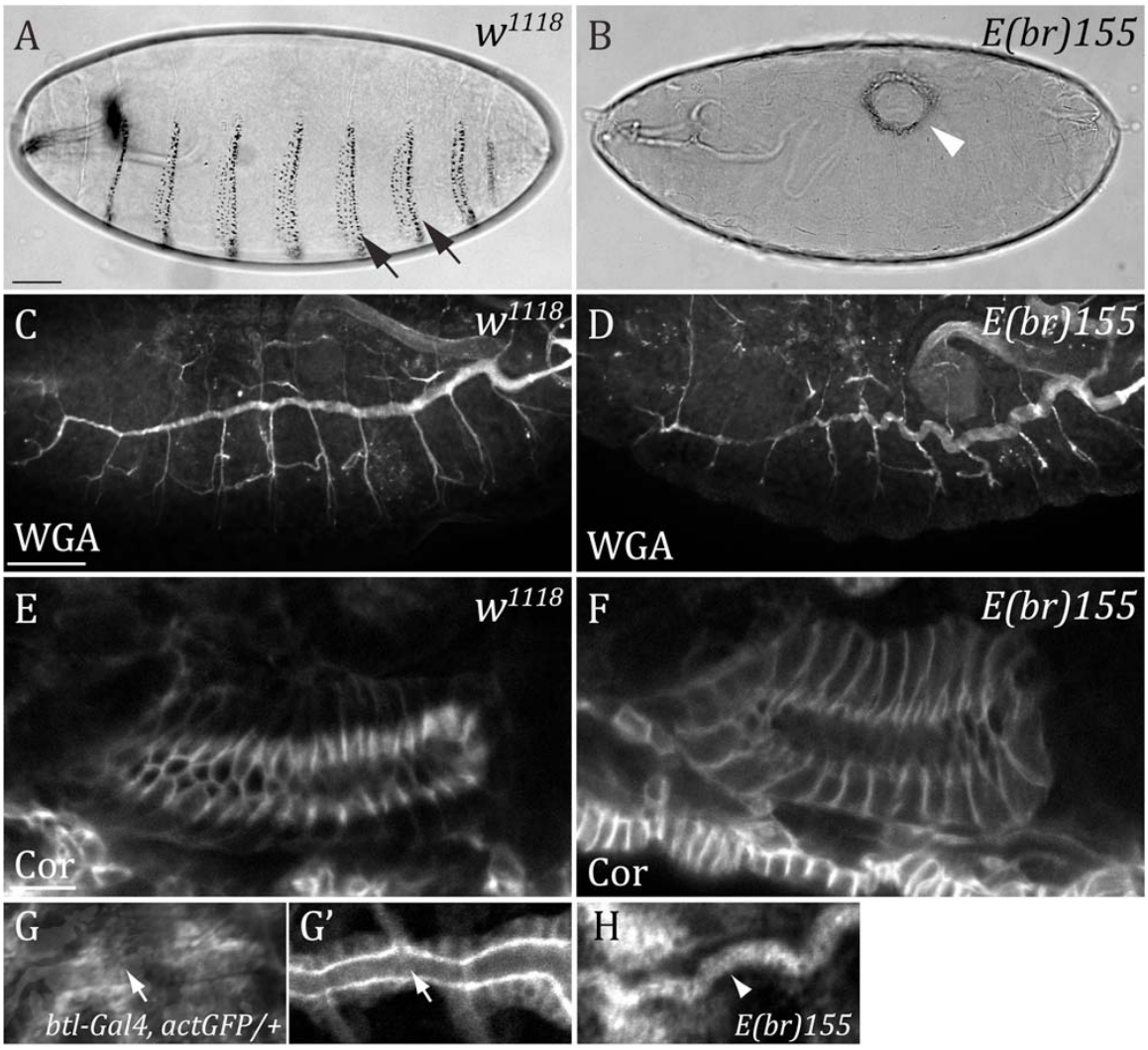
A
w1118
B
E(br)155
C
w1118
WGA
D
E(br)155
WGA
E
w1118
Cor
F
E(br)155
Cor
G
btl-Gal4, actGFP/+
G'
H
E(br)155

Appendix Figure 1
***E(br)155* mutant embryos have septate junction related defects**
(A, B) Brightfield micrographs of cuticle preparations of wild type (A) and *E(br)155* (B) embryos. Note the *E(br)155* mutant embryo lack dentical belts (arrows in A) and contains a dorsal hole (arrowhead).
(C, D) WGA staining shows the tracheal length is longer in a stage 16 *E(br)155* mutant embryo (D) than in a wild type embryo at the same stage (C).
(E, F) Confocal images of salivary glands in wild type (E) and *E(br)155* embryo (F) stained with an antibody against the septate junction protein Coracle (Cor). Note the broader distribution of Cor on the lateral membrane of the epithelial cellsw in *E(br)155* salivary gland (F).
(G-H) The paracellular barrier function of SJ is disrupted in *E(br)155* embryos. Rhodamine-dextran was injected into hemocoel of stage 17 embryos. In control embryos (G), the dye could not cross the tracheal epithelium (arrow points to tracheal lumen). The position of the tracheal trunk is visualized by GFP expressed in the tracheal cells (G'). In *E(br)155* embryos (H), the dye crossed the epithelium and filled the lumen of the tracheal trunk (arrow).

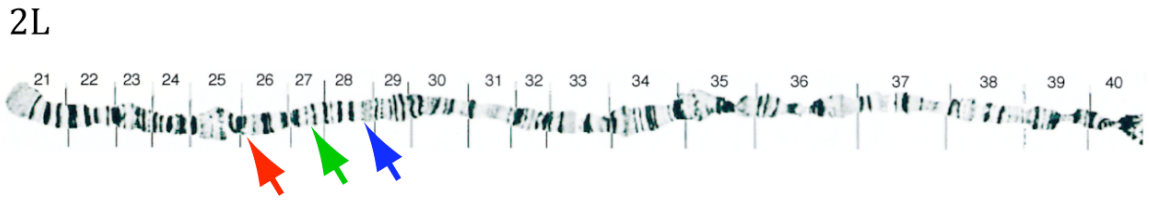

Appendix Figure 2
Three closely linked mutations on chromosome 2L in *E(br)155* mutant line
The mutation in 28E (blue arrow) is the real enhancer of *broad* mutation. The two second-site mutations include *uif* in 27D (green arrow) and *lid* in 26B (red arrow).

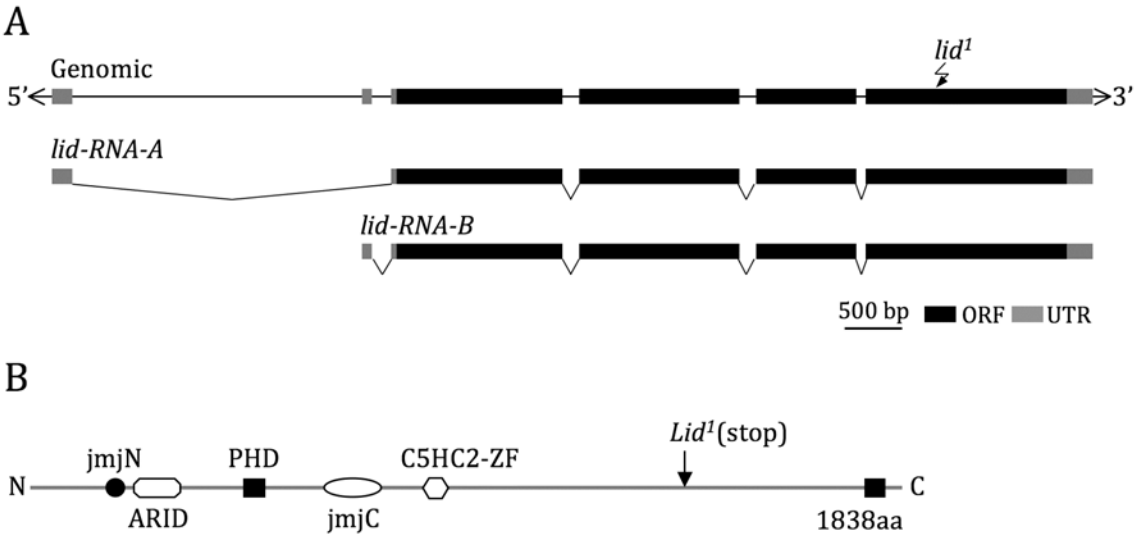

Appendix Figure 3
Genomic organization of *lid*
(A) Structure of the *lid* genomic locus predicted by flybase [5].
(B) Predicted domain organization of Lid protein (adapted from [3]).
The position of *lid*^{1} mutation is shown in both A and B.

Appendix Table 1
PCR primers for sequencing *lid* genomic region

Name	Sequence
5.1	ACC AAG TTG TGA ACT CAT CCG T
3.1	ATG TCG ATG TAG CAG GCA GT
5.2	ACC TGC CGA TTG GCT GAA
3.2	GAT CCT GCC AGT TCA TCG CA
5.3	AGA TTG TGG CCA GCT TCA
3.3	CGT TGT TAA TGC GTA AAT ATA GCG A

II. Characterization of *E(br)65*

45% of *br1; E(br)65/+* flies and 17% *E(br)65/+* flies show malformed legs, indicating *E(br)65* may have a dominant effect on leg morphogenesis. *E(br)65* shows second site non-complementation with mutations in the small GTPase *Rho1*, the guanine nucleotide exchange factor *RhoGEF2*, non-muscle myosin heavy chain *zipper*. It also interacts strongly with a phosphomimetic form of the myosin regulatory light chain *sqhE20E21*. Homozygous *E(br)65* mutant animals mostly die as early first instar larvae without obvious defects. Dead mutant embryos display a low penetrant defect in their denticle belts (Appendix Figure 4 B). Heterozygous mutant animals have larger body size and larger imaginal discs than wild type ones, indicating *E(br)65* may have a dominant effect on growth (data not shown and Appendix Figure 4 C, D).

To map the mutation, we have performed fine scale meiotic mapping with three individual pairs of P element lines and got consistent results between these 3 parallel experiments. Based on calculation with recombination ratios and the position of the P insertions, we predict that the lethal mutation may localize to sequence region 6,500,000 – 6,650,000 (Cytology 26D-26E) (Appendix Table 2). However, *E(br)65* complemented all the available deficiencies in that region (Appendix Table 3). In Appendix Figure 5 A, I drew out the combined results of P element mapping and complementation tests. We isolated genomic DNA from *E(br)65* animals and sequenced eight candidate genes in the interval (*CG31638*,

CG31637, *eya*, *osm-6*, *Ent2*, *CG9596*, *CG13766*, and *CG34345*, see Appendix Figure 5 B). No nonsense or missense mutations were identified. An F_2 EMS screen was performed to isolate new alleles of *E(br)65*. We screened 2800 individual mutations without isolating a single new allele. Now, there are more molecularly defined deficiencies available. We should continue doing more complementation tests with the new deficiency stocks.

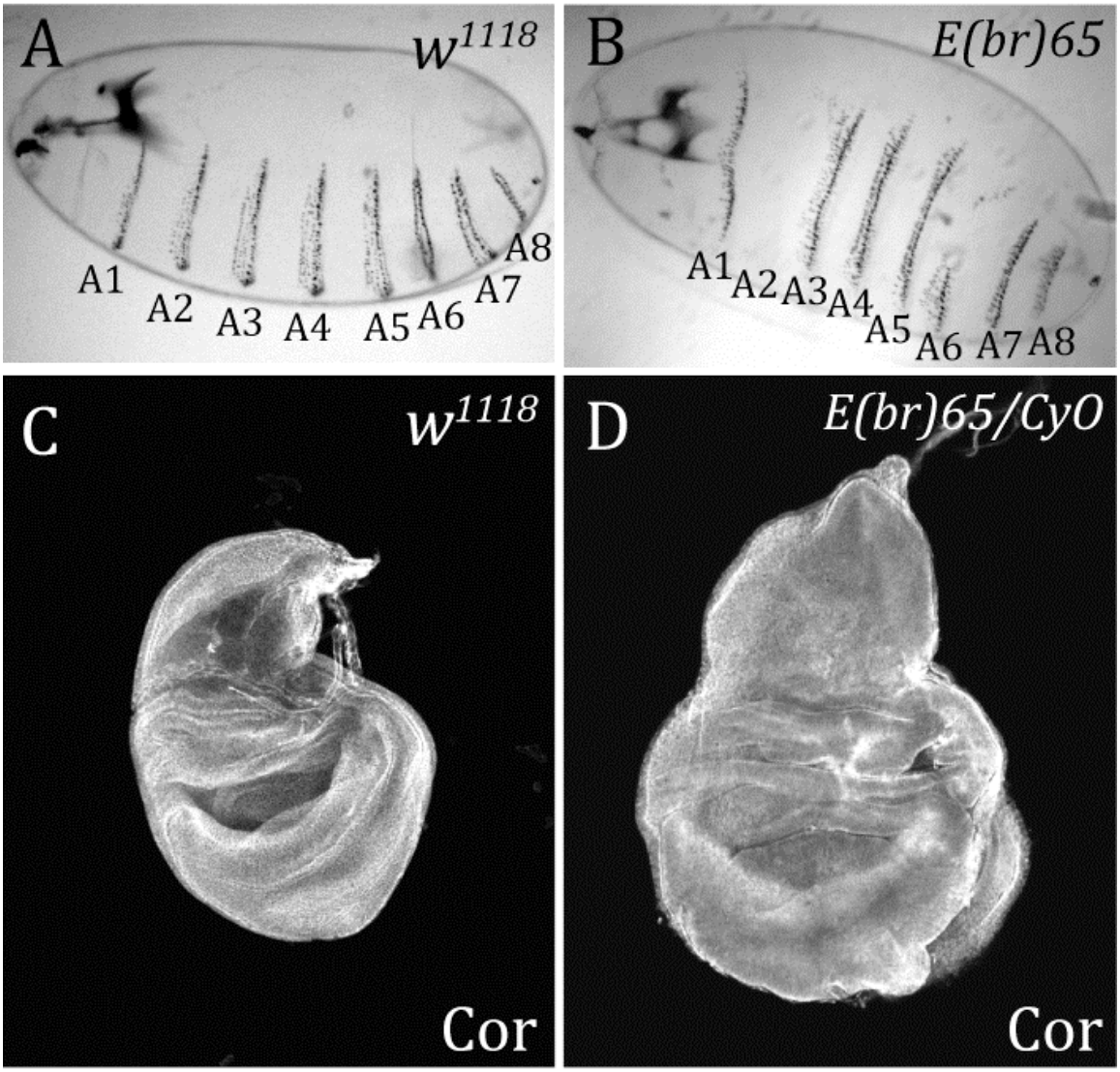

Appendix Figure 4
Defects in *E(br)65* homozygous mutant animals
(A, B) Brightfield micrographs of cuticle preparations of wild type (A) and *E(br)65* (B) embryos. The whole denticle belt in segment A2 and half of the denticle belt in A6 are missing in this mutant embryo.
(C, D) Confocal images of wing imaginal discs from w^{1118} (C) or *E(br)65/CyO* (D) wandering 3rd instar larvae stained with an antibody against Cor. Note the *E(br)65/CyO* disc is much bigger than the wild type one.

Appendix Table 2
P element mapping of *E(br)65*

P element insertions	Sequence location	Cytological location	Recombination ratio (n)
P{w[+mC]=lacW}Gef26[k13720]	6,323,822	26C3	1.8% (10788)
P{w[+mC]=lacW}nrv2[k13315]	6,792,138	27B1	2.3% (8714)
P{w[+mC]=lacW}l(2)k09923[k09923]	6,411,355	26D1	1.8% (16459)
P{w[+mC]=lacW}xl6[k00230]	6,919,363	27C4	2.9% (13234)
P{lacW}CG9523[k07502b]	6,424,371	26D1	2.0% (6961)
PBac{w[+mC]=RB}CG11188[e03057]	6,718,183	27A1	2.7% (7220)

Appendix Table 3
Complementation tests between *E(br)65* and deficiencies

Stock number	Deficiencies	Sequence location	Cytological location	Result
7801	Df(2L)Exel7027	6,664,818–6,786,906	26F6–27B1	Complement
7802	Df(2L)Exel7029	6,922,143–7,022,707	27C4–27D4	Complement
7803	Df(2L)Exel8019	7,140,502–7,202,317	27E2–27E4	Complement
7503	Df(2L)Exel6017	7,202,317–7,418,128	27E4–27F3	Complement
7501	Df(2L)Exel6015	6,088,361–6,262,082	26B9–26C1	Complement
7502	Df(2L)Exel6016	6,253,101–6,411,492	26C1–26D1	Complement
7800	Df(2L)Exel9038	6,292,859–6,338,855	26C2–26C3	Complement
6338	Df(2L)BSC6	NA	26D3–26F7	Complement
6454	Df(2L)BSC9	NA	26F5–27B2	Complement
6374	Df(2L)BSC7	NA	26D10–27C1	Complement

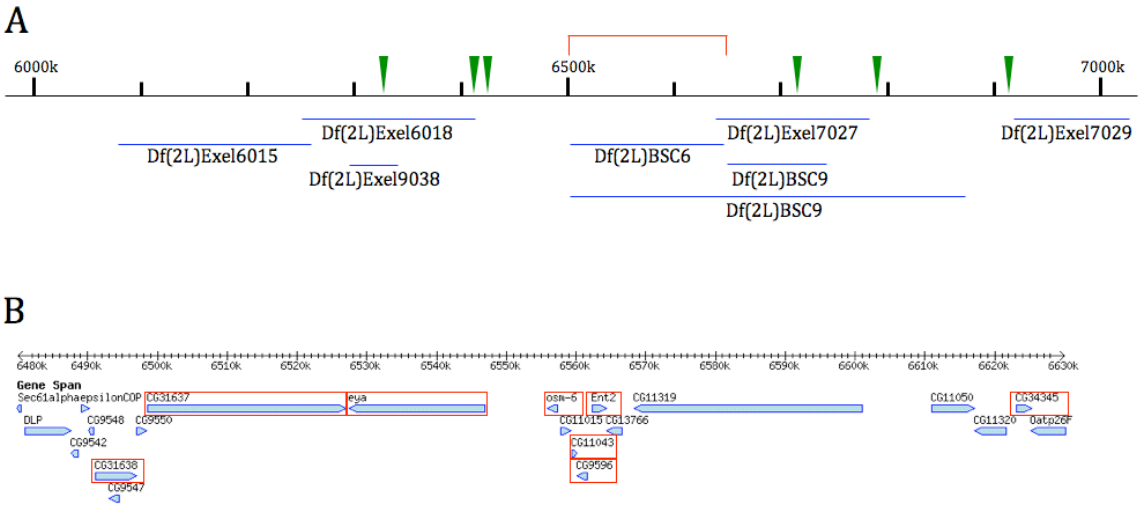

Appendix Figure 5
P element mapping, complementation tests, and genomic DNA sequencing results of *E(br)65*
(A) Green arrowheads point to the locations of the P element stocks used for mapping. Red bracket indicates the sequence location of the lethal mutation based on P element mapping (2L: 6500000- 6650000). Blue lines indicate the regions covered by the deficiencies.
(B) Overview of the genes in sequence region 6,480,000 – 6,630,000.The genes that have been sequenced include: *CG31638*, *CG31637*, *eya*, *osm-6*, *Ent2*, *CG9596*, *CG13766*, and *CG34345*. (The picture is adapted from flybase [5]).

References

1. Kiss, I., Beaton, A.H., Tardiff, J., Fristrom, D., and Fristrom, J.W. (1988). Interactions and developmental effects of mutations in the Broad-Complex of Drosophila melanogaster. Genetics *118*, 247-259.
2. Zhang, L., and Ward, R.E. (2009). uninflatable encodes a novel ectodermal apical surface protein required for tracheal inflation in Drosophila. Developmental biology *336*, 201-212.
3. Lloret-Llinares, M., Carre, C., Vaquero, A., de Olano, N., and Azorin, F. (2008). Characterization of Drosophila melanogaster JmjC+N histone demethylases. Nucleic acids research *36*, 2852-2863.
4. Gildea, J.J., Lopez, R., and Shearn, A. (2000). A screen for new trithorax group genes identified little imaginal discs, the Drosophila melanogaster homologue of human retinoblastoma binding protein 2. Genetics *156*, 645-663.
5. Tweedie, S., Ashburner, M., Falls, K., Leyland, P., McQuilton, P., Marygold, S., Millburn, G., Osumi-Sutherland, D., Schroeder, A., Seal, R., et al. (2009). FlyBase: enhancing Drosophila Gene Ontology annotations. Nucleic acids research *37*, D555-559.